VHE Gamma-Ray Sources at the Resolution Limit of H.E.S.S.

Dissertation

zur Erlangung des akademischen Grades
doctor rerum naturalium
(Dr. rer. nat.)
im Fach Physik
eingereicht an der Mathematisch-Naturwissenschaftlichen Fakultät
der Humboldt-Universität zu Berlin
von

Kornelia Stycz

Präsident der Humboldt-Universität zu Berlin
Prof. Dr. Jan-Hendrik Olbertz
Dekan der Mathematisch-Naturwissenschaftlichen Fakultät
Prof. Dr. Elmar Kulke

Gutachter/innen:
1. Prof. Dr. Thomas Lohse
2. Prof. Dr. Marek Kowalski
3. Prof. Dr. Mathieu de Naurois

Tag der mündlichen Prüfung: 19.06.2015

Kurzfassung

Die bodengebundene Gammaastronomie beschäftigt sich mit der Detektion von Photonen mit Energien von einigen zehn GeV bis zu etwa 100 TeV mittels der abbildenden atmosphärischen Cherenkov-Technik. In dem Verfahren wird die Atmosphäre als Detektor für hoch-energetische Gammastrahlung verwendet, da Photonen in diesem Energiebereich mit den Atomen und Molekülen der Atmosphäre wechselwirken und Teilchenschauer produzieren, die Cherenkov-Strahlung aussenden. Das Cherenkov-Licht wird von Teleskopen mit großen Spiegelflächen gesammelt um Abbildungen der Teilchenschauer zu erhalten, aus denen die Eigenschaften des verursachenden Gammaquants abgeleitet werden können. Bei den atmosphärischen Wechselwirkungen handelt es sich um statistische Prozesse, daher fluktuieren die Abbildungen der Schauer. Die Rekonstruktion der Richtung des ursprünglichen Teilchens ist durch die Fluktuationen fundamental begrenzt. Zudem hängt die Qualität der Rekonstruktion von der Energie des eintreffenden Photons, den Beobachtungsbedingungen, den Eigenschaften des Teleskops und dem Rekonstruktions-Algorithmus ab. Die Präzision der Richtungsrekonstruktion einzelner Gammaquanten wird als Winkelauflösung bezeichnet.

Diese Arbeit beschäftigt sich mit der Winkelauflösung von H.E.S.S. , einem Experiment der bodengebundenen Gammaastronomie. H.E.S.S. ist ein System aus fünf Teleskopen, von denen vier für den Energiebereich oberhalb einiger hundert GeV konizipiert sind. Für dieses Vier-Teleskop-System werden die systematischen Fehler der Winkelauflösungsfunktion und ihre Abhängigkeiten von Beobachtungsparametern an Hand von Beobachtungsdaten und Monte-Carlo-Simulationen abgeschätzt. Die aus Monte-Carlo-Simulationen gewonnene Auflösungsfunktion wird zur Vermessung von Quell-Morphologien verwendet. Abweichungen der simulierten Auflösungsfunktion von der mit H.E.S.S. an Hand von Punktquellen gemessenen werden im Rahmen dieser Arbeit identifiziert und quantifiziert. Damit kann die simulierte Auflösung der Realität angepasst werden. Mit der korrigierten Funktion werden zwei Phänomene studiert, die ein genaues Verständnis der Auflösung erfordern:

Zum einen wird die Ausdehnung der Emission des Krebsnebels im Energiebereich oberhalb von 500 GeV untersucht. Der Krebsnebel ist eines der am meisten erforschten astronomischen Objekte außerhalb unseres Sonnensystems und wurde als erste Quelle der hochenergetischen Gammastrahlung entdeckt. Verschiedene Modelle sagen im von H.E.S.S. gemessenen Energiebereich Ausdehnungen von 0.009° bis ca. 0.03° vorraus, bisher wurden experimentell allerdings nur Obergrenzen für die Größe angegeben. In dieser Arbeit werden die H.E.S.S. -Beobachtungen des Krebsnebels selektiert, die eine gute Auflösung mit geringen systematischen Fehlern erwarten lassen. Da die gemessene Ausdehnung mit einem Wert von $(0.01 \pm 0.002_{(stat)} \pm 0.015_{(syst)})$ Grad trotzdem nicht signifikant von Null verschieden ist, wird hier ebenfalls eine Obergrenze angegeben. Der systematische Fehler wird unter Berücksichtigung aller Unsicherheiten der Auflösungsfunktion des gewählten Datensatzes berechnet. Auf einem Konfidenzniveau von 95% wird die Obergrenze der Ausdehnung damit zu 0.034° bestimmt.

Zum anderen wird nach ausgedehnter Emission um Aktive Galaxienkerne gesucht. Aktive Galaxienkerne sind weit entfernte Objekte, die ihre Energie aus supermassiven Schwarzen Löchern im Zentrum von Galaxien beziehen. Die von ihnen emittierte Gammastrahlung wechselwirkt mit der extragalaktischen Hintergrundstrahlung und es entstehen Paare von Elektronen und Positronen. Diese können wiederum in Wechselwirkungen mit dem kosmischen Mikrowellen-Untergrund Gammastrahlung produzieren, sodass sich Kaskaden bilden. In Abhängigkeit von der Stärke des extragalaktischen Magnetfeldes können die Kaskaden die Form eines sphärischen Halos oder eines geweiteten Strahlungskegels an-

nehmen. In dieser Arbeit werden Modell-Vorhersagen für beide Ausprägungen mit den H.E.S.S. -Beobachtungsdaten dreier Aktiver Galaxienkerne verglichen um Obergrenzen für den gemessenen Fluss einer augedehnten Komponente zu berechnen. Die so erzielten Einschränkungen auf den Fluss sind die niedrigsten bisher veröffentlichten im TeV-Bereich. Unter der Annahme einer geweiteten Kaskade werden außerdem Stärken des extragalaktischen Magnetfeldes von $(0.1 - 10) \cdot 10^{-15}\,\mathrm{G}$ auf einem Konfidenzniveau von 99% ausgeschlossen. Die Untersuchungen werden analog zur Veröffentlichung H.E.S.S. Collaboration et al. (2014b), die im Rahmen dieser Arbeit entstanden ist, für zwei verschiedene Modelle der extragalaktischen Hintergrundstrahlung durchgeführt.
Abschließend wird ein Ausblick auf das geplante Gammastrahlen-Teleskop CTA gegeben und die experimentellen Möglichkeiten der beabsichtigten Winkelauflösung werden, insbesondere im Hinblick auf die hier studierten Phänomene, diskutiert.

Abstract

Very-high-energy (VHE) γ-ray astronomy deals with the ground-based detection of photons with energies of a few tens of GeV to $\sim$ 100 TeV by employing the Imaging Air Cherenkov Technique (IACT). This method uses the atmosphere as a detector for VHE γ-rays, exploiting that photons in that energy range produce particle showers by interacting with atmospheric particles. The particle showers, in turn, emit Cherenkov light, which is collected by telescopes with large mirror areas to image the particle shower. The properties of the γ-rays, specifically their energy and direction, can be deduced from the shower images. However, the interactions in the atmosphere are statistical processes, imposing a natural limit on the direction reconstruction with IACT experiments. In addition, the direction reconstruction is limited by the detection efficiency of Cherenkov photons of the telescope. The quality of the direction reconstruction depends on the energy of the primary particle, the telescope properties, observational conditions and reconstruction algorithm. The precision of the direction reconstruction of single photons is characterized as the angular resolution. In this work, the angular resolution of H.E.S.S. , an IACT experiment located in Namibia, is studied in detail. H.E.S.S. consists of five telescopes, four of which were built for the energy range above a few hundreds of GeV and started operating in 2004. For this sub-array, the systematic errors on the angular resolution and their dependence on observation parameters are estimated from known point sources in H.E.S.S. data and from Monte-Carlo simulations. A mismatch between H.E.S.S. data and Monte-Carlo simulations is quantified and the simulated angular resolution is corrected for it. With the correction, two phenomena that require a profound knowledge of the angular resolution are assessed.

First, the size of the the Crab Nebula at VHE is investigated. The Crab Nebula is one of the best-studied objects beyond our solar system and was the first source detected in VHE γ-rays. Models predict a size of the emission region of 0.009° to $\sim 0.03^\circ$ in the energy range observed with H.E.S.S. In this work, a size of $(0.01 \pm 0.002_{(stat)} \pm 0.015_{(syst)})$ deg is found, i.e. the source is not significantly extended. Including a detailed accounting of the systematic errors, a conservative upper limit on the size of the VHE γ-ray emission region of the Crab is given by 0.034° at a 95% confidence level.

Second, extended emission around Active Galactiv Nuclei(AGN) is searched for. AGN are distant objects with a supermassive black hole as their central engine. Due to interactions with the cosmic microwave background and the extragalactic background light, the particles emitted by AGN are expected to form cascades. The effect of the cascades on the observable size of the VHE emission region of AGN depends on the magnetic field. Two scenarios for different magnetic field strengths are probed with H.E.S.S. data, pair halo emission and beam-broadened cascade emission. The most constraining upper limits on the pair halo scenario are found, compared to published figures. Employing the beam-broadened cascade scenario, extra-galactic magnetic field strengths in the range of $(0.1-10)\cdot 10^{-15}$ G are excluded at a 99% confidence level. All of the studies are conducted for two models of the extragalactic background light, in analogy to H.E.S.S. Collaboration et al. (2014b) which was published in the scope of this thesis.

Finally, an outlook on the angular resolution of the future IACT experiment CTA and its ability to measure the phenomena mentioned here is given.

Contents

Der Zauber steckt immer im Detail.
Theodor Fontane

1. Introduction

Throughout the history of astronomy, each step of enhancement of the angular resolution took humanity's knowledge of the universe to a new level. Adding detail to observations probed existing scientific paradigms, and humanity's view of the whole world was shaken several times. When the first telescopes were introduced at the beginning of the 17th century, their gain of angular resolution compared to observations with the naked eye was about a factor of three. Galileo Galilei enhanced the technique to a factor of ∼20 and was able to detect the four moons of Jupiter, that are named after him nowadays. Besides, he realized that the Milky Way was composed of single stars, but his most momentous finding was the full set of phases of the Venus, see Fig. 1.1(a). The changing shape of the luminous Venus could only be explained by its rotation around the Sun, proving the Copernican heliocentric model. Heliocentricity was not only denied by the Church, but also by most astronomers and philosophers, who followed Aristotelean cosmology at that time. The struggle between the geocentric and the heliocentric view of the world is a story often told. Mankind lost its place in the centre of creation, but it gained the foundations of scientific progress as we know it today.

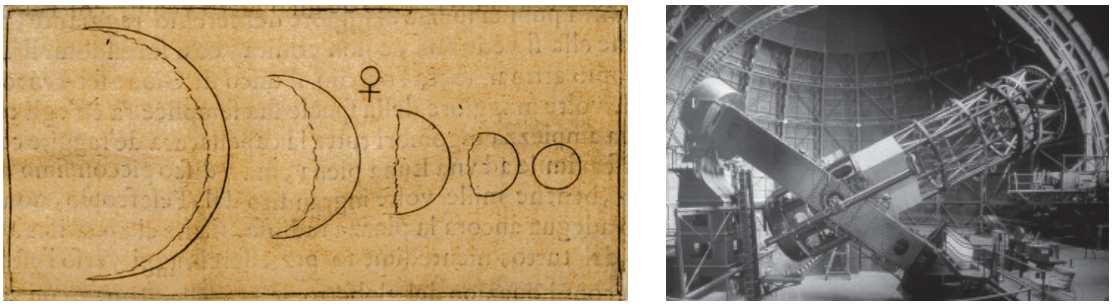

(a) (b)

Fig. 1.1.: (a) Drawing of the different phases of the Venus by Galileo Galilei. (b) Hookes 100-inch optical telescope of the Mount Wilson Observatory. Image credit: Huntington Library via mtwilson.edu.

Since then, the race for higher angular resolutions has never ceased. Already in 1655, the Dutch astronomer Huygens was able to resolve what he thought was one ring of Saturn, and in 1659 he succeeded in subdividing the Orion Nebula into different stars, which suggested that also other nebulae were in fact consisting of stars. Soon after, Newton built the first functioning reflecting telescope, and with the advances of parabolic mirror production throughout the 18th and 19th centuries telescopes grew larger and could therefore resolve smaller angular distances.
In the 1920s, mankind was once again struggling to find its place in the cosmic order. In the "Gread Debate" between the American astronomers Harlow Shapley of Mount Wilson Observatory and Heber D. Curtis of Lick Observatory, nothing less than the size of the whole universe was discussed. While Curtis believed that the "spiral nebulae", as spiral galaxies were called at that time, were outside our Galaxy, Shapley was convinced that they

were part of our Galaxy, and that our Galaxy made up all of the universe. The angular resolution of the Lick Observatory already allowed Curtis to detect the jet of Messier 87, an object now well-known to be a distant active galaxy. Also the relation between luminosity and frequency of Cepheids, a class of pulsating stars, was known (although not fully correct) and they were used as standard candles for distance measurements as early as 1912 — by Shapley, by the way. However, it needed the resolving power of the Hookes 100-inch telescope (see Fig. 1.1(b)) at the Mount Wilson Observatory to let Edwin Hubble detect a Cepheid in the Andromeda Nebula. Although Hubble's estimation of the distance to the Andromeda Galaxy was less than half of the distance known today (2.5 million light years), it went beyond the scope of what even Curtis imagined. The realm of humanity was but a tiny spot in a vast cosmos.
To make matters worse, Hubble found that the universe was expanding followed right after. Today, the *Hubble Space Telescope (HST)*, which is named after him, resolves galaxies that are 13 billion light years away, i.e. that existed only 500 million years after the Big Bang.
Enhancing the resolution power of the Hookes telescope by optical interferometry, Michelson and Pease were able to measure the diameter of a star for the first time in 1920. It was Betelgeuse, a red supergiant star, which is ∼1000 times larger than the sun. The most powerful optical telescope in terms of its limiting resolution today is CHARA, a long-baseline optical interferometer also located on Mount Wilson. With its data, the first images ever obtained of the surface of another star the size of the sun (Altair) were published (Monnier et al. 2007), and optical astronomy is pushing toward even better resolution with extremely large telescopes and adaptive optics.

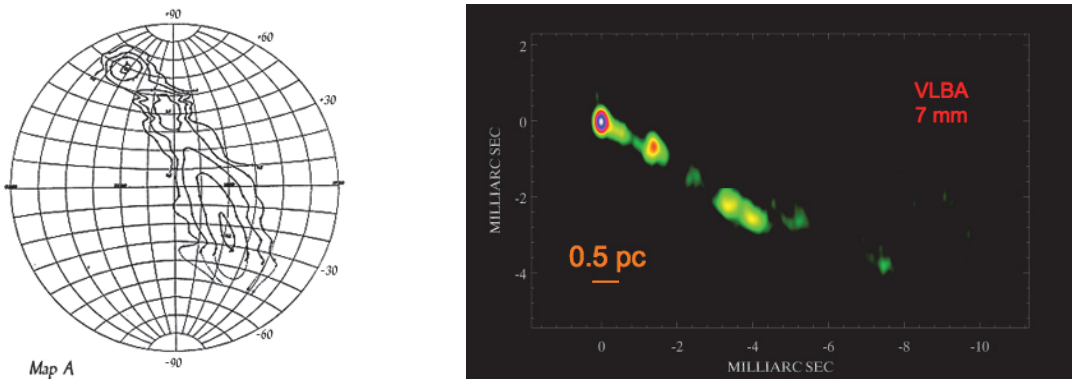

(a) (b)

Fig. 1.2.: (a) A part of the first radio map of our Galaxy, produced by G.Reber in 1939. The coordinates are right ascension (RA) and declination (Dec). (b) Radio observations of the jet of the AGN 3C120 with VLBI. Images by R. C. Walker (NRAO).

Meanwhile, astronomers are using other wavelengths of electromagnetic radiation to literally see the universe in a different light. Starting with infrared (IR) astronomy at the end of the nineteenth century, radio astronomy developed since the 1930s, and ultra-violet (UV) and radio observations followed in the 1940s. A new generation of instruments in each of these fields always also meant progress in resolving power, since understanding the observed astrophysical phenomena required measurements at smaller and smaller scales. A particularly good example of how improvements in angular resolution in such fields pushed scientific progress are the developments in the radio energy band. After radio emission from the Galactic centre was detected by Jansky in 1931, the first radio map was drawn by Grote Reber in 1939 (see Fig. 1.2(a)). It displays the galactic plane with

the galactic centre at -29° declination, and, at roughly +40° declination, the active galaxy Cygnus A. The detection of that object already hinted at one of the main benefits of radio observations: The science of Active Galactic Nuclei (AGN) or quasi-stellar radio sources, a.k.a. quasars, as they were called upon their discovery in 1963. Soon, the necessity of a higher angular resolution was recognized and met with the introduction of Very-Long Baseline Interferometry (VLBI). The establishment of this new technique, which allowed for the resolution of objects on a scale of milli-arcseconds, was almost immediately rewarded by the discovery of superluminal motion in 1969 (Gubbay et al. 1969), i.e. the apparent movement of AGN jets faster than the speed of light. Today, the VLBI technique enables astronomers to watch the development of jets on sub-parsec scales, see Fig. 1.2(b), and thereby gain insights into the acceleration mechanisms of these amazing objects. Current efforts in high-resolution radio astronomy go as far as testing general relativity in the strong gravity regime at the event horizon of the supermassive black hole in the Galactic Centre.

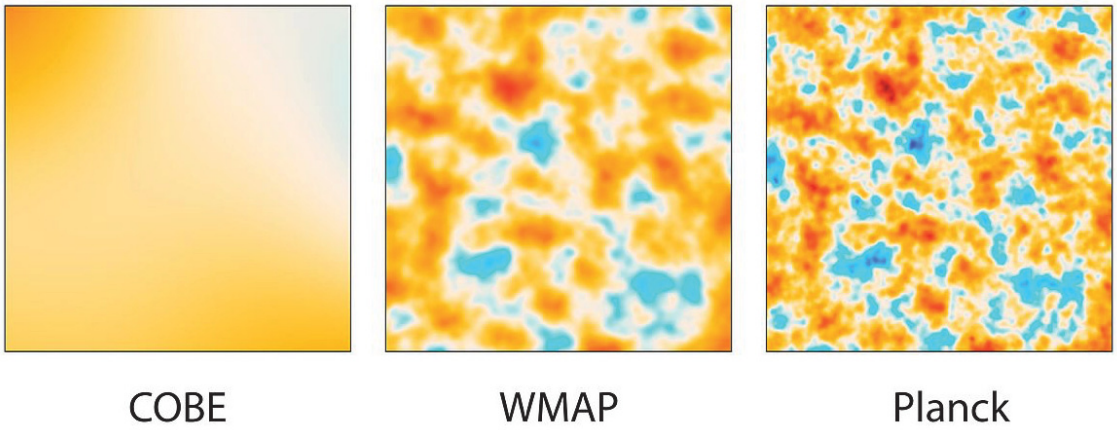

Fig. 1.3.: Comparison of angular scales of the CMB resolved by the COBE, WMAP and Planck satellites (from left to right). The images present 10-square-degree patches. Image Credit:NASA/JPL-Caltech/ESA.

Another field that progressed through gain in angular resolution are measurements of the Cosmic Microwave Background (CMB). The CMB is often called "the echo of the Big Bang" since it consists of the photons produced in the recombination phase of the universe, when space became transparent to visible light for the first time. This makes it our prime source of information on the evolution of the universe in the first 380 000 years of its existence. First detected as a uniform background by Arno Penzias and Robert Wilson in 1964, large-scale anisotropies were found in observations with the COBE satellite in 1992. These observations were matching the predictions of Rashid Sunyaev's theory of the Big Bang, which also predicted anisotropies on smaller scales due to baryo-acoustic oscillations in the primordial matter before recombination. With that knowledge and the data of balloon experiments with a better angular resolution, like BOOMERanG, TOCO and MAXIMA at the end of the 1990s, the distance to the last scattering surface before recombination was measured, and a flat geometry of the universe was determined. Observations with the WMAP satellite, which could resolve even smaller structures, confirmed an accelerated expansion of the universe in the ΛCDM model, the simplest big bang cosmological model that includes dark energy (associated to the cosmological constant Λ) and cold dark matter (CDM). From smaller angular scales of the anisotropies, the baryon density and the dark matter density could be determined. Today, owing to data taken

with the PLANCK satellite, parameters of the ΛCDM model and derived values like the Hubble constant are known to an unprecedented level of precision. The evolution of the angular resolution of the satellites measuring the CMB is depicted in Fig. 1.3.
With $\sim 0.1^\circ$, the angular resolution in ground-based γ-ray astronomy is comparatively low. This field of astronomy deals with the detection of photons in the very-high-energy (VHE) range, i.e. at energies of tens of GeV to $\sim$100 TeV. The view on the Galactic plane in TeV γ-rays, overlaid on an optical image, visualizes the difference in resolvable scales in these energy bands, see Fig. 1.4. The low angular resolution is partly caused by the indirect detection method, which is employing the atmosphere as a detector and is subject to statistical fluctuations. More than that, however, the fundamental resolution limits are far from being reached since γ-ray astronomy is a relatively young field of research. The first VHE γ-ray source was discovered only in 1989 with the Whipple Telescope (Weekes et al. 1989), which had an angular resolution of $\sim 2^\circ$. The instruments existing nowadays are the third generation of VHE γ-ray telescopes. The initial focus of these instruments was the detection of objects in this entirely new energy band. Therefore, the main goal of the analyses was maximising the significance of a detection. With an increasing number and variety of sources, the need for more detailed knowledge arose, specifically spectral and morphological information. The introduction of stereoscopy, advanced detection and analysis techniques lead to an improvement in angular resolution by a factor of $\sim$20. With the current angular resolution, the shells of some supernova remnants can be morphologically resolved, for example. An even better resolution in this "new window to the universe" will certainly result in more groundbreaking discoveries.

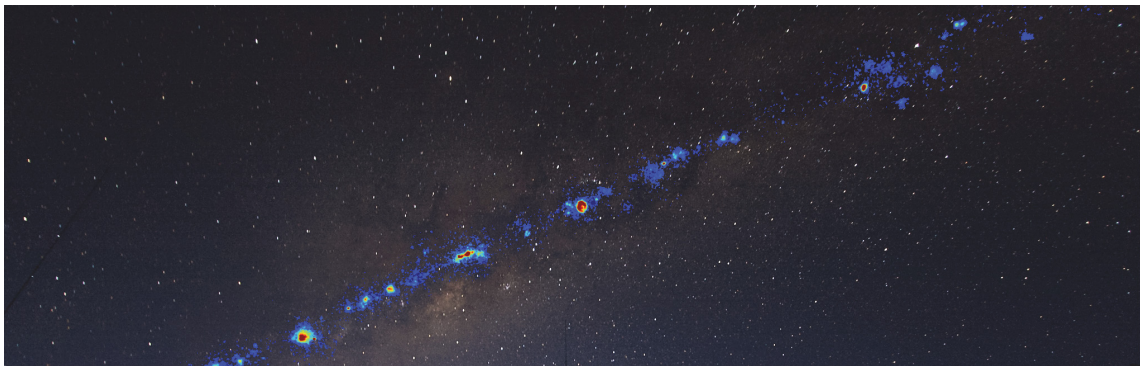

Fig. 1.4.: Overlaid images of the galactic plane in optical light and in VHE γ-rays. The telescope in the foreground is part of H.E.S.S., a ground-based γ-ray instrument. Photograph and montage by F. Acero.

In this work, the angular resolution of the H.E.S.S. experiment is studied in detail, with the aim to identify and quantify the systematic errors on it and to give meaningful constraints on two phenomena that require its profound understanding. In the first chapter, an overview of γ-ray emission mechanisms and of known sources of cosmic γ-rays is given, and the imaging air Cherenkov technique (IACT) of ground-based γ-ray detection is introduced. The IACT experiment H.E.S.S. is described in Chapter 3, with an emphasis on instrument and observation parameters that influence the angular resolution. Chapter 4 deals with the angular resolution of H.E.S.S., including detailed descriptions of how the expected angular resolution is calculated from Monte Carlo simulations and how source sizes are obtained with its help. By comparison with observational data, the systematic errors on source size measurements are estimated. The acquired insights are used in the following two chapters. In Chapter 5, an upper limit on the size of the TeV γ-ray emission

of the Crab Nebula is given and in Chapter 6, a search for extended emission phenomena around Active Galactic Nuclei is conducted. The results of both studies are summarized in Chapter 7 and an outlook on the potential of further improvements of the angular resolution of TeV γ-ray instruments is given.

2. Cosmic Gamma Rays

Cosmic VHE γ-rays are produced at the sites of the most energetic processes in the universe. The first section of this chapter gives an overview of such non-thermal processes and of the different classes of γ-ray sources detected so far. Subsequently, the interactions of γ-rays with the Earth's atmosphere are described. In particular, the formation of particle cascades and their emission of Cherenkov radiation in the atmosphere are discussed, since these processes are used for the ground-based detection of γ-rays. Finally, in Sec. 2.4, the imaging atmospheric Cherenkov technique and the challenges of detecting γ-ray sources with it are described.

2.1. Origin

VHE γ-rays are produced in interactions of accelerated charged particles with radiation fields and ambient matter. There are several mechanisms to convert the energy of these cosmic particles to γ-rays. Generally, it is differentiated whether γ-rays originate in *leptonic* or in *hadronic* processes in a source, i.e. whether the accelerated particles are electrons and positrons or nuclei. In the following, the most common γ-ray production scenarios are briefly discussed.
Hadronic interactions are of special interest because the cosmic-ray puzzle remains unsolved: Vast amounts of cosmic protons and nuclei with energies up to 10^{21} eV hit the earth, but it is unclear whether the known accelerators can explain all of the flux, and whether they contribute to the flux at the highest energies. Since very energetic hadrons can produce VHE γ-rays, photons with TeV energies can be tracers of cosmic-ray acceleration. The most common hadronic processes resulting in γ-rays are interactions that produce neutral pions (π^0), such as interactions between protons p,

$$p + p \rightarrow X + \pi^0 \tag{2.1}$$

and the photo-production of mesons (i.e. of the π^0) from nucleons N,

$$N + \gamma \rightarrow X + \pi^0. \tag{2.2}$$

With a probability of 98.8%, the π^0 decays into two photons, representing an efficient γ-ray source. In the GeV and TeV energy range, the γ-ray energy spectra resulting from hadronic interactions are almost identical to the parent proton spectrum. Assuming diffusive shock acceleration (also called first-order Fermi acceleration, since it was proposed by Fermi (1949)) as the proton acceleration mechanism, power-law spectra with an index of $\Gamma \approx$ -2 are expected. Since mechanisms of proton acceleration would also accelerate other charged particles, the VHE γ-ray emission from hadronic processes is accompanied by synchrotron emission of leptons at lower energies. Synchrotron radiation has a broad band spectrum, that typically peaks at X-ray energies for γ-ray emitting sources. In the spectral energy distributions of VHE γ-ray emitters, the two processes typically manifest themselves in two "humps".
However, VHE synchrotron radiation of leptons would require leptons with unrealistically high energies (since $E_{sync} \ll E_{lepton}$) and strong magnetic fields. Depending on the ambient

photon fields, inverse-compton (IC) scattering is a much more efficient process and is therefore considered as the primary source of γ-rays with energies above 1 TeV in leptonic scenarios. The target photons of IC scattering are the CMB, starlight, but also the photons created via synchrotron radiation - the process is then called synchrotron self-compton (SSC) and it is one of the most successful scenarios in modelling the emission spectra of AGN.
IC and synchrotron photons can trace the same electron population emitted by a source, therefore the double-humped energy spectra of VHE γ-ray sources can also be explained in leptonic scenarios: The peak at lower energies describes the synchrotron photon emission, the peak at higher energies results from IC radiation.
There is a broad variety of source types that emit γ-rays with TeV energies. In the following, the source classes detected at VHE and established models for the acceleration mechanisms taking place in them will be described.

Supernova Remnants (SNRs)

A supernova is either the collapse of a massive star at the end of its evolution or the thermonuclear explosion of a white dwarf, that accreted enough matter from a companion star to surpass the Chandrasekhar limit (Chandrasekhar 1931).
The explosion drives shock waves into the interstellar medium, which are the sites of particle acceleration for thousands of years. These shock fronts are detected as almost radially symmetric SNR "shells" at VHE and are among the most extended γ-ray emitters. For example, the SNR RXJ 1713.7−3946, shown in the left panel of Fig. 2.1, has a diameter of 0.8° . It was the first morphologically resolved TeV γ-ray source (Aharonian et al. 2004). The processes of γ-ray emission in SNRs are under debate: On the one hand, SNRs are the

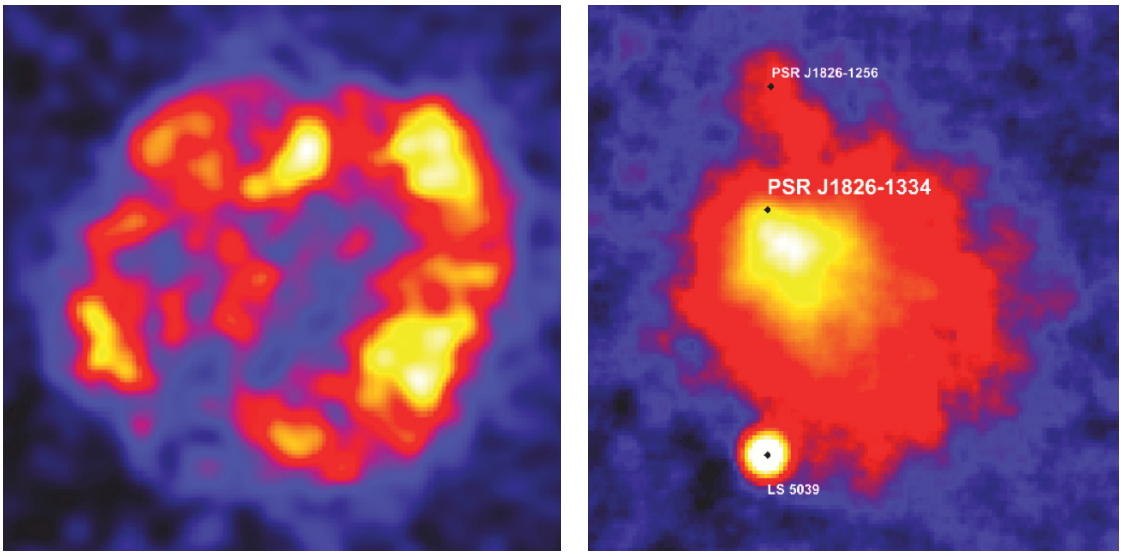

(a) (b)

Fig. 2.1.: (a) The shell-type SNR RXJ 1713.7−3946 as seen in VHE γ-rays with H.E.S.S. . Figure taken from Aharonian et al. (2007d). (b) Maps of the VHE emission of the extended PWNe HESS J1826−130 and HESS J1825-137, and the binary system LS 5039. PSR 1826−1256 and PSR 1826−1334 are the pulsars powering the two PWNe. Image courtesy of Brucker (2013).

prime candidates for cosmic-ray acceleration. In particular, a pion-decay signature feature was observed in the spectra of the two SNRs IC 443 and W44 (Ackermann et al. 2013b). On the other hand, the correlation between SNR morphologies at X-rays and at γ-rays points to a leptonic origin, and for some SNRs an IC scattering scenario is preferred to describe the high-energy spectral distribution (Aharonian et al. 2009). A better angular resolution of the measurements at VHE could probe the leptonic scenario by correlating the γ-ray emission to other wavelengths at smaller scales.

Pulsars and Pulsar Wind Nebulae (PWNe)

PWNe are the most abundant class of TeV γ-ray sources in the Galactic plane. They consist of a relativistic plasma of electrons and positrons that emit synchrotron and IC radiation. Their central engines are pulsars, fast-rotating neutron stars that are the remnants of supernova explosions and whose magnetic moments are not aligned with the rotational axis. While the exact processes and location of particle acceleration in the pulsar magnetosphere are under debate (see, e.g., Sturrock 1971; Cheng et al. 1976; Arons & Scharlemann 1979; Li et al. 2012), it is seen as a fact that the particles are closely bound to the magnetic field lines and emit co-rotating cones of light around both magnetic poles (Bühler & Blandford 2014). Whenever one of them crosses the line of sight of the observer, an electromagnetic pulse is registered. These pulsations are long known and were detected throughout the electromagnetic spectrum, but their existence at energies $\geq$25 GeV was unexpected and it was just recently discovered (The MAGIC Collaboration 2008). Directly after their acceleration, the particles flow freely along the magnetic field lines, the ultra-relativistic wind they compose is therefore "cold" (i.e. radiation-suppressed). The magnetic field lines, however, move because of the rotation of the pulsar and develop a toroidal pattern. The cold wind terminates when the ram pressure of the particle wind is balanced by the particle pressure of the surrounding nebula. The zone of equilibrium is the *termination shock*, where particles are re-accelerated and their momenta are isotropised. Accordingly, they are no longer aligned with the magnetic field and start to emit synchrotron radiation, hence the term "synchrotron nebula" is often used synonymously with PWN. The acceleration mechanism of particles in the termination shock is under discussion: Classical approaches of diffusive shock acceleration are unlikely since they do not work efficiently on relativistic particles (Sironi & Spitkovsky 2011). Instead, magnetic reconnection might lead to the non-thermal particle acceleration (Lyubarsky 2003).
Depending on their distance, energy output and age[1], the region of VHE IC emission of PWNe can be largely extended, see Fig. 2.1. The morphology can then be energy-dependent and different spectra may be measured in different regions, provided the angular resolution is good enough (Aharonian et al. 2006c). In young systems ($<$ 1000 years), the SNR ejecta confining the PWN expand freely, but in older systems the interaction of the ejecta and the interstellar medium (ISM) can result in SNR shell emission and a reverse shock of the compressed interstellar gas. This makes the differentiation between SNR and PWN emission difficult. A good angular resolution is necessary to study the two components separately.

Binary Systems

About 70% of the stars in our Galaxy live in binary or even more complex systems. Compact object binary systems, i.e. binaries containing a neutron star or a black hole, can emit VHE γ-rays. Particles are either accelerated in jets that form due to accretion

[1]For a review on the evolution of PWNe, the reader is referred to Gaensler & Slane (2006).

onto the compact object (microquasar scenario) or in the collision zone of stellar/pulsar winds (Aharonian et al. 2008). In any case, the physical environment in a close binary system is characterized by a very high radiation density and high magnetic fields (mG – G), rendering it radically different from the conditions inside PNWe and SNRs (Hinton & Hofmann 2009). In such an environment, relativistic electrons and positrons cool rapidly via synchrotron and IC processes. Hence, the VHE γ-ray emission can only originate directly at the very localized spot of lepton acceleration and is expected to appear point-like in VHE γ-rays. Also in hadronic scenarios the free escape of particles from the acceleration sites is improbable due to the strong radiation fields. The detection of extended VHE γ-ray emission from a binary system would be surprising.

Active Galactic Nuclei (AGN)

Of the identified TeV γ-ray sources, AGN are the most abundant class. They are distant galaxies with a super-massive black hole (i.e. $m_{BH} \geq 10^6 m_{\odot}$) in their centre that accretes surrounding matter and produces powerful jets. The jets can be of Mpc scale and emit radiation of all wavelengths from radio to X-rays. Furthermore, AGN display variability on different timescales in different energy bands. During flares at VHE, some AGN outshone all galactic sources despite their huge distances. The exact processes of jet creation and acceleration are still unknown, possibilities ranging from shock-wave acceleration in magneto-hydro-dynamic (MHD) turbulence to centrifugal powers have been suggested (for a review, see, e.g., Rieger 2011, and references therein). The VHE-photon emitting particles in the jets are highly relativistic, reaching Doppler factors of up to 100 (Aharonian et al. 2007b). Both hadronic and leptonic γ-ray production are possible in the models under discussion and fit the observational data equally well.

(a) (b)

Fig. 2.2.: (a) Composite image of the radio galaxy Centaurus A. Overlaid are radio, optical and x-ray images. Credits: X-ray - NASA, CXC, R. Kraft (CfA), et al.; Radio - NSF, VLA, M. Hardcastle (U Hertfordshire) et al.; Optical - ESO, M. Rejkuba (ESO-Garching) et al. (b) Near-infrared image of the globular cluster Terzan 5. Image courtesy of ESO/F. Ferraro.

Most probably, the γ-rays that are detected from the direction of AGN also have their origin in the jets. This hypothesis is supported by the fact that mostly the AGN whose jets are pointing in our direction, so-called BL Lacertae objects (BL Lac, or blazars) and flat spectrum radio quasars (FSRQ), are visible in TeV γ-rays. However, the detection of some nearby radio galaxies in γ-rays may hint at the existence of isotropic VHE emission from AGN. Due to their large distances, the γ-rays from AGN are subject to energy-dependent absorption by the extragalactic background light (EBL). The higher the energy of the VHE photon, the shorter its free path length before pair-production with an EBL photon occurs. Accordingly, the absorption leaves an imprint on the VHE spectra, which can be used to determine the EBL level (see, e.g., H.E.S.S. Collaboration et al. 2013). Although the primary emission of most AGN is expected to be not resolvable with current VHE γ-ray instruments, interactions with the EBL and with magnetic fields may lead to measurable extensions. With a well-understood angular resolution, such phenomena can be probed (see Chapter 6).

Other Sources

Only few specimen were detected so far of the other source classes of VHE γ-rays. One of them are **globular clusters** (H.E.S.S. Collaboration et al. 2011), which are regions of extremely high star densities. Their γ-ray emission probably stems from the colliding winds of the stars or of the milli-second pulsars inside them, but the existence of a dominant "classic" γ-ray-emitting object (i.e. a PWN or binary system) cannot be ruled out. Similarly, VHE emission from **starburst galaxies** is expected to be caused by the high star formation and supernova rates, or rather the corresponding enhanced density of interstellar gas (Acero et al. 2009). Starburst galaxies are viewed as good candidates for cosmic-ray acceleration. **Molecular clouds**, on the other hand, are most probably not the sites of acceleration but effective targets for relativistic particles from nearby accelerators like SNRs, that might not be visible in γ-rays themselves (Aharonian et al. 2008; H.E.S.S. Collaboration et al. 2014d, e.g.,)). Regions of dense interstellar gas, powered in the same way, and unresolved sources are expected to contribute to the **diffuse galactic emission** of γ-rays (H.E.S.S. Collaboration et al. 2014a).

2.2. Air showers

The brightest steady source of VHE γ-rays in the sky is the Crab Nebula. Above 1 TeV, it emits $2.3{\cdot}10^{-7}$ photons per second and square meter, in other words, it requires a detection area of $\sim 10^5$ m^2 to detect one photon per minute. This illustrates, that large collection areas are needed to study VHE γ-ray sources. Such are realised by making use of the atmosphere as a calorimeter in the imaging air Cherenkov technique. The deposition of γ-ray energy in the atmosphere is described in the following.

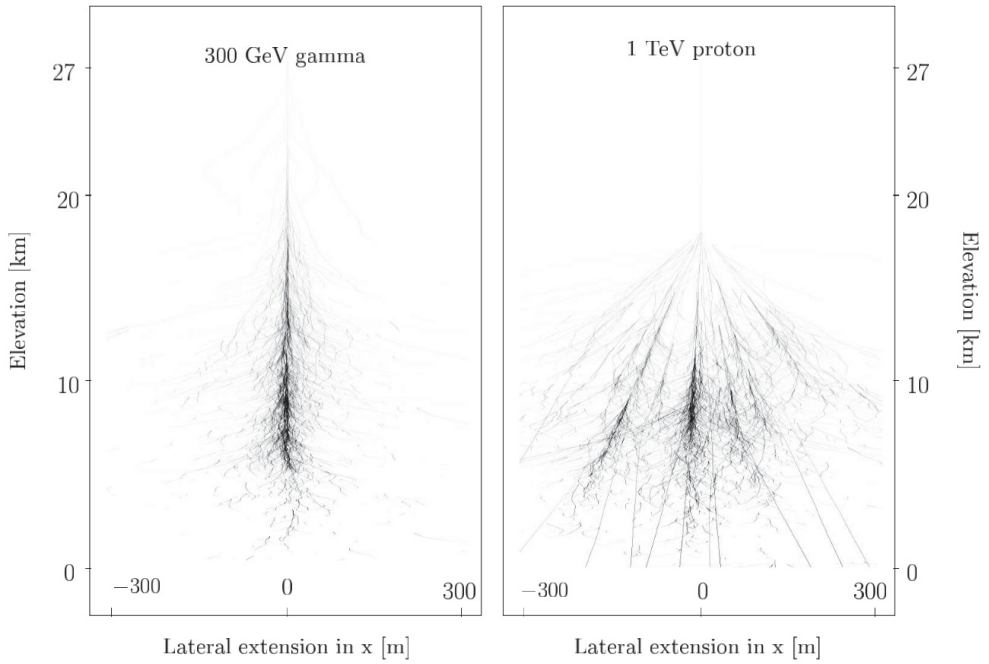

Fig. 2.3.: Simulated air showers induced by a photon with an energy of 300 GeV (left) and a proton with an energy of 1 TeV (right). All particles with energies above the threshold for Cherenkov photon production are shown. Figure taken from D. Berge (2006).

When a VHE γ-ray hits the atmosphere, it produces an electron-positron pair in the electromagnetic Coulomb field of an atmospheric nucleus. The electrons and positrons, in turn, emit high-energy bremsstrahlung photons (also in the Coulomb fields of nuclei) that again induce pair production. By multiple repetitions of this process, a cascade of secondary particles develops, a so-called *electromagnetic shower*. The mean free path lengths of electrons and positrons (which will be referred to as electrons from here on) and of photons in the atmosphere are of the same order of magnitude, hence they are often generalised as $X_0 \approx 40\,\mathrm{g\,cm^2}$. In fact, the radiation length of electrons in the atmosphere is $\sim 37\,\mathrm{g\,cm^2}$, given in units of area density, while the pair production length of photons is $\sim 47\,\mathrm{g\,cm^2}$.
The atmospheric depth of the first interaction is a crucial parameter for the development of the shower. This *primary interaction depth* is usually at about 15 – 20 km above sea level. Then the energy of the cascade is distributed on more and more particles, and the shower develops until the energy of the electrons and positrons drops below the *critical energy* E_c. Below that energy, which is 83 MeV in air, the electrons lose their energy rapidly via ionization and excitation of atmospheric particles, and the production of bremsstrahlung photons ceases. Assuming that the photons distribute their energy evenly on the electrons and positrons they produce, the maximum number of particles in a shower is proportional

to the energy of the primary particle and it is reached when the average energy of secondary particles is approximately E_c. Hence the height at which the maximum number of particles exists, the *shower maximum*, is lower if the primary particle energy is higher. Since the crucial quantity is the traversed atmospheric depth, the height of the shower maximum also depends on the inclination of the shower. Air showers with high inclinations, i.e. originating at high zenith angles, pass a longer way through the atmosphere until their shower maximum is reached. However, as for less inclined showers, their shower maximum forms at ∼10 km above sea level.
Except for a slight widening by multiple Coulomb scattering of electrons, electromagnetic showers develop along the direction of the primary particle and are of comparatively regular shape (see left panel of Fig. 2.3). Nevertheless, pair production, bremsstrahlung and Coulomb scattering as well as energy losses due to ionisation and excitation are statistical processes, hence the shower shape is not unambiguously attributable to a primary particle with certain properties.
Cosmic nuclei also induce showers when they hit the atmosphere. In contrast to electromagnetic showers, they are usually broader and can be very irregularly shaped (right panel of Fig. 2.3). This is caused by the variety of interactions that can take place in such *hadronic showers*: Inelastic scattering off atmospheric particles leads to the production of nuclei, mesons (kaons and pions), which form hadronic and electromagnetic sub-showers. The processes in hadronic showers are dominated by strong interactions, which can result in large transverse momenta and thereby a wide-spread distribution of shower particles. In hadronic processes, mostly via decay of charged pions and kaons, vast amounts of muons are produced. Many of them reach the ground before decaying, leading to a flux at sea level of about one muon per square centimeter per second.
In addition, electrons hit the atmosphere and also cause electromagnetic showers, which are difficult to discriminate from the ones initiated by γ-rays. On average, the showers initiated by electrons start earlier since the radiation length is shorter than the pair-production length.

2.3. Cherenkov radiation

Since the high-energy particles of an air shower move faster than the local phase velocity of light in air, the charged particles emit Cherenkov light. By this means, the cascades become luminous and thereby detectable. For a refractive index n, the Cherenkov light is emitted in a cone with an opening angle $2\theta_c$, with

$$\theta_c = \arccos \frac{c}{nv} \approx \arccos \frac{1}{n}. \tag{2.3}$$

The refractive index depends on the density of the medium, hence the opening angle of the Cherenkov light cone becomes wider the closer the cascade approaches the ground, where the pressure is higher. For electromagnetic showers, the superposition of light cones emitted at different heights results in an broad ring of Cherenkov light that has a radius of 80 – 150 m on the ground. Depending on the height of the shower maximum above ground, the ring appears rather like a filled circle, see left panel of Fig. 2.4. It is smeared out due to the multiple scattering of the shower electrons. The number of produced Cherenkov photons per emitted wavelength λ is proportional to $1/\lambda^2$. However, UV photons are fully absorbed by ozone (O_3) at wavelengths below ∼300 nm, therefore the light that reaches ground is mostly in the 300-500 nm band (Doering et al. 2001). Furthermore, the photons are subject to Mie and Rayleigh scattering, which diminish the number of photons on

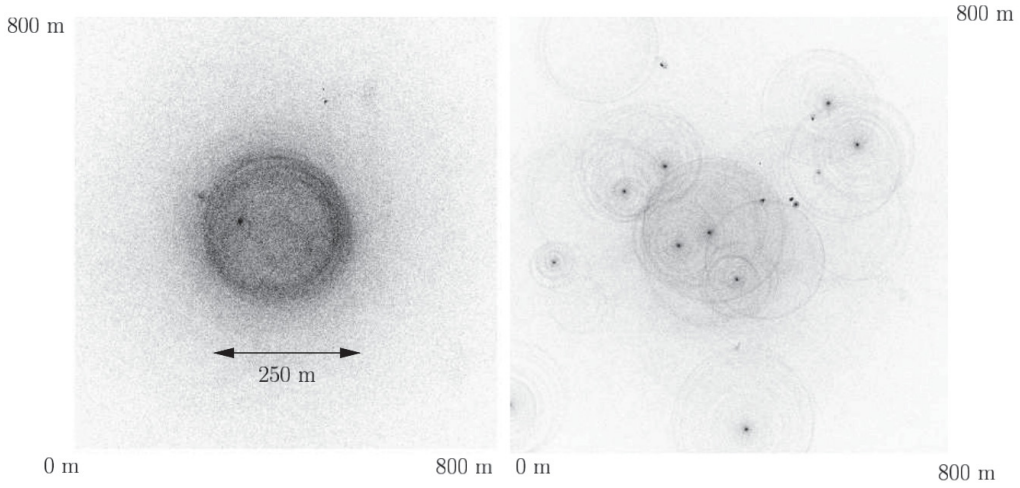

Fig. 2.4.: Cherenkov light distribution on ground of showers induced by photon with an energy of 300 GeV (left) and by a proton with an energy of 1 TeV (right). Figure courtesy of D. Berge (2006).

ground and are random processes that introduce ambiguity to observable shower shapes. For a primary γ-ray with an energy of 1 TeV, about 100 Cherenkov photons per square meter can be observed at a height of 2000 m above sea level. All of the Cherenkov light reaches the ground within a few nanoseconds.
Since most of the Cherenkov emission takes place at the shower maximum, its height determines how much light reaches the ground. This means that less Cherenkov photons reach the ground for showers induced by primaries with lower energies, even more so at large zenith angles. In addition, the radius of the Cherenkov ring on ground depends on the zenith angle of the shower: The height of the shower maximum stays approximately the same, therefore the Cherenkov photons traverse a larger distance before reaching ground if the shower is inclined. This purely geometrical effect leads to larger ring radii at high zenith angles, i.e. the Cherenkov photons are detectable at larger distances from the original shower axis.
Naturally, also the charged particles in hadronic air showers produce Cherenkov radiation that reflects the shower shape, see Fig. 2.4. Muons emit Cherenkov light even at ground level, where their energy is usually close to the Cherenkov light production threshold. In that case, the assumption of $v \approx c$ is not valid and their actual velocity determines the opening angle of the Cherenkov cone. Together with showers induced by electrons, hadronic showers and the Cherenkov light of muons are the main sources of background that need to be distinguished from showers produced by γ-rays. Since all of these background components originate in charged particles, that are deflected in cosmic magnetic fields, they arrive on Earth more or less isotropically distributed. γ-rays, on the other hand, point towards the direction of their source. This fact is used to estimate the level of background contamination of γ-ray observations.
Additionally, the *night sky background (NSB)*, which consists of starlight and light pollution from the ground, impedes the detection of Cherenkov photons.

2.4. Cherenkov telescopes

The detection of γ-rays with ground-based instruments is based on the detection of the Cherenkov light emission of their air showers, hence the method is called Imaging Air Cherenkov Technique (IACT). To collect as much light of the faint, short Cherenkov "flash" as possible, large mirror areas are used in the experiments, which focus the light into cameras that are sensitive to single photons and are read out with fast electronics. The camera images are isogonal reflections of the light emitted by the shower along its trajectory, which result in elliptical shapes of electromagnetic showers (see Fig. 2.5). The ellipse parameters reflect the basic properties of the shower and, thereby, the properties of the primary γ-ray. The size of the camera image, for example, is proportional to the energy of the original particle, and its axis connects the direction of origin of the particle with the point of intersection of the shower axis with the telescope plane. The distance to that intersection is called *impact distance*.

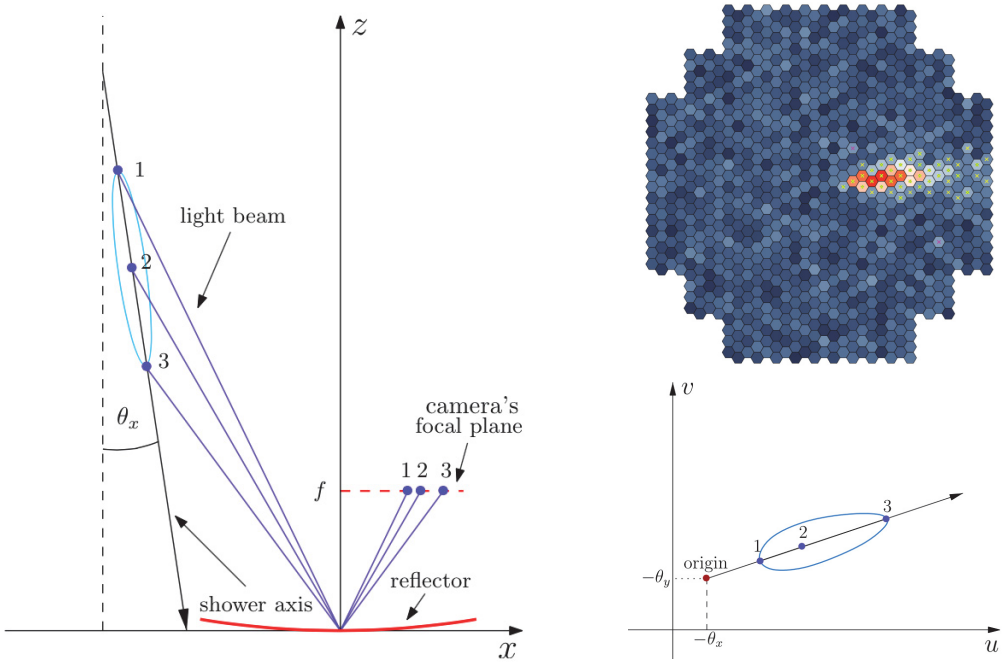

Fig. 2.5.: Imaging of an electromagnetic air shower with the air Cherenkov technique. On the left, a schematic of the isogonal reflection of different points of the shower into the focal plane of a camera is depicted. The resulting image of the shower in the camera plane, perpendicular to the z-axis in the picture on the left, is shown on the bottom right. In the upper right panel, a simulated shower image in one of the H.E.S.S. cameras is shown. Images courtesy of T. Nowak and K. Bernlöhr.

The quality of the reconstruction can be significantly improved by employing stereoscopic observations. Generally speaking, more of the information carried by the Cherenkov light of a shower can be collected with multiple telescopes. Most importantly, the direction reconstruction becomes much more precise because the shower is seen under different angles. In the simplified picture of elliptical shower images (Hillas ellipses), the intersection of the axes of showers imaged by different telescopes is a good estimate for the source direction. Furthermore, since the quality of the angular resolution is also limited by the fact that only a fraction of the Cherenkov light hits the telescopes, larger collection areas are advantegeous.

With cleverly spaced telescopes, the sensitivity of the instrument increases: The larger the area of a telescope array, the larger the volume of the atmosphere that can be observed, hence the event statistics are increased. In addition, a stereoscopic system facilitates the suppression of muonic background. By requiring coincident events in two telescopes, local fluctuations of photons are filtered out. If the telescope spacing is large enough, muons are not seen stereoscopically since they develop their Cherenkov cones close to the ground. The implementation of these concepts will be presented in detail in the next section using the example of H.E.S.S. , the most successful current-generation IACT.

3. H.E.S.S.

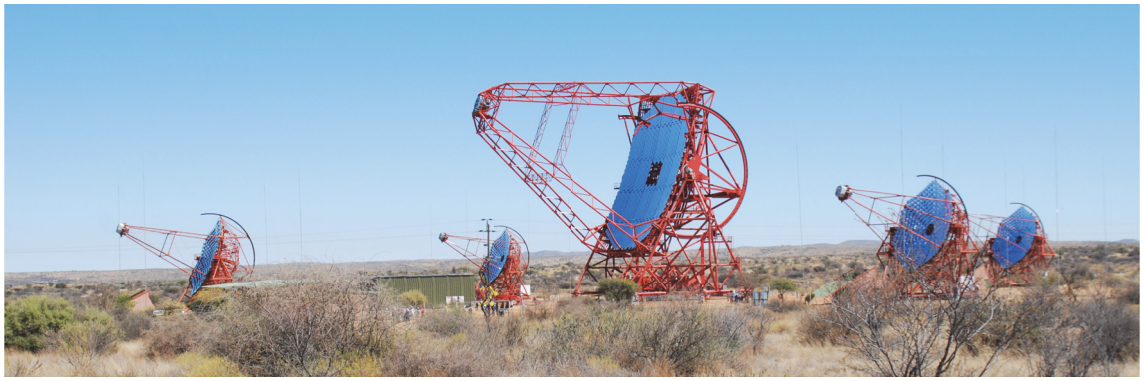

Fig. 3.1.: The H.E.S.S. telescopes.

The five H.E.S.S. telescopes are operated in Namibia, in the Khomas highland south-west of Windhoek. The location provides excellent observation conditions due to its very arid climate, the height of 1800 m above sea level, little light pollution, and a good visibility of the central part of the Galactic plane, which contains a large number and diversity of TeV γ-ray sources. Four of the telescopes form a square of 120 m side length and have collection areas of 107 m^2, built for a γ-ray energy range of hundreds of GeV to $\sim$100 TeV. They form Phase I of the system, which is operational since 2004. The fifth telescope was inaugurated in 2012, initiating Phase II of H.E.S.S. With its large mirror area of 614 m^2 and a more finely pixelated camera, it facilitates the detection of γ-rays with lower energies down to tens of GeV.
In this work, only data taken with the original four telescopes are used. In its 10-year history, more than 90 sources of TeV emission were discovered with H.E.S.S. Groundbreaking discoveries like γ-ray emission from supernova remnant shells (Aharonian et al. 2004), the first variable galactic TeV source (Aharonian et al. 2005), and TeV emission from a Starburst Galaxy (Acero et al. 2009) were made. H.E.S.S. collected a large amount of Phase I data of a variety of sources, under all kinds of observation conditions. The large number of observations and hence the event statistics of some of the brightest sources provide an extensive testing ground for systematic studies. Analysis methods have been developed and optimised to meet different objectives. In this chapter, the H.E.S.S. Phase I telescopes and the essentials of data taking, event reconstruction and analysis are described.

3.1. Telescopes and data taking

The main difficulty in taking data with IACTs is that the showers are faint and of short duration, while a multitude of sources of background exists. This section briefly describes how H.E.S.S. is designed to be as sensitive to γ-ray induced air showers as possible by filtering most of the background with a multi-level trigger system.
The size of the square that the telescopes are placed in allows for stereoscopic viewing of γ-ray induced air showers, but inhibits the triggering of multiple telescopes on Cherenkov

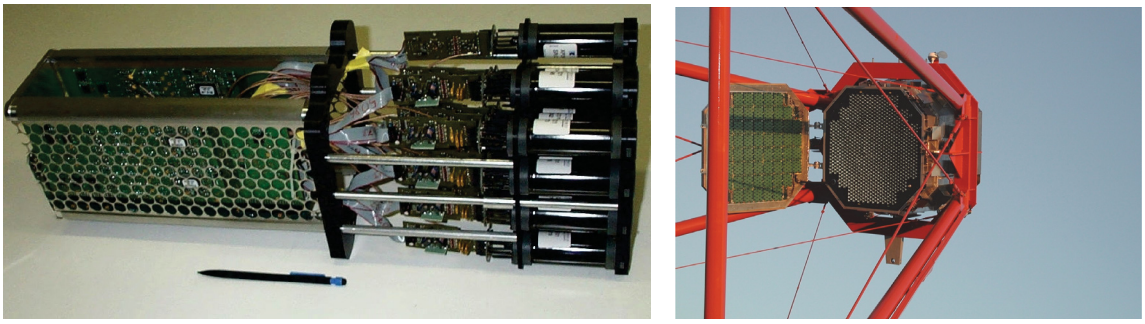

(a) (b)

Fig. 3.2.: (a) H.E.S.S. Phase I drawer. The PMTs are oriented towards the right, the electronic boards are on the left. (b) Phase I camera with opened lid. The visible layer is a sheet of Winston cones.

light produced by muons. Each telescopes' reflective area consists of 382 circular mirrors of 60 cm in diameter, forming a total light collecting area of 107 m^2. The mirrors and dish follow a Davies-Cotton design (Davies & Cotton 1957), which reduces abberations at angles far from the optical axis. A structure of four masts holds the camera in the focus, 15 m from the mirrors. The camera and masts cause a shadowing of the dish of ∼11% on average. Misalignments and deformation of the camera structure create systematic uncertainties of the order of 30" of the exact orientation of the telescopes. The camera has a field of view of 5° in the sky and consists of 960 photo-multiplier tubes (PMTs, see Fig. 3.2(a)). Each PMT is equipped with a Winston cone (Welford & Winston 1989) which collects and guides the light onto it, and closes the gaps between neighbouring PMTs. The Winston cones are visible in Fig. 3.2(b), which shows one of the H.E.S.S. cameras with its lid open. The quantum efficiency of the PMTs, i.e. the ratio of detected to incident photons, is 25% for wavelengths of 300 – 500 nm. The PMTs and the necessary electronics are organised in batches of 16, forming so-called drawers that have a common read-out and high-voltage supply. The PMTs are read out with three channels: one for the analog trigger signal, two for differently amplified signals to allow for a large dynamic range. The two amplified PMT signals are sampled with 1 GHz and temporarily stored. Upon a positive trigger decision both signals are read out.
The first level trigger takes place on camera level: A PMT (or pixel) counts as triggered, if a certain amount of photo-electrons (usually four or more) are registered. To not store electronic noise or single NSB photons, a trigger signal is only forwarded if a configurable amount of triggered pixels lies within a sector of 4×16 pixels. The camera trigger signal is sent to the *central trigger*, which requires a coincident trigger signal by at least two telescopes to store events. This reduces the data rate efficiently, since the overabundant muons are filtered out to a large degree. The remaining events, mostly consisting of electromagnetic and hadronic showers, are converted to digital signals and saved to disk. Typically, observations are made and stored in units of 28 minutes, called a run. The H.E.S.S. data acquisition is described in detail in Balzer et al. (2014).

3.2. Calibration

In the calibration step, the conversion from digital counts back to photo electrons is calculated, taking into account the imperfections of the detector. Furthermore, information

that is needed in the analysis is added, e.g., the orientation of each telescope.
Dedicated runs are used to determine the exact conversion factor of counts to photo electrons (*SinglePE runs*) and to account for differences in quantum efficiencies and conversion factors between the PMTs (*FlatField runs*). An important step of calibration is the determination of broken pixels. If bright stars pass through the camera, the affected PMTs are turned off in order to prevent damage by too high currents. Some pixels fail because of hardware defects, and sometimes the electronics of a complete drawer are out of order. These pixels are marked as (temporarily) broken and are not used in the analyses. If the number of broken pixels surpasses 15% in three telescopes, the run fails the quality criteria and is not used.
Two steps in the calibration will be presented in more detail, the determination of the *muon efficiency* and the *pointing corrections*. They are especially important for the direction reconstruction of single γ-rays, and thereby for the angular resolution.

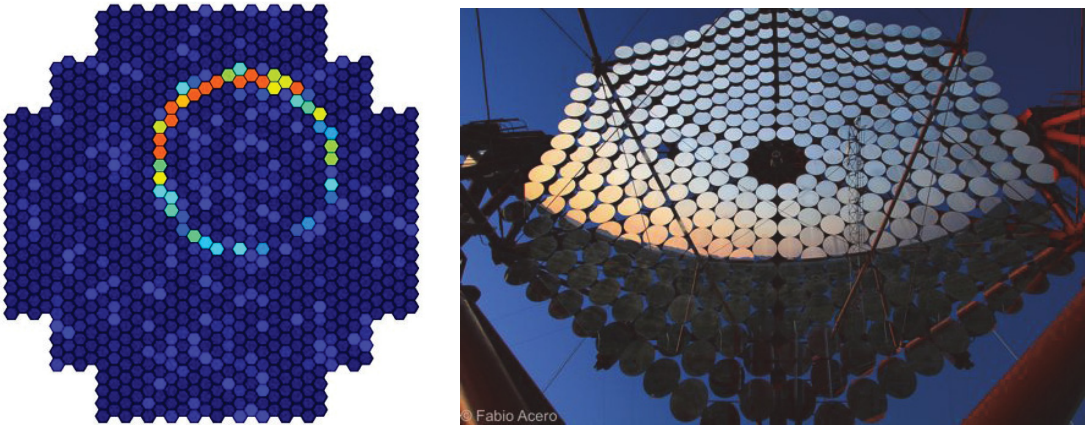

(a) (b)

Fig. 3.3.: (a) Muon ring in a H.E.S.S. camera. Image courtesy of M. de Naurois. (b) Dish with mirrors and visible opening for the *SkyCCD* on the upper left. The *LidCCD* is situated in the centre of the dish. Photograph courtesy of Fabio Acero.

Muon efficiency

To compare the optical efficiencies of the four telescopes with each other, muons are used. Although most muon events do not pass the *central trigger*, many of them are recorded because of their chance coincidence with γ-like events. Their Cherenkov radiation leaves ring-like images in the cameras, see Fig. 3.3. The properties of these so-called muon rings are well known: The Cherenkov angle depends on the velocity (which directly translates into the energy) and defines the radius of the ring in the camera. On the other hand, also the number of photons in a muon ring depends on the muon energy. Knowing the energy, the number of Cherenkov photons produced by a muon can be accurately predicted. The *muon efficiency* is defined as the ratio of detected to predicted photons. This number describes the optical efficiency of the whole system, including mirror reflectivity, shadowing effects by the camera and masts, winston cone efficiency and quantum efficiency of the PMTs. While the shadowing is a geometrical effect and therefore constant over time, dust accumulates in the Winston cones, and the PMTs and mirror surfaces are subject to degradation. However, it was shown that the quantum efficiency of the PMTs stays on a high level (de Naurois 2012), only the reflectivity of the mirrors suffers from abrasion by

dust and rain and ageing of the material. This tendency can be seen in Fig. 3.4, where the absolute optical efficiency of one of the Phase I telescopes is plotted against the run number, roughly corresponding to its development over time. The small upward jumps correspond to adjustments in high voltage supply, made in order to keep the conversion factor of analog counts to photo electrons constant. The recovery of the efficiency around run 61000 is caused by a replacement of the mirrors in 2010. In simulations of muon rings with a perfect mirror reflectivity, the ratio of measured to expected photons is $\sim$ 0.11 (Chalmé-Calvet et al. 2014). This ratio is used as the nominal efficiency and will be referred to as 100% (relative) muon efficiency in the following. Before the mirror replacement in 2010, the relative efficiency had degraded to less than 50% for some telescopes. The muon efficiency is an important parameter for the angular resolution, since it defines the light yield of the telescope. Thereby, an absolute energy calibration is introduced. The reconstructed energy of a γ-ray is one of its main properties and crucial for its direction reconstruction. In analyses and simulations, the mean relative efficiency of the four telescopes is used for an absolute energy calibration. With simulations of muon rings for different optical efficiencies, the systematic error on the efficiency by employing muon ring reconstruction was determined to be less than 5% at 40% efficiency, and less for higher efficiencies (private communication with R. Chalmé-Calvet). The statistical error ranges between 2% and 4%, depending on the calibration period, see Fig. 3.4.

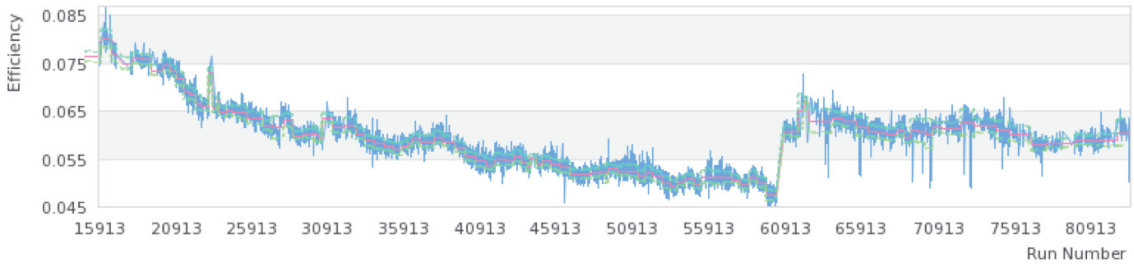

Fig. 3.4.: Optical efficiency of one of the H.E.S.S. Phase I telescopes depending on the run number. The pink line displays the mean muon efficiency calculated for the respective calibration period, the green lines are its 1σ errors. Figure taken from Chalmé-Calvet et al. (2014).

Pointing correction

Knowledge of the exact orientation of the telescopes is the basis of direction reconstruction in the sky. Dedicated *Pointing runs* are performed to calibrate the sky positions mapped in the cameras. The white lid of the cameras stays closed in these runs and is used as a screen on which stars are reflected by the telescope mirrors. Only small caps at the corners of the camera lid are opened - behind them, on the sheet with the Winston cones, red LEDs are positioned. In the mirror plane, two CCD cameras are installed: The *LidCCD* in the centre and the *SkyCCD* roughly three meters offset, see Fig. 3.3. The *LidCCD* is aligned to have the central part of the camera lid and at least two of the LEDs in its field of view, since the LEDs serve as reference points of the camera position. The *SkyCCD* is aligned parallel to the optical axis of the telescope. The principle of *Pointing runs* is to take pictures of bright stars with the *LidCCD* and *SkyCCD* simultaneously and to compare them, with respect to the LEDs. *Pointing runs* are taken twice per month. Bright stars that are distributed at different zenith and azimuth angles are tracked for one minute, while the CCD pictures are taken. In the calibration, the misplacement of the

stars in the pictures is used to calculate correction parameters for a mechanical model that predicts the bending of the steel structure, torsion of the camera mast, etc. depending on the altitude-azimuth orientation of the telescope. The corrected model is applied to all camera positions of the observation period. With this procedure, a pointing accuracy of 20" per axis is reached (Gillessen 2004), corresponding to a radial accuracy of 28.3". A much higher accuracy of 6" per axis is reached when the *SkyCCD* and *LidCCD* take pictures during an observation and the corrections can be applied run by run (Braun 2007).

3.3. Reconstruction

The reconstruction of properties of the initial γ-rays from the shower images that are stored in the calibrated "raw data" is the central part of the analysis. Traditionally, an analysis with Hillas parameters is used in VHE γ-ray astronomy since its invention in 1985 (Hillas 1985). The parametrisation assumes an elliptical form of shower images and uses its characteristics, i.e. the ellipses' width, length, centre of gravity, angular orientation and position in the camera, to reconstruct the shower direction (see left panel of Fig. 3.5) and to classify the shower properties. By comparison with tabulated, typical shower properties from γ-ray simulations, the properties of the original particle are determined and hadronic showers can be rejected due to their irregular shape.

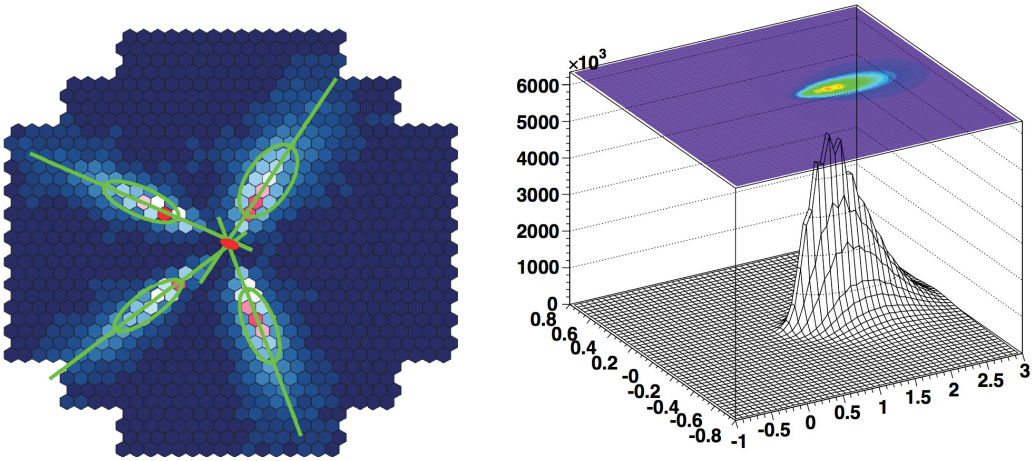

(a) (b)

Fig. 3.5.: (a) Direction reconstruction from a shower parametrisation with Hillas ellipses, taken from Balzer (2010). Four camera images of the same γ-ray shower are superimposed in a common camera plane, the green ellipses show the Hillas parametrisation of the intensity distributions. The estimated source region lies at the intersection of the axes of the ellipses and is depicted as a red error ellipse. (b) Shower template used in the *Model Analysis*, taken from de Naurois & Rolland (2009).

In the *Model Analysis* by de Naurois & Rolland (2009), which is used in this work, a Hillas parametrisation is only employed to set initial parameters for a more advanced fit. The *Model Analysis* is based on a simultaneous fit of shower templates to all available camera images. The templates are generated from a semi-analytical model that describes the lateral, longitudinal and angular distribution of charged particles in electromagnetic air showers, and the corresponding distribution of Cherenkov light. Templates are gener-

ated for a wide range of zenith angles, energies of the primary γ-ray, primary interaction depths and impact distances. They are stored as 2D distributions of photon densities in the camera plane (see right panel of Fig. 3.5), in tables with all of these parameters as dimensions. Between the table entries, shower images are linearly interpolated. The comparisons with the actual camera images are accomplished by calculating pixel-wise intensities and employing a Log-Likelihood maximisation with the Levenberg-Marquardt Algorithm (Levenberg 1944; Marquardt 1963). The fit parameters contain the direction and energy of the initial particle, and the errors on these two quantities reflect the quality of the reconstruction. More importantly, the quality of the fit, i.e. how good the shower can be described by a γ-ray induced shower template, is an effective measure to separate γ-induced showers from hadronic ones. For the whole camera, the *Goodness* can be calculated from the log-likelihood values in the pixels i:

$$G = \sum_i \frac{\ln L(s_i, \mu_i) - \langle \ln L \rangle|_{\mu_i}}{\sqrt{2N_p}} \tag{3.1}$$

where $\ln L(s_i, \mu_i)$ is the log-likelihood of observing s_i photo-electrons in a pixel when μ_i are expected, $\langle \ln L \rangle$ is the expectation value of $\ln L$ assuming μ_i photo-electrons were measured, and N_p is the number of working pixels in the camera. The *Shower Goodness* (SG) is calculated with the same formula by only including pixels that are attributed to the shower[1] and two adjacent rows. However, the SG in this form depends on the observation conditions and the total image intensity in the respective camera. Therefore, lookup tables containing the mean values $\langle G \rangle$ and width σ_G of SG distributions depending on zenith angle, impact distance and total image intensity are created from simulations. The dependencies are taken care of when calculating the *Mean Scaled Shower Goodness* for all telescopes t,

$$MSSG = \sum_t \frac{SG_t - \langle SG \rangle}{\sigma_{SG}\sqrt{N_t}}, \tag{3.2}$$

N_t being the number of telescopes. This value is used as the primary γ-hadron separation parameter. Other parameters that are used in the event selection are the *Background Goodness* (BG) and the *NSB Likelihood* (NSBL). To calculate the *Background Goodness*, the *Goodness* defined in eq. 3.1 is calculated only for pixels outside of the shower. It is sensitive to hadronic clusters and other irregularities. Opposed to the likelihood of the γ-ray template fit, a likelihood for the event being noise (or NSB) is calculated by setting μ_i to 0 in eq. 3.1.

Different cuts have been developed for different purposes. The basic requirements for an event to pass are a minimum number of photo-electrons (p.e.) in the camera image, and a maximum distance of the centre of gravity of the shower from the camera centre (*nominal distance*) of 2° , which prevents the usage of incomplete or distorted shower ellipses at the camera edges. Only events with a *telescope muliplicity* $\geq$2 are accepted for reconstruction, i.e. the shower images in at least two cameras must pass the previous two cuts. This procedure is crucial for the direction reconstruction: The minimum telescope multiplicity guarantees that the event is reconstructed stereoscopically, and the nominal distance cut prevents the usage of incomplete or distorted shower ellipses at the camera edges. The minimum image intensity cut rejects small and faint events. Since shower images are bigger and brighter if the energy of the initial γ-ray is high, this cut indirectly introduces

[1] Two thresholds can be set to define the shower: A pixel is attributed to the shower if its photo-electron number surpasses the higher threshold and at least one of its neighbours surpasses the lower threshold, or if it surpasses the lower threshold and at least one of its neighbours surpasses the higher threshold. In this work, the standard thresholds of 5 and 10 photo-electrons were used.

a minimum event energy. A cut on the primary depth reduces showers produced by electrons, which on average start emitting Cherenkov radiation higher in the atmosphere.

Table 3.1.: Cut parameters and their values for Std, HiRes and Faint cuts in the *Model Analysis*.

configuration	min. p.e.	max. MSSG	max. NSBL	max. BG	max. direction error	min. primary depth
Std	60	0.6	-1	2	-	-1
HiRes	60	0.6	-1	2	$<0.03^\circ$	-1
Faint	120	0.4	-1	2	-	-1

To achieve a high data quality, but also high significances for most sources, the cut configuration *Standard* (Std) has been developed, see de Naurois & Rolland (2009). The cut parameters and their values are listed in Table 3.1. To give an example of the rejection power of the cuts, a typical run on the Crab Nebula is contemplated. Out of the events that trigger the telescopes, 1% passes the Std cuts.
For a higher quality of direction reconstruction, *High Resolution* (HiRes) cuts have been introduced, which additionally reject all events with direction errors $> 0.03^\circ$, leaving only 0.1% of the events from the run mentioned above. *Faint* cuts were originally developed for faint sources, as the name says. The requirements for an event to pass this selection are stricter than for Std cuts - only 0.5% of the events that triggered are classified as γ-rays. Due to the larger and brighter shower ellipses and the better compatibility with a γ-ray shower template, the direction reconstruction of events passing Faint cuts is more precise. Also for HiRes and Faint configurations, the cut values are presented in Table 3.1.

3.4. Detection of sources and background estimation

Despite the rejection cuts presented in the last section, a relatively high background level persists even for the strongest sources. The remaining background consists mostly of hadron- and electron-induced showers that look like γ-ray events, but also diffuse γ-ray emission (e.g. in the Galactic plane, see H.E.S.S. Collaboration et al. 2014a). To detect a source, the fact that the background is more or less evenly distributed, while γ-rays come from distinct sources, is used. The number of events attributed to a source, the *excess*, is calculated as the difference in event numbers between the source region (also called analysis region, or ON region) and a γ-ray source free control region (the OFF region):

$$N_E = N_{\mathrm{ON}} - \alpha N_{\mathrm{OFF}}, \tag{3.3}$$

α being a normalization factor taking into account different exposure times, sizes of the regions and the detector responses in the regions. In particular, the acceptance of the cameras, i.e. the ability to register particles, depends on the distance from the camera centre. Following Eq.17 in Li & Ma (1983), the significance of a detection is then given by

$$S = \sqrt{2}\left\{ N_{\mathrm{ON}} \ln\left[\frac{1+\alpha}{\alpha}\frac{N_{\mathrm{ON}}}{N_{\mathrm{ON}}+N_{\mathrm{OFF}}}\right] + N_{\mathrm{OFF}} \ln\left[(1+\alpha)\frac{N_{\mathrm{OFF}}}{N_{\mathrm{ON}}+N_{\mathrm{OFF}})}\right]\right\}^{1/2}. \tag{3.4}$$

There are several methods to estimate the background and to calculate the corresponding factor α. Two of them, the *Reflected Region* and the *Ring Background* method, are used

in this work. While the *Reflected Region* method is suitable for one-dimensional representations of sources, the *Ring Background* method is used to obtain two-dimensional maps. Both methods are briefly explained in the following.

For the *Reflected Region* method (Berge et al. 2007), observations have to be taken in *wobble mode*, meaning that the telescopes are not pointed at the source directly, but with an off-axis angle of typically $0.5° - 1.5°$. The advantage is that ON and OFF regions with the same size and distance to the camera centre can be determined for each run (see Fig. 3.6(a)), rendering a radial acceptance correction for α not necessary. To get a stable estimate with as little statistical fluctuations as possible, multiple OFF regions are defined, added and weighted. Around the ON region, a circular region is excluded from the background estimation to avoid contamination with the γ-ray emission of the source. For the same reason, other sources of γ-ray emission in the field of view are excluded. Alternating wobble positions in positive and negative right ascension (RA) and declination (Dec) directions around the source are chosen to compensate gradients in the field of view and to get a good background estimate in spite of exclusion regions. Typically, the wobble offset for point-like sources is $0.5°$ or $0.7°$, restricting the size of the analysis region accordingly. For spectral analyses of point sources, the size of the analysis region is chosen to be $0.1°$ in the Std and HiRes configuration and $0.07°$ for Faint cuts. These ON region sizes optimise the detection significance for the respective cut configuration. They allow for a large number of OFF regions, rendering the background estimation stable and the ratio of ON to OFF events high.

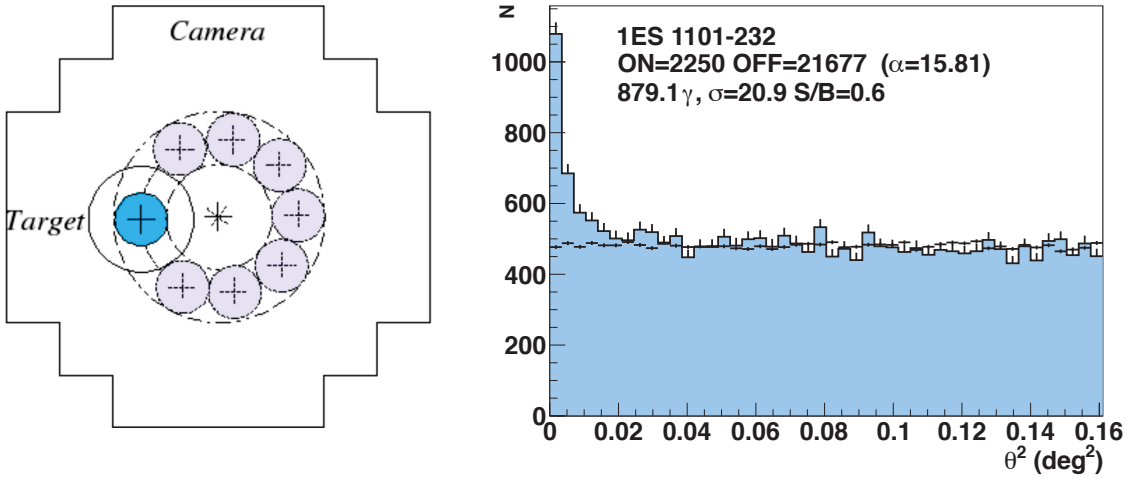

(a) (b)

Fig. 3.6.: (a) Schematic of the *Reflected Regions* background method, courtesy of M. de Naurois. The filled cyan circle symbolises the ON region, the filled light blue circles the OFF regions. (b) θ^2 plot of 1ES 1101−232, a rather faint extragalactic source. The blue filled histogram depicts the ON data, the black crosses are accumulated OFF data, scaled with α.

The spatial distribution of ON, OFF and excess events can be visualised in θ^2 plots. These are one-dimensional histograms displaying the squared radial distribution of events,

$$\theta^2 = (x - x_0)^2 \cos(y_0)^2 + (y - y_0)^2, \tag{3.5}$$

with (x, y) being the event positions in (RA,Dec) and $\cos(y_0)$ accounting for the transfor-

mation of equatorial coordinates to a plane. For the ON region, (x_0, y_0) are the coordinates of the target position, while for OFF regions (x_0, y_0) is the centre of the respective region. The events are accumulated in separate histograms, see Fig. 3.6(b). The excess distribution is calculated by subtracting the normalized OFF histogram from the ON histogram.

In the *Ring Background* method (Berge et al. 2007), an annulus around the source is chosen as OFF region, see Fig. 3.7(a). Since the ring covers regions with different distances to the camera centre, the *camera acceptance* to γ-rays has to be taken into account when calculating α. The acceptance is calculated by multiplying binned camera maps of the weighted and summed run-wise camera exposure with event count maps. As in the *Reflected Region* method, sources of γ-rays are excluded from the calculation. When observations are done in *wobble mode*, the position of the excluded regions in the camera changes, allowing to fill the holes in the acceptance map. The advantage of the *Ring Background* method is its applicability to every point in the field of view. This allows for the representation of spatial distributions of the excess and the significance in bi-dimensional sky maps, see Fig. 3.7(b).

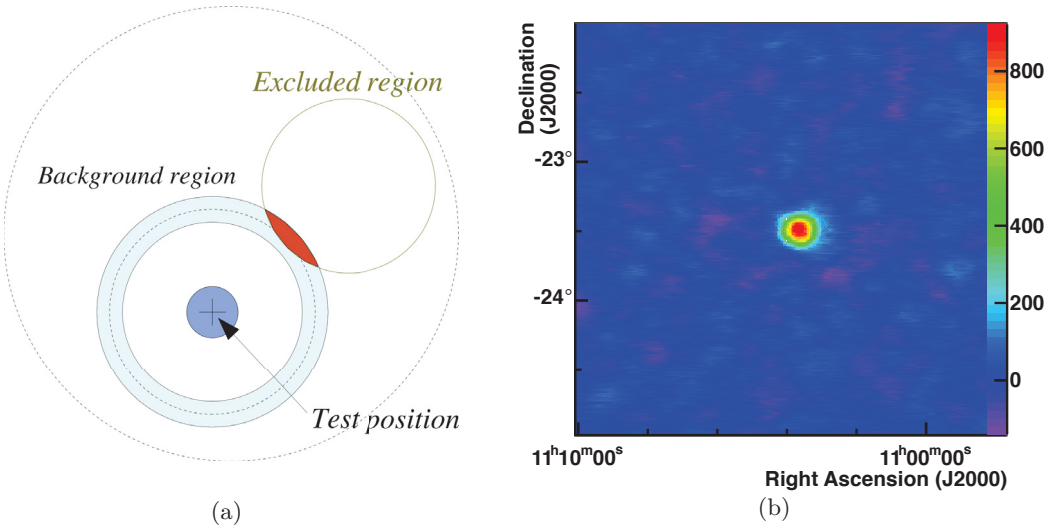

(a) (b)

Fig. 3.7.: (a)Schematic of the *Ring Background* method. The filled cyan circle depicts the ON region, the light blue annulus is the OFF region. An excluded part of the OFF region is marked red. Image from the H.E.S.S. internal documentation by M. de Naurois.(b) Excess map of 1ES 1101−232, produced from the same data set at the θ^2 plot in Fig. 3.6(b). The colour scale represents the number of excess counts after a smoothing was applied to the counts map.

The source morphologies visible in both θ^2 plots and sky maps are a convolution of the intrinsic shape of the γ-ray emission with the angular detector response, i.e. the *Point Spread Function*(PSF). To access the intrinsic source morphologies, knowledge of the PSF is indispensable. Before describing its properties and dependences in Chapter 4, the determination of one of its crucial parameters, the slope of the energy spectrum of the reconstructed γ-ray source, is described in the next section.

3.5. Spectra

Besides the direction, the energy of a γ-ray is its most important property. The spectrum, i.e. the differential photon flux over energy, gives insights on the acceleration/emission processes inside of a γ-ray source. However, the observed distribution of event energies from a source does not equal the distribution reaching the atmosphere since it is convolved with energy-dependent detector properties, most importantly with the *effective area* and the *energy resolution*. Both effective area and energy resolution also depend on observation conditions (zenith angle, off-axis angle, azimuth angle), detector properties (number of participating telescopes, muon efficiency), the reconstruction and the analysis method. All of these parameters will be represented by C in the following.
The effective area $\mathcal{A}$ is the surface integral of the probability to detect a particle on ground. It is calculated from simulations of γ-rays at fixed energies E as the ratio of particles n_γ passing the chosen analysis cuts to the overall number of simulated particles n_{sim}, multiplied with the simulated detection area $\mathcal{A}_{sim}$:

$$\mathcal{A}(E, C) = \frac{n_\gamma}{n_{sim}} \mathcal{A}_{sim} \tag{3.6}$$

The energy-dependent effective areas are stored in multi-dimensional tables for the different observation conditions, allowing for interpolation in the whole parameter space. A typical distribution of the effective area versus the energy and the zenith angle of the observation is shown in Fig. 3.8(a).

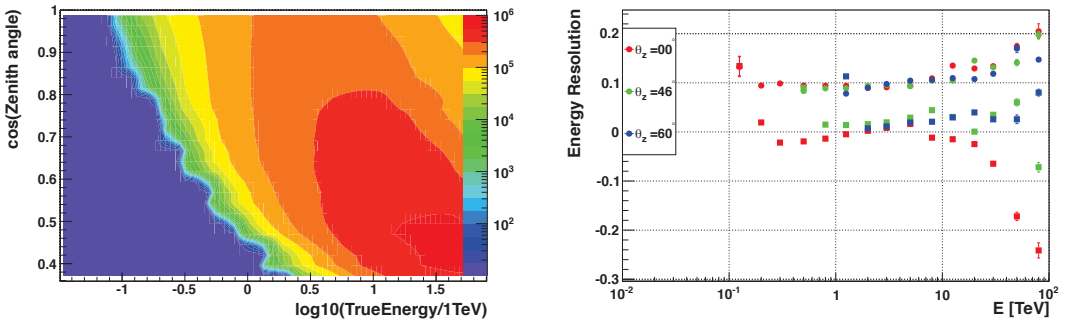

(a) (b)

Fig. 3.8.: (a) Effective detection area for a *Model Analysis* (Std cuts) at an off-axis angle of 0.5° , a muon efficiency of 100% and azimuth angle of 180° , depending on energy and zenith angle. (b) Energy resolution and bias of the energy reconstruction for the same analysis. Filled circles display the resolution, squares the relative bias. The different colours represent zenith angles of 0° (red), 46° (green) and 60° (blue). Note the shift in the energy threshold to higher energies with increasing zenith angle.

At the lowest energies, the reconstructed event statistics become insufficient, leading to effective areas of zero and irregularities in the tables, which are visible as the rippled region. To avoid this regime in the spectrum calculation, an energy threshold is introduced. Since the rise of the acceptance with energy depends on the observation conditions, the threshold is chosen to be positioned dynamically. In this work, the energy at which the effective area curve reaches 15% of the maximum effective area is chosen as the threshold. For example, when looking at the left panel of Fig. 3.8, the energy threshold would be positioned approximately at the transition form green to yellow colours.

The energy resolution function $\mathcal{R}$ is the probability density of reconstructing an energy E given an event with a true energy E'. In practice, this distribution is simply the reconstructed energy distribution of mono-energetic γ-ray simulations. In addition to a smearing of the energy, the mean of the distribution can be shifted. The offset between simulated and reconstructed mean energy is called *energy bias*. Both the width of the smearing and the bias depend strongly on the observation conditions. As an example, the zenith angle dependence is visualized in Fig. 3.8(b). In the same manner as the effective areas, the energy resolution functions are stored in multi-dimensional tables that allow for interpolation.
With $\mathcal{A}$ and $\mathcal{R}$ given, the expected number of events n_γ in an energy bin $[E_1, E_2]$ can be calculated as

$$\mathrm{n}_\gamma = \int_{E_1}^{E_2} dE \int_0^\infty \Phi(E') \times \mathcal{A}(E', C) \times \mathcal{R}(E', E, C)\, dE', \tag{3.7}$$

where Φ denotes the flux of the observed source depending on the true energy E'. The spectrum $\Phi(E')$ can take different forms, the simplest model in use is a power law:

$$\Phi(E') = N_0 \left(\frac{E'}{E_0}\right)^{-\Gamma} \tag{3.8}$$

The normalisation N_0 is the flux at the reference energy E_0, the spectral index Γ reflects the steepness of the slope. The description with a power law is robust and sufficient for many sources. Other models that proved to describe the energy spectra of TeV γ-ray sources in more detail are a curved power law,

$$\Phi(E') = N_0 \left(\frac{E'}{E_0}\right)^{-\alpha-\beta \ln \frac{E'}{E_0}}, \tag{3.9}$$

and a power law with an exponential cut-off,

$$\Phi(E') = N_0 \left(\frac{E'}{E_0}\right)^{-\Gamma} \exp\left(-\frac{E'}{E_c}\right) \tag{3.10}$$

Assuming Poissonian distributions for the number of γ-like and background events in each energy bin, a binned likelihood fit is performed to determine the parameters of the spectral model best describing the observed distribution. The result of such a fit is shown in Fig. 3.9. The figure contains the best-fit power law to the convolved ("forward-folded") energy distribution of 1ES 1101−232 and spectral points, which are calculated from the difference of measured event number in an energy interval, N_{obs}, compared to the expected event number from the best-fit model, N_{exp}. The normalised difference $(N_{obs} - N_{exp})/N_{exp}$ is shown in the residual plot below. According to the fit, the differential flux and the corresponding statistical errors at 1 TeV are $(5.5 \pm 0.5) \cdot 10^{-13}\,\mathrm{cm}^{-2}\,\mathrm{s}^{-1}\,\mathrm{TeV}^{-1}$, and the spectral index is 3.0±0.1. In Aharonian et al. (2006a), the systematic errors on the flux and on the spectral index were estimated to be 20% and 0.1, respectively.

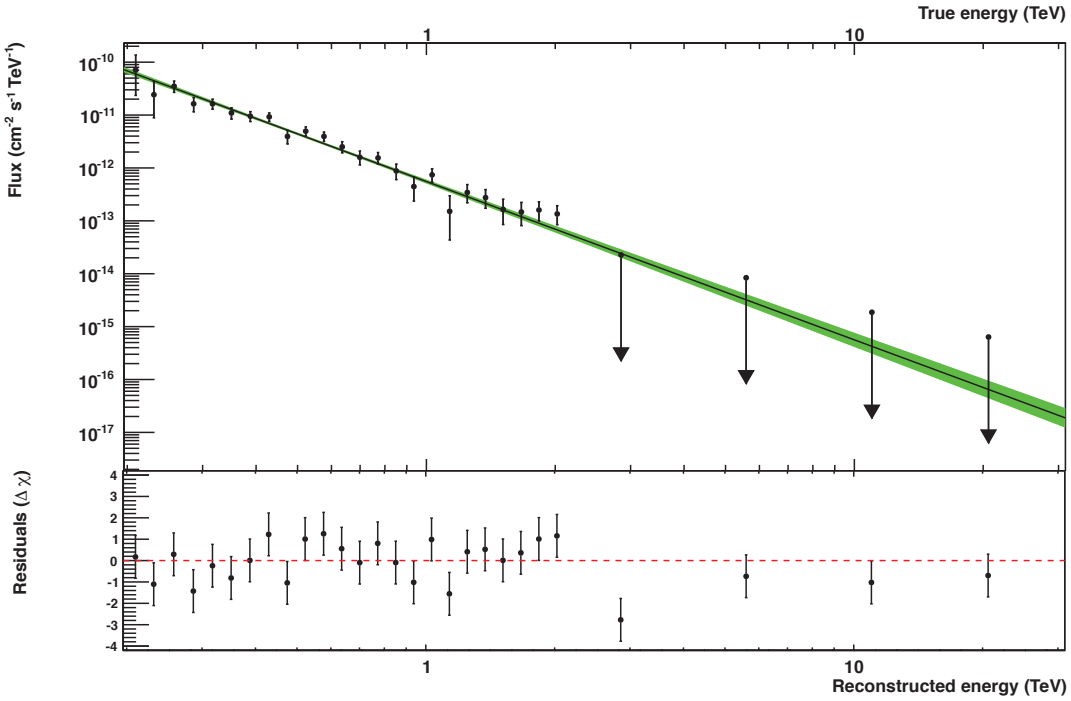

Fig. 3.9.: Energy spectrum and residuals of 1ES 1101−232. The black line represents the power law model that fits the convolved data best. Upper panel: The green area around it marks the 1σ confidence interval of the fit. Black points denote the measured flux per energy bin, where the binning was chosen so that a significance of 2σ is reached for each data point. The arrows represent upper limits in the bins without significant flux measurement. Lower panel: The residuals of the spectrum.

4. Point Spread Function

The Point Spread Function (PSF) is the angular response of an imaging system to a point source. It describes how photons from an infinitesimally small region in the sky are spatially reconstructed by the instrument. The angular response spreads the image of the point source, and the degree of spreading is a measure for the quality of the imaging. In Fig. 4.1, the H.E.S.S. PSF is visualized by the spreading of PKS 2155−304, a distant AGN. The optical image of the source and its surroundings are shown for comparison, to give an impression how much the resolution of IACTs differs from that of other astronomical imaging devices. The images in the middle and on the right were produced from all H.E.S.S. runs on PKS 2155−304 that were taken with four telescopes. The source was chosen because of its extremely high event statistics – its point-like nature is under debate (see Chapter 6).

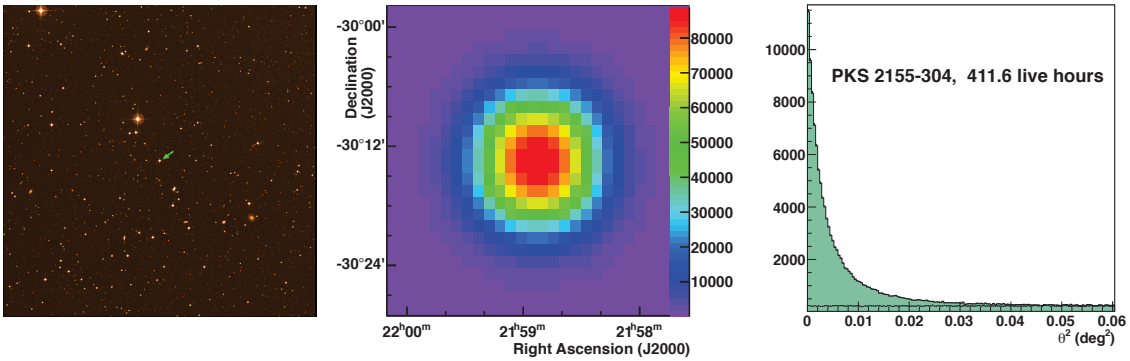

Fig. 4.1.: The AGN PKS 2155−304 in an optical image (left, pointed at by the green arrow), a H.E.S.S. excess skymap of the same field of view (middle) and a θ^2 plot. The optical image and the skymap both have a size of 0.5 deg × 0.5 deg. In the θ^2 plot, the lower thin black markers display the distribution of OFF events, while the filled green histogram displays the distribution of ON events. The maximum value is $\theta^2 = 0.06\,\mathrm{deg}^2$, corresponding to an angular distance of 0.25 degrees from the optical centre of PKS 2155−304. The optical image is provided by Landessternwarte Heidelberg, see http://www.lsw.uni-heidelberg.de/projects/extragalactic/charts.

In the case of IACTs, the degree of spreading is usually quantified by calculating the radius containing 68% of the reconstructed events of a simulated point-like γ-ray source, r_{68}. Since the imaging system in ground-based VHE γ-ray astronomy consists not only of the telescopes but also of the atmosphere and the reconstruction and event selection algorithms, its response function is influenced on all of these levels. Accordingly, the response function can be divided into an "atmospheric", a "telescope" and an "analysis" part. All of them are reflected as different steps in the MC simulations of γ-rays used to obtain a theoretical H.E.S.S. PSF. Subsequently, an overview of the limitations and dependencies of the PSF will be given on the three levels mentioned above, and the simulation procedure will be described in parallel. The calculation of a theoretical PSF and its use in the

determination of source sizes are presented in Sec. 4.1 and 4.2, respectively. The actual PSF of the H.E.S.S. instrument can be assessed by observations of point-like sources. The choice of such sources and a comparison with the expected PSF is presented in Sec. 4.4. In Sec. 4.5, possible reasons for and dependencies of a mismatch between the expected and the actual PSF are systematically studied.

However, first of all, the dependence of the PSF on the energy of the primary γ-ray is discussed since it is decisive on all three levels. The causal relationship is evident from the considerations in Chapter 2: Showers originating in γ-rays with higher energies are larger and hence produce more Cherenkov photons. Since the relative shower fluctuations are comparatively smaller, the camera images are better determined, which makes their reconstruction more precise. This fundamental dependence is shown in Fig. 4.2(b). In this work, as in most H.E.S.S. analyses, the PSF is not calculated for individual event energies, but for a spectrum of γ-ray events from a source. In a first approximation, the energy distributions of VHE γ-ray sources can be described by a power law as presented in Eq. 3.8. Typical values for the **spectral index** are $\Gamma = 2.0 - 3.5$. The higher the spectral index, the higher the relative number of events with low energies, which leads to a broadening of the overall PSF. Nevertheless, detector properties and the reconstruction method influence the dependence of the PSF on the energy significantly, as will be shown in the following. An example of the resulting dependence of the PSF on the spectral index is shown in Fig. 4.3(b). In PSF calculations from MC simulations, the spectral index determines the number of simulated γ-rays per energy.

Atmosphere

The angular resolution of IACTs is naturally limited by the statistical processes of shower formation in the atmosphere. As described in Chapter 2, from the first interaction of a primary particle to the emission of Cherenkov light, such processes are particle decay and generation, Compton scattering, bremsstrahlung, pair-production, electron-positron annihilation, BhaBha and Møller scattering. Rayleigh and Mie scattering, which lead to an absorption of Cherenkov light in the atmosphere, are also statistical processes.
All of these interactions introduce an ambiguity into the reconstruction of the properties of the primary particle. They are simulated in the first step of MC generation, which employs the well-established KASKADE code (Kertzman & Sembroski 1989). The energy thresholds for the different processes, lifetimes and masses of all particles involved as well as the magnetic field and the density profile of the atmosphere are crucial parameters in KASKADE. The atmospheric profile typically used for H.E.S.S. simulations is a model consisting of several layers based on measurements performed in Namibia. Alternatively, summer and winter versions of the atmospheric profile exist, developed from measurements in February and June. The output of KASKADE consists of the coordinates, direction, wavelength and time of arrival of the Cherenkov photons on the ground. In order to obtain the H.E.S.S. PSF, only γ-rays are simulated.
Fig. 4.2(a) visualises how different atmospheric air showers can look although they are all induced by γ-rays with the same energy and under the same conditions. The minimum PSF size possible for IACTs, assuming that all Cherenkov photons are detected, was estimated by Hofmann (2006) by employing similar simulations. The main result of their studies is a fundamental limit for directional reconstruction employing Hillas ellipses, shown in Fig. 4.2(b). The resolution shown in the plot is given as the width of a Gaussian that was fitted to the distribution of reconstructed event directions.
In addition to the energy dependence, the **azimuth angle** dependence of the PSF is shown

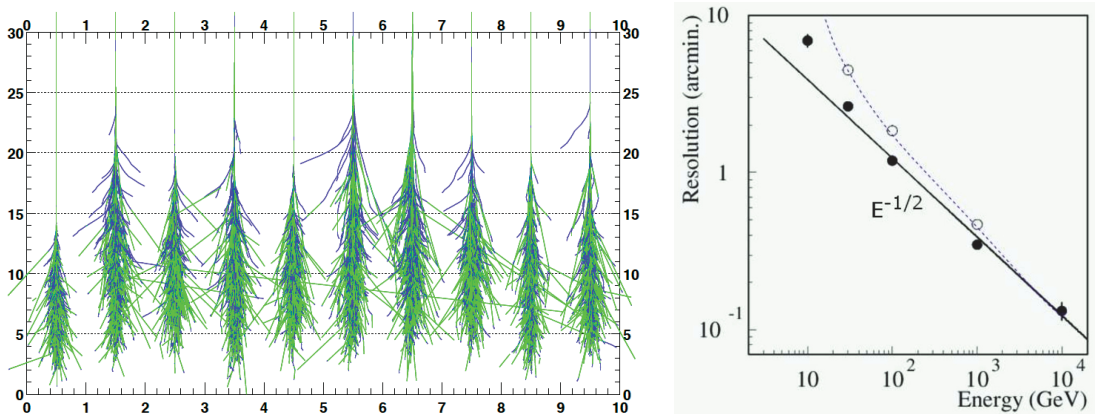

(a) (b)

Fig. 4.2.: (a) Simulations of atmospheric interactions induced by a γ-ray with an energy of 300 GeV. Photon tracks are shown in green, tracks of electrons/positrons in blue. Only particles with energies larger than the critical energy are included. The x- and y-axes are given in is given kilometers on the ground and above sea level, respectively. Courtesy of de Naurois (2000). (b) Angular resolution as a function of γ-ray energy assuming 100% Cherenkov photon collection efficiency. Filled black circles denote simulations without magnetic field or the North direction at the H.E.S.S. site, empty circles show the resolution for the South direction. Figure taken from Hofmann (2006)

in Fig. 4.2(b). The Earth's magnetic field deflects charged particles in electromagnetic showers and thereby separates positrons from electrons. The larger the angle between the magnetic field vector and the direction vector of the shower, the stronger the separation. At the H.E.S.S. site, the magnetic field lines deviate from the geographic north-south axis by an angle of 13° and point into the ground at an angle of 65° . Therefore, showers originating from the South at high zenith angles are widened the most. Since the Cherenkov radiation reflects the distribution of charged particles, the shower images in the cameras are fainter and less elongated, which leads to larger errors in the direction reconstruction. In addition, due to positron-annihilation, the charge-separated showers are not symmetric and the their images appear slightly rotated when seen under certain angles (Commichau et al. 2008). All in all, the reconstruction of showers from the South (azimuth = 180°) is less accurate than of showers from the North (azimuth = 0°), causing a difference in r_{68} of up to 15% at high zenith angles. Showers caused by γ-rays with lower energies are more prone to this effect.

The development of showers in the atmosphere is also dependent on the **zenith angle**. The higher the zenith angle, the larger the atmospheric depth between the first interaction of the primary particle and the telescopes. Especially for showers originating from γ-rays with GeV energies, which reach their shower maximum at rather low atmospheric depths, the number of Cherenkov photons that reaches the Earth becomes smaller. This renders it more difficult, or, below a zenith-dependent energy threshold, impossible to reconstruct the shower. In addition, the inclination to the magnetic field lines increases at large zenith angles, leading to the distortions in shower images described above. On the other hand, showers become more elongated since the gradient of atmospheric density becomes flatter along their way and for events with energies distinctly above the threshold, the effective area increases at high zenith angles. The spectral index, the azimuth angle and the zenith angle are the main parameters in the KASKADE simulations.

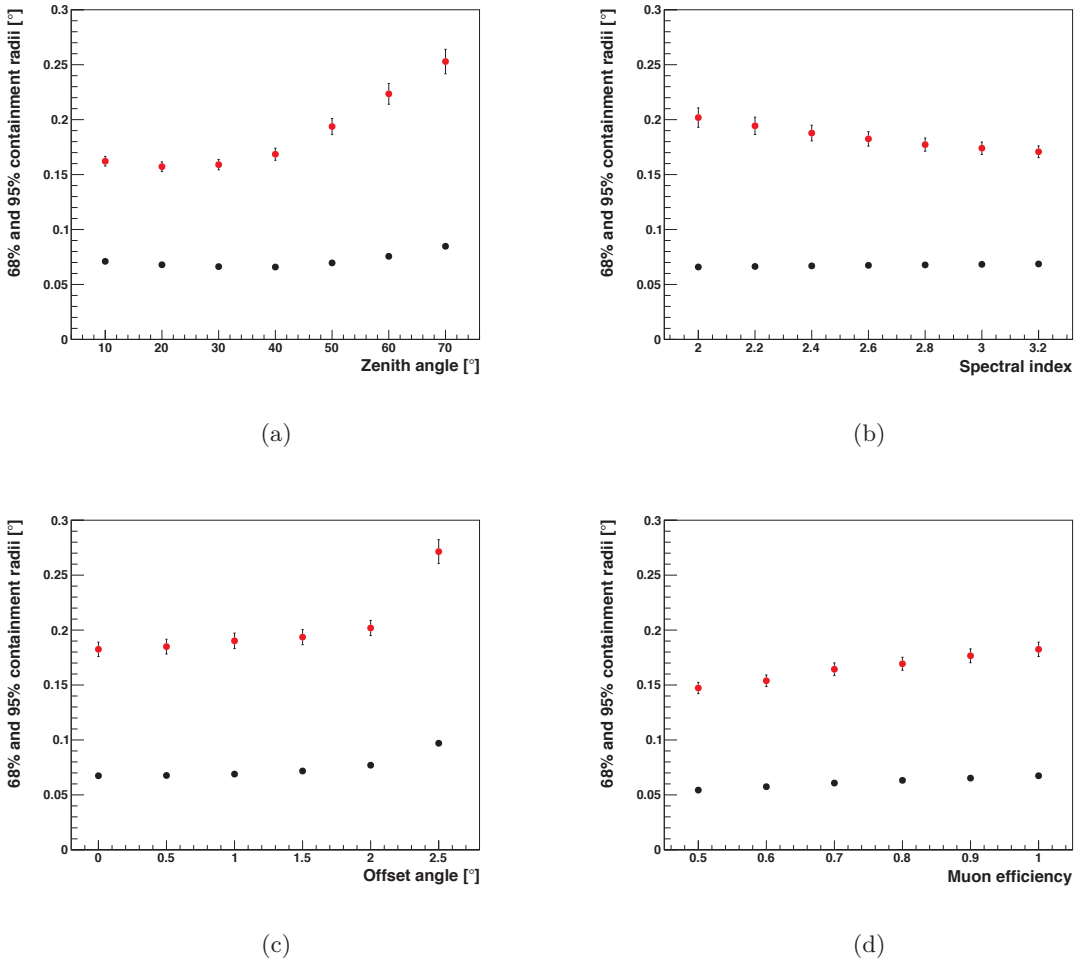

Fig. 4.3.: Dependence of the MC PSF on (a) the zenith angle, (b) spectral index, (c) offset angle and (d) muon efficiency. Black circles denote the 68% containment radius r_{68}, red circles the 95% containment radius r_{95}. If not varied, the simulated observation conditions are a zenith angle of 46°, an offset angle of 0° , a spectral index of 2.6 and a muon efficiency of 100%.

Telescope

The second step in H.E.S.S. Monte Carlo simulation is a telescope response simulation called SMASH (Guy & de Naurois 2014), which reproduces all the properties of the telescopes, the cameras and the read-out electronics. These properties, e.g. the number of telescopes, their mirror areas, optical and electronic efficiencies etc., limit how much of the Cherenkov light produced by a shower can be detected. Simulations demonstrating the effect of mirror areas and pixel sizes on the PSF are given in Hofmann (2006), for example. In addition, the limited field of view affects the energy dependence of the PSF: If the showers become too large, their images in the H.E.S.S. cameras are truncated and the missing information leads to larger uncertainties in the reconstructed direction. Therefore, r_{68} increases at high energies.
Also the **off-axis** angle of an observation has a direct effect on the PSF and is taken into account as a parameter in SMASH. For off-axis angles $\geq 1.5°$, the PSF deteriorates

due to truncation of shower images on the camera edges and the nominal distance cut. By comparison, the broadening of the optical PSF of the mirror towards its outer edges is negligible since the optical PSF stays smaller than the camera pixel size under all conditions (Jung 2003).
The **muon efficiency** as described in Sec. 3.2 is another parameter in the simulations. At first, it seems surprising that a low muon efficiency seems to lead to a better PSF, as depicted in Fig. 4.3(c). In fact, this effect is caused by the increase of energy threshold with lower optical efficiency: Low-Energy showers do not trigger enough pixels if the mirror reflectivity is low.
In SMASH, the Cherenkov photons of a KASKADE shower are converted to "photon bunches" in each telescope's coordinate system and propagated to the camera via a detailed ray-tracing simulation of the dish structure with all mirrors and masts. The simulated camera, including Winston cones, PMTs and the corresponding quantum efficiencies, registers how many photo-electrons are produced in each pixel and saves this number together with the photon arrival times. Next, the electronic response of the camera and the conditions of the different trigger levels as described in Sec. 3.1 are simulated. A simulated NSB with a frequency of 100 MHz per pixel (typical for observations of the Crab Nebula, for example) adds a realistic level of noise to the photo-electron numbers. In the end, the intensities in each camera pixel are obtained as an equivalent to raw data and the MC simulations can be treated just like real data, except for the missing hadronic and leptonic background.

Analysis

Finally, the PSF depends on the reconstruction method and on the event selection cuts. A Hillas-type analysis cannot compete with a more sophisticated method like the *Model Analysis*, see Fig. 4.4(a). This figure also illustrates that the different reconstruction algorithms introduce different energy dependencies on the PSF.
To achieve an even smaller PSF size, additional cuts can be introduced, e.g. the HiRes cuts presented in Sec. 3.3. A comparison of the simulated PSF for Std, Faint and HiRes cuts is shown in Fig. 4.4(b). While the Std and Faint configurations lead to a similar distribution, the HiRes PSF is significantly more narrow.

In Fig. 4.3, the dependences of r_{68} and r_{95} on some of the parameters mentioned above are shown. While r_{68} is a good measure of the "core" of the PSF, r_{95} (the radius within which 95% of γ-ray events are contained) reveals that it has "tails" that reach out to 0.03° under certain observation conditions. Obviously, these two radii do not always show the same dependencies, indicating that the PSF cannot be reduced to a number but the whole distribution needs to be taken into account. In the follwing sections, the generation of the PSF as a 1D histogram and its usage to determine source sizes are explained.

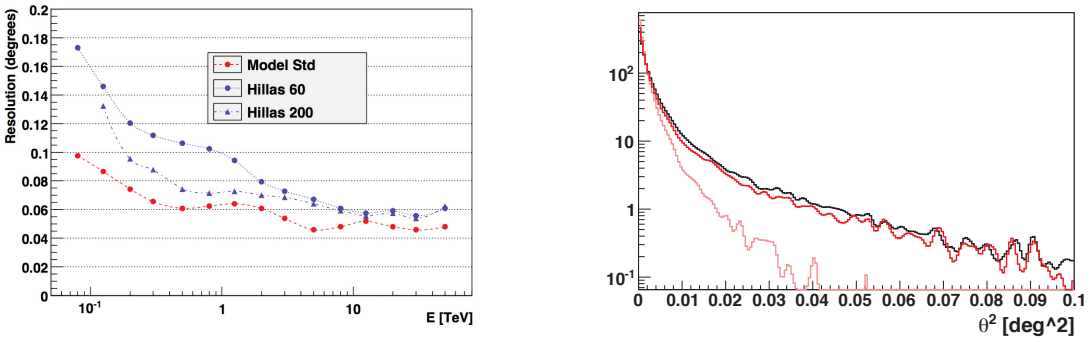

(a) (b)

Fig. 4.4.: (a) Comparison of r_{68} of different analysis types, plotted against the energy. "Hillas 60" and "Hillas 200" denote the curves obtained with Hillas analyses as described in Aharonian et al. (2006a) with cuts on the minimum number of photo-electrons of 60 and 200, respectively. Figure taken from de Naurois & Rolland (2009). (b) θ^2 plots of a normalized simulated PSF for Std (black), Faint (red) and HiRes (pink) cuts, in logarithmic scale.

4.1. PSF from MC simulations

To obtain a theoretical PSF that can be compared to data under all observation conditions, MC simulations of point-like sources are generated for all combinations of parameters listed in Table 4.1. Their spatial information is condensed and stored in *Morphology Tables*, which are then used to easily produce PSFs for a given data sample.

Table 4.1.: Settings of Monte Carlo simulations used for *Morphology Table* generation.

parameter	values
azimuth angles	0, 180
zenith angles	0, 10, 18, 26, 32, 37, 42, 46, 52, 57, 60, 63, 67, 70
efficiencies	1.0, 0.9, 0.8, 0.7, 0.6, 0.5
off-axis angles	0, 0.5, 1, 1.5, 2, 2.5, 3
photon indices	1.8, 2.0, 2.2, 2.4, 2.6, 2.8, 3.0, 3.2
number of telescopes	3, 4

Morphology Tables

Morphology Tables are five-dimensional lookup tables that contain the probability density as a function of the squared angular distance between the reconstructed and the nominal event direction, θ^2. The other four dimensions are efficiency, zenith angle, off-axis angle and photon index. The tables are generated for azimuth angles of 0° and 180° and for three and four telescopes participating in a run, respectively. They can be created for any analysis type and configuration with any cut definition - the MC simulations are analysed under these conditions and the events are rejected or labeled as gamma candidates accordingly. In order to use the simulated events efficiently, MC simulations for different photon indices are reweighted and summed up.
An array of eight histograms, each with 2000 bins in the range $[0,1]\,\mathrm{deg}^2$, is created. Each histogram corresponds to the θ^2 distribution for a photon index between 1.8 and 3.2, in steps of 0.2. Going through all events in one simulated run, each gamma candidate event is filled into each histogram by re-weighting the events of the MC according to its index. This means, e.g. in order to fill the events of a MC simulation with index $\Gamma_{MC} = 2.2$ into the table for the index $\Gamma_t = 2.8$, a weight $E^{\Gamma_t - \Gamma_{MC}} = E^{0.6}$ is given to each event. When the complete MC run is processed, the eight histograms are smoothed and normalized. The bin contents in each histogram then correspond to the probability density function (PDF) values depending on θ^2. In a loop over all bins of the eight histograms, the PDF values are filled into the proper θ^2 bins of the *Morphology Table* depending on the cosine of the zenith angle, the off-axis angle, the photon index and the muon efficiency. An example PDF is shown in Fig. 4.5.

Calculating the PSF of a data set

In order to calculate the expected PSF for a specific data set, the proper *Morphology Tables* have to be chosen and an interpolation between them is carried out to get PDF values according to the actual observation conditions in each run. The tables are selected with respect to the analysis type, the azimuth angle and all the cuts chosen in the analysis of the data set, e.g. the minimum number of photo-electrons in a shower and parameter cuts like the MSSG (see Sect. 3.3). The PSF is always calculated under the assumption

of a power law spectrum, the index Γ of which is chosen by the analyser and is usually determined in a spectrum fit. Like a *Morphology Table* histogram, the PSF histogram is initiated with 2000 bins in the range [0,1] deg^2. For each run, the *Morphology Table* for the corresponding number of participating telescopes and the rough direction (azimuth of 0° or 180°) is chosen. According to the muon efficiency μ in the run, its off-axis angle δ, mean zenith angle ζ and the chosen photon index, the PDF values stored in the *Morphology Table* are accessed. An interpolation in four dimensions is made by recursively going down to one dimension and linearly interpolating the PDF values. Schematically, the interpolation in the efficiency-dimension can be written as

$$\begin{aligned}\mathrm{GetPDF}(\theta^2,\mu,\zeta,\delta,\Gamma)|_{\mu_{true}} = &\frac{(\mu_{true}-\mu_{low})}{(\mu_{high}-\mu_{low})}\cdot\mathrm{GetPDF}(\theta^2,\mu_{high},\zeta,\delta,\Gamma)\\ &+\frac{(\mu_{high}-\mu_{true})}{(\mu_{high}-\mu_{low})}\cdot\mathrm{GetPDF}(\theta^2,\mu_{low},\zeta,\delta,\Gamma)\end{aligned}$$

where μ_{true} is the muon efficiency of the run, μ_{low} and μ_{high} are the closest simulated efficiency values below and above μ_{true}, respectively. The closer a tabulated value is to the true value, the larger its relative weight. Recursively, GetPDF means that the interpolated PDF value is calculated for the 3D table depending on (ζ, δ, Γ) and so on, until only one dimension is left which is interpolated linearly.
The interpolated PDF value is then weighted by the live time of the run and added to the corresponding bin in the θ^2 histogram. Since the H.E.S.S. PSF is assumed to be radially symmetric, this one-dimensional representation contains all the information needed.

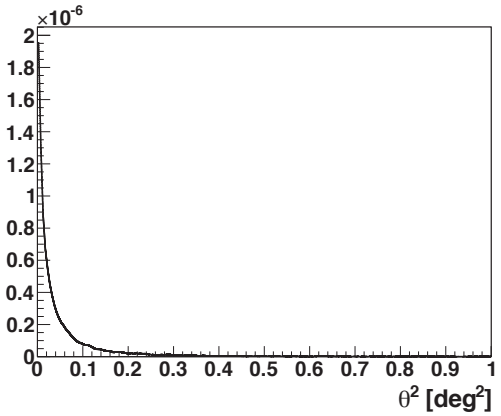

Fig. 4.5.: Example of a PDF stored in the *Morphology Tables*.

4.2. Morphology Fits

Morphology fits to the measured event distribution allow to characterize the intrinsic shape of a source. The basic principle is to compare the distribution of reconstructed event directions with a model distribution convolved with the appropriate PSF. If the distribution is expected to be radially symmetric, the comparison can be carried out using θ^2 histograms, otherwise a bidimensional fit of a sky map is necessary. In the following, the implementation of both methods in the H.E.S.S. software in binned, simultaneous ON-OFF log-likelihood fits and the morphological models used in this work are briefly

described. For a better readability, the detail that all distances in RA have to be scaled with cos(Dec) is omitted hereafter.
If the two-dimensional emission of a source is described by $\Phi(x, y)$, the expected distribution of events in a sky map is

$$\frac{d^2N}{dxdy} = \int_{-\infty}^{\infty} dx' \int_{-\infty}^{\infty} dy' \, \mathrm{PSF}(x', y') \times \Phi(x - x', y - y'), \tag{4.1}$$

with $\mathrm{PSF}(x, y) = \mathrm{PSF}(r^2 = x^2 + y^2)$. The resulting number of events in one bin of the map is

$$n_\gamma = \int_{x_0}^{x_1} dx \int_{y_0}^{y_1} dy \, \frac{d^2N}{dxdy}. \tag{4.2}$$

Assuming a radially symmetric function $\Phi(r)$ to describe the emission, the event distribution in a θ^2 histogram is

$$\frac{dN}{d\theta^2} = \int_0^{2\pi} d\phi \int_0^{\infty} dr'^2 \mathrm{PSF}(r') \times \Phi(r', \phi', \theta^2)), \tag{4.3}$$

with ϕ and r being the polar coordinates corresponding to x,y as described in Eq. 3.5. Accordingly, the expected number of γ events in the range $[\theta_1^2, \theta_2^2]$ is

$$n_\gamma = \int_{\theta_1^2}^{\theta_2^2} d\theta^2 \, \frac{dN}{d\theta^2}. \tag{4.4}$$

In both representations, the optimal model parameters can be found by minimizing the difference between expected and measured distribution. However, besides the γ emission of the source, the expected background events n_b must be modeled and compared to the measured background as well. In θ^2 fits, the background is estimated by defining OFF-regions with the *Reflected Regions* method, while a *Ring Background* is used for sky maps, see Sec. 3.4. The fit of a background level n_b and expected γ events n_γ is done simultaneously assuming Poisson statistics. If, in an ON bin i of the dataset with a live time t_{ON}, N_{ON} are measured and N_{OFF} events are found in the corresponding (accumulated) OFF bin with a live time t_{OFF}, the probability to find n_γ events from the source and n_b background events can be calculated as

$$P_i(N_{ON}, N_{OFF}|n_\gamma, n_b) = \frac{(n_\gamma + \beta n_b)^{N_{ON}}}{N_{ON}!} e^{-(n_\gamma + \beta n_b)} \, \frac{{n_b}^{N_{\mathrm{OFF}}}}{N_{\mathrm{OFF}}!} e^{-n_b}, \tag{4.5}$$

in which β replaces $t_{\mathrm{ON}}/t_{\mathrm{OFF}}$. The overall log-likelihood is formed by summing up the logarithms of P_i for all bins:

$$\log L = \sum_i \log(P_i) \tag{4.6}$$

The best estimate of n_b and of the parameters of Φ are the ones maximising the log-likelihood. Finding the maximum is accomplished by using the Levenberg-Marquardt-Algorithm (Levenberg 1944; Marquardt 1963). Originally used for least-squares minimization, it was shown to be applicable to the maximum likelihood method (Charnes et al. 1976) and stands out because of its robustness compared to other minimization algorithms. The assumed model and the parameters found in the fit can be used to characterize the morphology of the γ-ray emission of the source. In general, any spatial model can be folded with the PSF and used in a morphology fit. This work concentrates on the measurement of source sizes smaller than r_{68}, rendering complicated models indistinguishable from simple ones after the convolution with the PSF.

If the emission is not expected to show any extension, a δ function is used to model the point source:

$$\Phi(x, y) = \delta(x - x_0, y - y_0) \tag{4.7}$$

for a source positioned at (x_0, y_0). For small source sizes, a bidimensional symmetric Gaussian shape is a simple and reasonnably accurate description of the emission:

$$\Phi(x, y) = \frac{N_0}{2\pi\sigma_a^2} \exp\left[-\frac{(x - x_0)^2 + (y - y_0)^2}{2\sigma_a^2}\right] \tag{4.8}$$

The fit parameters in this case are the central position (x_0, y_0), the width of the Gaussian σ_a and the normalisation N_0. If $\theta^2 = 0$ corresponds to the correct position (x_0, y_0), the projection of this function on the θ^2 axis is

$$\Phi(\theta^2) = \frac{N_0}{2\sigma_a^2} \exp\left[-\frac{\theta^2}{2\sigma_a^2}\right], \tag{4.9}$$

leaving only the luminosity N_0 and the width σ_a as free parameters. In the following, σ_a is referred to as the *apparent size* of the source.
The morphology fit algorithm has been checked and proved to be reliable for source sizes both smaller and larger than the PSF size[1].

4.3. Containment radii

In this work, containment radii are used as a way to characterise the PSF itself and to study its parameter dependencies. The determination and use of containment radii are outlined subsequently. With the help of containment radii, the statistical error on the MC PSF is estimated. In this work, a function is fitted to the θ^2 histogram and the containment radius is defined as the containment radius of the function. The error can be calculated from the function parameters and their errors. In previous studies (e.g. Gast (2012); Stycz (2010)) three Gauss functions were successfully used to parametrise the PSF. That description and a parametrisation with a King Profile were compared, resulting in the same values of r_{68} within the statistical errors for MC simulations. In θ^2, a King profile is parametrized by

$$k(\theta^2) = \frac{1}{2\alpha^2}(1 - \frac{1}{\gamma})\left(1 + \frac{\theta^2}{2\gamma\alpha^2}\right)^{-\gamma} \tag{4.10}$$

The general formula for the radius containing a percentage c of the integral to infinity of a King Profile is

$$\mathrm{r}_c = 2\gamma\alpha^2\left[(1 - c)^{\frac{1}{1-\gamma}} - 1\right] \tag{4.11}$$

Here, a parametrisation with a King Profile is preferred, since it has less parameters, increasing the fit stability, and the containment radius and its errors can be calculated analytically.
The fits are performed using the Likelihood-Fit implementation of the MINUIT algorithm[2]. To check whether the procedure developed for this work functions correctly, so-called *pull distributions* of r_{68} were generated. As the name says, the first step is pulling

[1] A documentation of the tests can be found on internal pages:
https://hess-confluence.desy.de/confluence/display/HESS/Cen+A+Morphology+2013
[2] www.cern.ch/minuit

randomly from a theoretical distribution. A multitude of random distributions is produced and a fit is performed on each. The fitted parameters x_i should follow a Gaussian distribution centered on the true parameter μ, and the errors σ_i should reflect the scale of the deviation from the true parameter. Therefore, the pull distributions, consisting of the values

$$x_i' = \frac{x_i - \mu}{\sigma_i} \tag{4.12}$$

should follow a Gaussian distribution with a mean value of 0 and a width of 1.
An example of an MC PSF, generated for a Crab Nebula sample, and the fit of a King Profile to it are depicted in Fig. 4.6(a). The pull distributions of r_{68} of 10 000 experiments, each generated by pulling 1000 events from that PSF and fitting them with a King Profile, are depicted in Fig.4.6(b). The mean μ is chosen as the value of r_{68} resulting from a direct fit to the PSF histogram. The Gaussian function describes the distribution well (χ^2/ndf = 47.2/39) and the pull distribution behaves as expected.

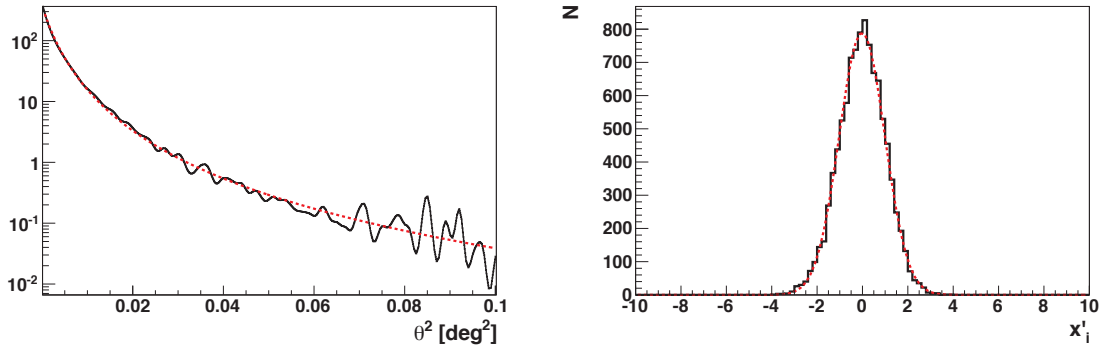

(a) (b)

Fig. 4.6.: (a) MC PSF for a sample of Crab Nebula runs (black line), fitted with a King Profile function(red dashed line). (b) Pull distribution of values x_i for r_{68}, as defined in Eq. 4.12. The black histogram is the distribution for 10 000 simulations drawn from the PSF displayed in the left panel. The red dashed line is the fit of a Gaussian, which resulted in μ = -0.02 ± 0.01, σ = 1.005 ± 0.007.

Estimation of apparent source sizes

Although a single Gaussian does not describe the PSF accurately (e.g. r_{95} is underestimated because of the "tails" of the PSF), treating r_{68} like the 68% containment radius of a Gaussian is a useful rule of thumb. For a two-dimensional Gauss function with width σ, r_{68} equals 1.515σ. This relation can be used to estimate the effect of a mismatch between true PSF and MC PSF on the source size, as described in the following.
Fitting the observed morphology of a source with a Gaussian, the width of the Gaussian corresponds to the intrinsic width convolved with the PSF width:

$$\sigma_{tot}^2 = \sigma_{src}^2 + \sigma_{PSF,true}^2 \tag{4.13}$$

The apparent source size σ_a can be estimated with the size of the PSF from MC,

$$\sigma_a^2 = \sigma_{tot}^2 - \sigma_{PSF,MC}^2 \tag{4.14}$$

If the PSF calculated from MC simulations does not equal the true PSF, the squared apparent source size

$$\sigma_a^2 = \sigma_{src}^2 + \sigma_{PSF,true}^2 - \sigma_{PSF,MC}^2 \tag{4.15}$$

is not equal to the squared intrinsic size. With $\sigma_{PSF} \sim r_{68}/1.515$, the apparent source size can be estimated for a given intrinsic source size, r_{68} and mismatch of MC and true PSF. Eq. 4.15 illustrates how difficult it is to fit source sizes close to 0° : In the quadratic subtraction, even small differences between $\sigma_{PSF,true}$ and $\sigma_{PSF,MC}$ become apparent when $\sigma_{src} = 0$. For example, for r_{68} of 0.06° (which is typical for H.E.S.S.), a mismatch of 0.002° leads to an apparent source size of 0.01° when the source is intrinsically point-like. The same mismatch is negligible when the source has an intrinsic extension of the PSF size or larger, e.g. $\sigma_a = 0.061°$ when $\sigma_{src} = 0.06°$. An illustration of the problem is shown in Fig. 4.7.

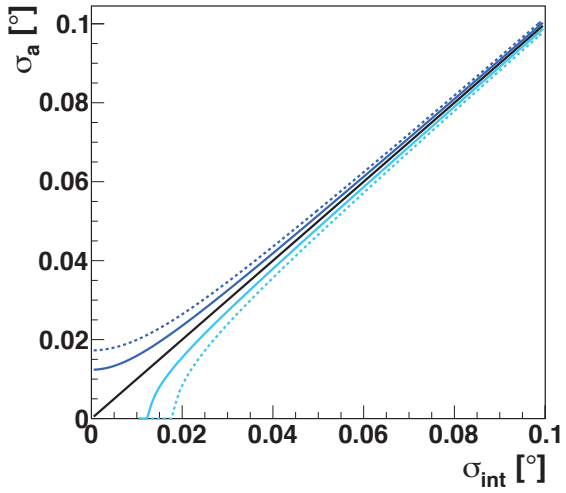

Fig. 4.7.: Apparent source size versus intrinsic source size, depending on the mismatch of true and MC PSF. The black line depicts a perfect agreement between $\sigma_{PSF,true}$ and $\sigma_{PSF,MC}$. The blue and blue dashed lines show how the apparent source size is affected if $\sigma_{PSF,true}$ and $\sigma_{PSF,MC}$ differ by 5% and 10%, respectively. $\sigma_{PSF,true}$ is set to 0.06° .

Errors on the MC PSF

In the H.E.S.S. software used with the *Model Analysis*, the MC PSF is regarded as error-free after filling the *Morphology Tables*. In reality, the event statistics of the MC simulations are far from infinite considering the required precision to fit sources with intrinsic sizes smaller than the PSF. Especially at low muon efficiencies and high zenith angles, few low-energy events are reconstructed and pass the analysis cuts. To conservatively estimate the statistical error on the MC PSF used in the following, the uncertainty on r_{68} in the *Morphology Table* bins for four-telescope observations with an off-axis angle of 0.5 and the lowest simulated muon efficiency (50%) was studied. As described in Sec. 4.1, MC simulations were analysed with Std, HiRes and Faint cuts and the events of the simulations for all spectral indices, i.e. 1.8 + 0.2·i, with i = [0...8], were accumulated in one θ^2 histogram. The number of events in the histograms for each of the three cut configurations is plotted against the zenith angle in Fig. 4.8(a). As expected, the number of events that can be reconstructed and pass the cuts decreases rapidly with zenith angle.

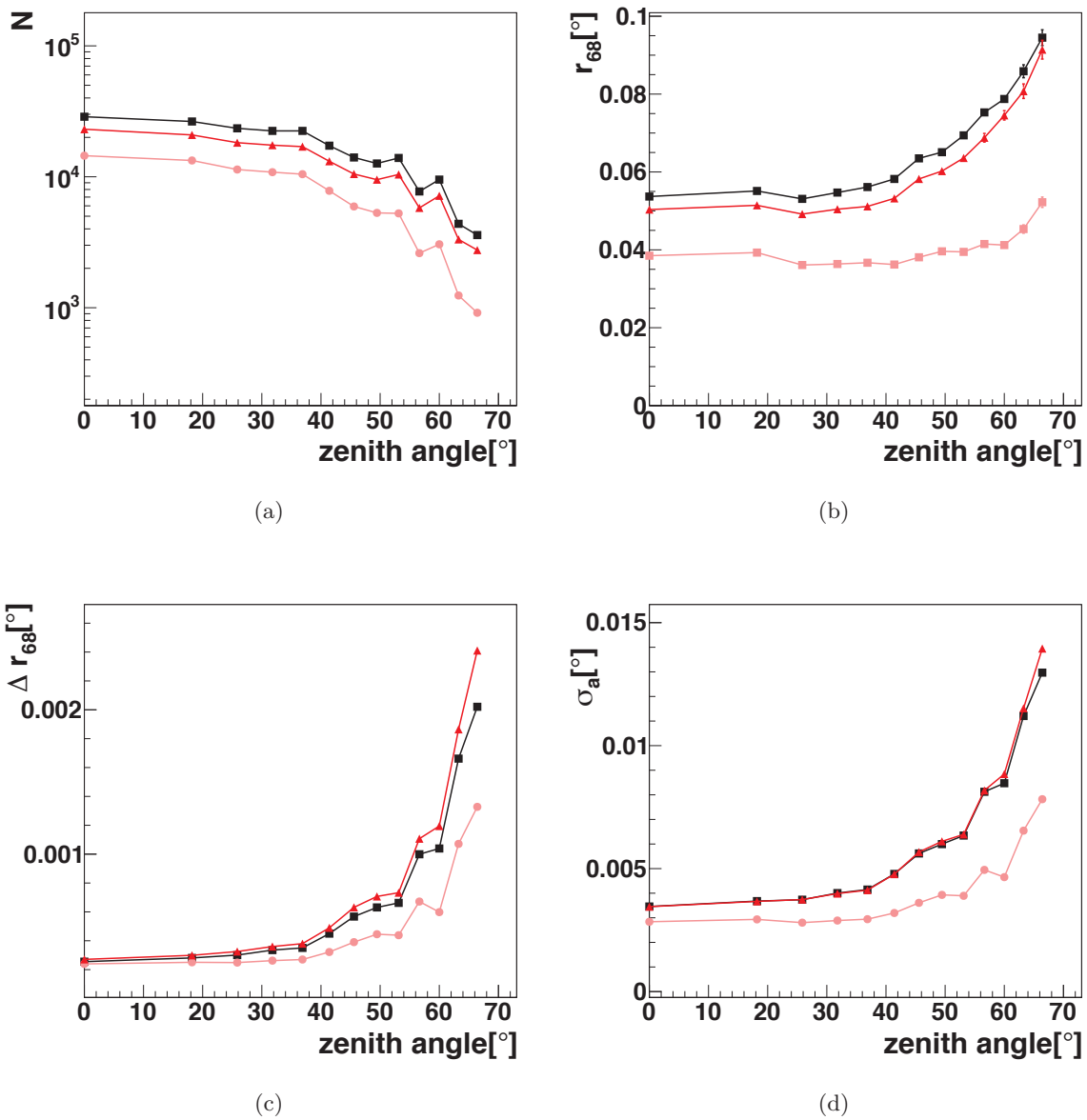

Fig. 4.8.: (a) Number of MC events passing the reconstruction and cuts at an azimuth angle of 0° , a muon efficiency of 50% and an off-axis angle of 0.5° , plotted against the zenith angle. In all plots, black squares denote Std cuts, red triangles represent Faint and pink circles HiRes cuts. (b) Corresponding r_{68} for the accumulated MC simulations and (c) Δr_{68}, the errors on r_{68}. (d) Apparent source sizes calculated from r_{68} and the error on it employing Eq. 4.16.

Only $\sim$ 50% of the events that pass Std cuts also pass HiRes cuts, while the ratio of events passing Faint cuts to events passing Std cuts is roughly 5/6. r_{68} and the statistical errors on it resulting from a fit of a King Profile are shown in Fig. 4.8(b) and Fig. 4.8(c) for the three cut configurations. Up to 60° zenith angle, which usually is the maximum for H.E.S.S. observations, the errors amount to 1 – 2% of r_{68}. If the PSF was underestimated

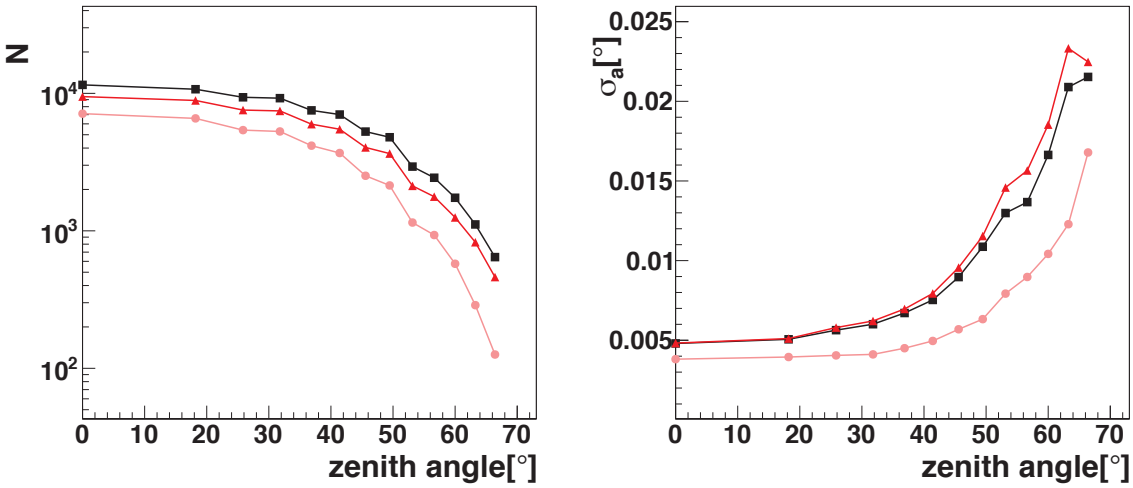

(a) (b)

Fig. 4.9.: Same as Fig. 4.8(a) and 4.8(d) for an off-axis angle of 2.0° .

by 1σ, i.e. by Δr_{68}, a point source would appear to be extended with

$$\sigma_a = \sqrt{(r_{68} + \Delta r_{68})^2 - r_{68}^2}\,/1.515. \tag{4.16}$$

using a Gaussian estimation as presented in Eq. 4.15. The relation is almost symmetric for the size of Δr_{68} at hand, meaning that an overestimation of the PSF by 1σ would yield the same result. These numbers (the statistical errors on the width of the MC PSF) can be treated as systematic errors on the size of a point-like source. For the accumulated θ^2 histograms of MC simulations with an off-axis angle of 0.5° , they are depicted in Fig. 4.8(d). The same calculation was done for higher off-axis angles. Since the camera acceptance decreases and more events are rejected due to the nominal distance cut, far less events are filled into the θ^2 histograms, see Fig. 4.9(a). Accordingly, the errors on r_{68} from the King Profile and the corresponding systematic errors on point-like sources increase, as shown in Fig. 4.9(b). An error of more than 0.01° is made for zenith angles larger than 50° . In the following sections, the statistical errors on the MC simulations are not mentioned explicitly and can be considered as the ones shown in the figures above, unless stated otherwise. For an azimuth angle of 180° and for runs with three participating telescopes, the errors are slightly larger ($\leq$10%).

4.4. Comparison with point sources

To check whether the simulated PSF reproduces the instrument response correctly, a comparison with real point sources is performed. Two types of sources are guaranteed to be point-like for H.E.S.S.: Binary systems and variable AGN. The size of the emission region of binaries is constrained by the physical process producing VHE γ-rays, see Sec. 2.1. Four VHE γ-ray binaries have been detected by H.E.S.S. so far: LS 5039, HESS J0632+057, PSR B1259-63/LS 2883, and HESS J1018-589 A (associated with the binary 1FGL J1018.6–5856), but for the latter, an underlying extended emission is seen (not associated with the binary system, see H.E.S.S. Collaboration et al. (2012)).

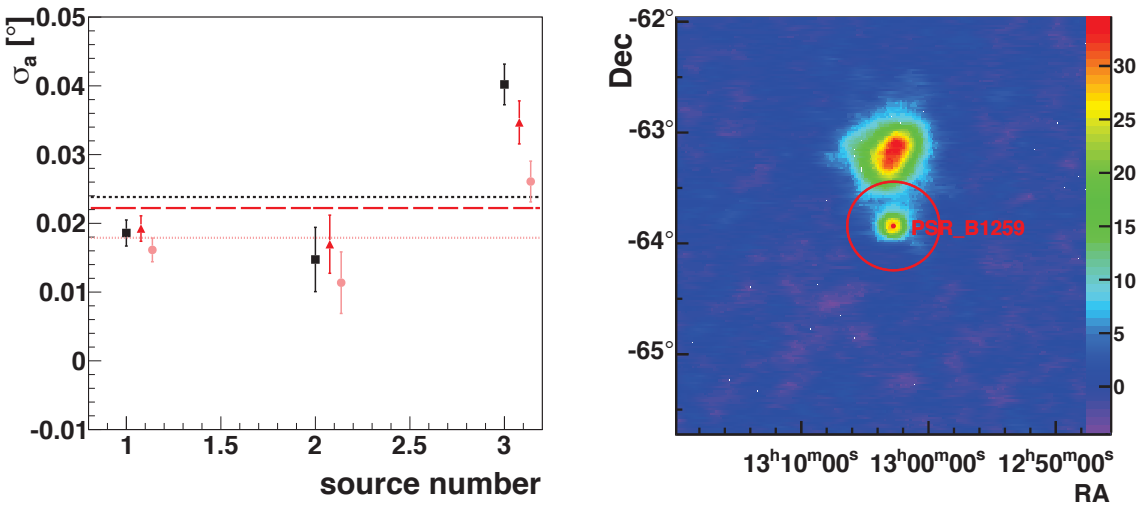

(a) (b)

Fig. 4.10.: (a) Fitted source sizes for the three binaries (from left to right) LS 5039, HESS J0632+057 and PSR B1259-63 obtained with Std cuts (black squares), Faint cuts (red triangles) and HiRes cuts (pink circles). Fits of constants for all three cut configurations are shown as dashed lines in the corresponding colours. (b) Significance map of PSR B1259-63 and the neighbouring source J1303-631. The red circle has a radius of 0.5° .

For variable sources, a safe criterion for the maximum size is given by causality: When an emission zone emerges, its size cannot be larger than the distance that light can travel in the time of its development. For relativistic processes, a possible Doppler boost of the emission zone has to be taken into account, since it leads to an apparent extension. If the bulk of the emission moves with a Lorentz factor $\Gamma = \sqrt{\frac{1}{1-\beta^2}}$ with $\beta = v/c$, at an angle θ to the line of sight, the resulting Doppler factor is

$$\delta = [\Gamma(1 - \beta \cos\theta)]^{-1} . \tag{4.17}$$

Given a variability time scale t_{var}, the radius R of the boosted emission zone cannot be larger than

$$R_{max} = c t_{var} \delta/(z+1) \tag{4.18}$$

for a source at a redshift z. Depending on the distance to the source, the observable angular size can be much smaller than the H.E.S.S. PSF. Therefore, variable AGN are good candidates for true point sources: Located at large distances, some of them display a high flux variability.
The three binary systems LS 5039, HESS J0632+057 and PSR B1259-63 as well as a selection of bright AGN were analysed and their morphology was compared with the MC PSF. For this purpose, the size of the ON region was chosen to be 0.4° , which is a trade-off between maximum extension of the θ^2 histogram and the number of uncorrelated OFF-regions. On the one hand, a large analysis region is necessary because the tails of the PSF contribute to events beyond 0.3° in observations with large zenith angles (see Fig. 4.3). On the other hand, more OFF regions are preferable to achieve higher background statistics, which makes the fit of source sizes stable against fluctuations. For a region size of 0.4° , two independent OFF regions can be used. All known H.E.S.S. sources and so-called "hot spots" were excluded from the analyses, their locations and extensions being taken from

the H.E.S.S. Galactic Plane Scan Catalogue (H.E.S.S. Collaboration, in prep.). First, 2D skymaps were generated with the Ring Background method (see Sec. 3.4 and the source position was fitted, assuming a point source model. Taking the fitted position as the center, the data was re-analysed and finely binned θ^2 histograms were produced. Additionally, analyses for the extraction of spectra were performed with an ON region size of $0.01\,\mathrm{deg}^2$ for Std cuts. This size of the analysis region was chosen to optimise the ratio of γ-ray events to hadronic events. Furthermore, it allows for a large number of OFF regions, leading to a stable fit of the background spectrum and thereby to a solid fit of the source spectrum. The spectra were fitted with a simple power-law model (see Eq. 3.8, and the fitted spectral index Γ was used to generate the corresponding MC PSF. The θ^2 histograms were fitted with a symmetric Gaussian model, i.e. an exponential function as described by Eq. 4.9, convolved with that PSF. A one-dimensional fit is preferred because of less parameters and the higher bin-wise statistics in both ON and OFF histograms, leading to smoother Likelihood functions and thus to more stable fit results.
The apparent sizes of LS 5039, HESS J0632+57 and PSR B1259-63 for Std, Faint and HiRes cuts are shown in Fig. 4.10(a). All fitted sources are significantly extended. A fit of a constant to the three data points gives $c = (2.4 \pm 0.1)\cdot 10^{-2}\,\mathrm{deg}$ with $\chi^2/\mathrm{ndf} = 42.8/2$ for a Std analysis, $c = (1.8 \pm 0.1)\cdot 10^{-2}\,\mathrm{deg}$ with $\chi^2/\mathrm{ndf} = 10.8/2$ for a HiRes analysis and $c = (2.2 \pm 0.1)\cdot 10^{-2}\,\mathrm{deg}$ with $\chi^2/\mathrm{ndf} = 20.3/2$ for Faint cuts. Since HESS J0632+057 is very faint, which is reflected in the comparatively large statistical errors in Fig. 4.10(a), its apparent size may be a statistical fluctuation. LS 5039 is located near the PWN HESS J1825-137, hence the unexpected extensions may be attributed to leaking events from the neighbouring source or problems in the background estimation because of the large exclusion region. However, this effect is probably minor: The distance between the sources is 1.27° and the flux contamination with events of HESS J1825-137 is less than 5% in periods of high γ-ray emission of the binary system (Mariaud 2014). PSR B1259-63 is very close to the PWN HESS J1303-631 (see Fig. 4.10(b)), therefore a contamination with the PWN events is probable.
The apparent sizes of the selected AGN are shown in Fig. 4.11. For the widths found with Std cuts, the fit of a constant yields $(2.29 \pm 0.02)\cdot 10^{-2}\,\mathrm{deg}$ with $\chi^2/\mathrm{ndf} = 95.3/7$, HiRes and Faint cuts result in $(1.93 \pm 0.02)\cdot 10^{-2}\,\mathrm{deg}$ and $(1.65 \pm 0.03)\cdot 10^{-2}\,\mathrm{deg}$, respectively, and similar χ^2/ndf values. For close-by AGN like M87, a resolvable size is possible, and also for distant objects possible explanations for extended non-variable emission exist, see Chapter 6. However, the sources at hand have roughly the same apparent size independent of their distance, which strongly suggests that the MC PSF is underestimated by a systematic error of that size. The differences between the different cuts and the high χ^2/ndf values also indicate that there are unknown sources of systematic errors.
The maximum ratio of extended emission can be constrained to a few percent in extreme outbursts of VHE emission, so-called flares. In addition to displaying a point source, flare data are exceptional because of the extremely high flux levels of the sources, providing high statistics of γ-like events. The most prominent example, a flare of PKS 2155−304, will be discussed in the following. Since the three runs measuring the highest flux were taken one after the other, the data set displays exceptionally stable system properties compared to the usual, long-term data sets, where the interplay between different effects is more complicated. The comparison of MC PSF and true PSF of the H.E.S.S. experiment will be done under the assumption that the flare morphology is indeed point-like.

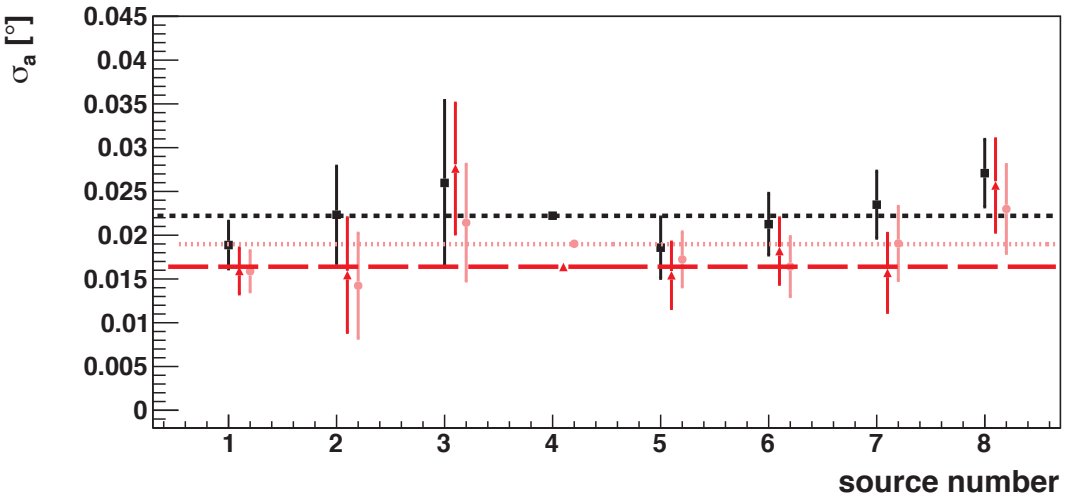

Fig. 4.11.: Fitted apparent source sizes of various AGN, numbered according to the list below. The mean apparent size is estimated by the fit of a constant, which is depicted as the black dashed line for Std cuts, a red dashed line for Faint and a pink dashed line for HiRes cuts.

1 - M 87	3 - PKS 0548−322	5 - 1ES 0229+200	7 - 1ES 0347−121
2 - PKS 1514−241	4 - PKS 2155−304	6 - 1ES 1101−232	8 - PKS 0447−439

The flare of PKS 2155−304 in 2006

As described in Aharonian et al. (2007b), the high-frequency-peaked BL Lac PKS 2155−304 at redshift z = 0.117 displayed an extreme γ-ray outburst on July 28, 2006. Its flux varied on time scales of minutes and reached peak values of more than 15 times the Crab nebula flux over 200 GeV, see Fig. 4.12(a). Given the variability time scale and applying the causality argument, the size of the emission region is limited to $R{\cdot}\delta^{-1} \leq 4.65 \cdot 10^{12}$cm (Aharonian et al. 2007b). To explain the fast rise time of the flare, a very high Doppler factor of ≥ 100 is needed (Aharonian et al. 2007b). Even with this factor, the radius of the emission region corresponds to an angular size of only $\theta \leq 2 \cdot 10^{-11}$ deg, which is many orders of magnitude smaller than the H.E.S.S. PSF and can therefore only be seen as a point-like source.

The dataset used here, consisting of the three runs with the highest flux, is the one described in Aharonian et al. (2007b). In the 88 minutes covered by these runs, the measured flux from PKS 2155−304 was $15.44 \pm 0.03 \cdot 10^{-10}\mathrm{m}^{-2}\mathrm{s}^{-1}$ above an energy threshold of 0.2 TeV, while the quiescent flux level of the source is about $(4.23 \pm 0.09) \cdot 10^{-11}\mathrm{m}^{-2}\mathrm{s}^{-1}$. Hence, the flux of a possibly extended non-variant component can be at most 3% of the flare flux, and the ratio of signal to background events is 10180/759 in the complete analysis region.

The data of PKS 2155−304 were taken with four telescopes, pointing towards the target with an off-axis angle of 0.5°. The mean zenith angle of the runs is 13° and the muon efficiency of the array was 53% at that time. The position of the source is fitted to RA = 329° 43' 8.4", Dec = -30° 13' 34.9", which is 0.0021° from the nominal source position and therefore well within the nominal pointing precision of 0.008°. Fitting the source size to the θ^2 histogram at the new position, an extension of $\sigma_a = 2.06^{+0.06}_{-0.07} \cdot 10^{-2}$ deg is found in a Std analysis. As illustrated in Fig.4.14(b), the apparent source size is larger than $1.86{\cdot}10^{-2}$ deg at a 3σ confidence level, hence incompatible with a point-like source. Also

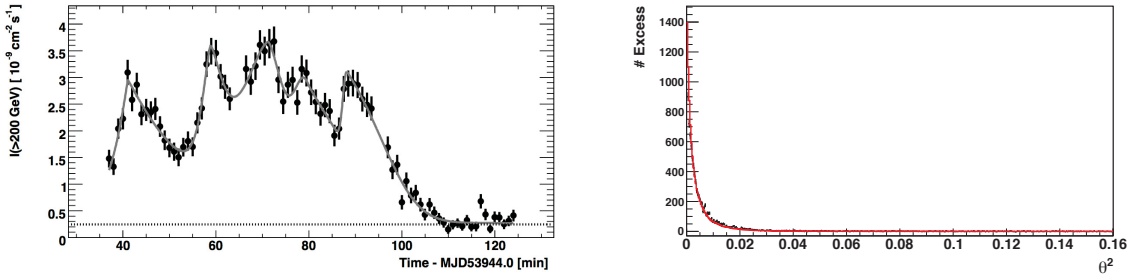

(a) (b)

Fig. 4.12.: (a) Time evolution of the integral flux above 200 GeV observed from PKS 2155−304 in the dataset described in the text. Each bin corresponds to a time interval of one minute. The horizontal line represents the Crab Nebula flux > 200 GeV as described in Aharonian et al. (2006a). Figure taken from Aharonian et al. (2007b). (b) θ^2 distribution of the same dataset (black) and corresponding MC PSF (red) with Std cuts.

in the HiRes and Faint analyses, the apparent size remains $1.79^{+0.07}_{-0.08} \cdot 10^{-2}$ deg and (1.44± 0009)·10^{-2} deg, respectively. To illustrate how small the deviations are that introduce such source sizes, the θ^2 excess distribution and the scaled (not fitted) PSF are shown in Fig. 4.12(b). A zoom of the same plot and a log-scale representation are shown in Fig. 4.13(a) and Fig. 4.13(b).

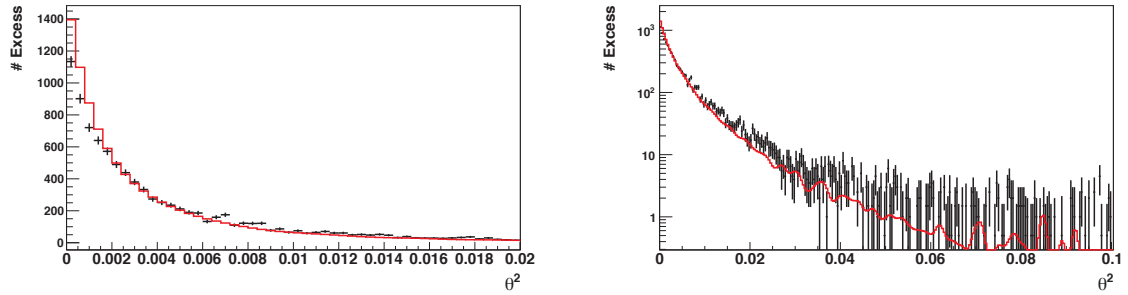

(a) (b)

Fig. 4.13.: (a) Zoom into Fig. 4.12(b) to visualize the mismatch between data (black) and PSF (red). (b) Zoom into Fig. 4.12(b) in logarithmic scale.

To check whether this deviation from the expected point-like behaviour stems from a possible extension of the non-variable component, a simple simulation was developed. A source with a Gaussian width of σ_s was simulated and convolved with the MC PSF of the PKS flare data set. To simulate the overall source shape, this extended component was added at a 3% flux level to the PSF, which represents the variable point-like component. The resulting θ^2 histogram was fitted with a King Profile and the apparent source size was calculated as described in Sec. 4.1. The apparent source sizes for different σ_s and PSFs obtained with Std, HiRes and Faint analyses are listed in Table 4.2, all of them are below 0.01° . Quadratically subtracting this conservative maximum value from the fitted source size of the flare for Std cuts, an extension of more than 0.018° remains. The HiRes and Faint analyses display an even smaller effect of the simulated extended component.

Clearly, the existence of a non-variable component cannot explain why the fitted size contradicts the expected point-like nature. The apparent extension of the PKS 2155−304 flare can be used as an estimate for the mismatch between the MC PSF and the true angular resolution of the H.E.S.S. experiment.

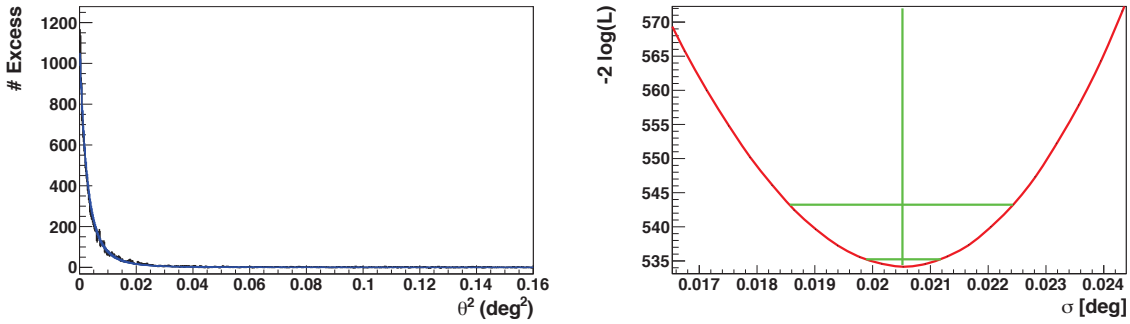

(a) (b)

Fig. 4.14.: (a) Fit of a Gaussian, convolved with the PSF, to the flare data obtained with Std cuts. Data are shown in black, the fitted function in blue. (b) Likelihood profile of the fit parameter σ_a around its best-fit position for the flare data. The red line represents the negative Log-Likelihood values plotted versus σ_a. The best-fitting source size is marked by the vertical green line, the lower and upper horizontal green lines represent 1σ and 3σ error bars, respectively.

Table 4.2.: Simulated apparent source size of the PKS 2155−304 flare assuming that a non-variable component with a Gaussian width σ_s spoils the signal. All values are given in 10^{-2} deg. The errors depend exclusively on the chosen number of simulated events shown in Fig. 4.8(d)

σ_s	1.0	3.0	10.0	20.0	40.0
σ_a, Std	0.14	0.37	0.85	0.98	0.78
σ_a, HiRes	0.14	0.40	0.82	0.78	0.70
σ_a, Faint	0.12	0.38	0.86	0.88	0.82

4.5. Systematic errors in the PSF calculation

As concluded in the last section, there is a non-negligible mismatch between the data and the MC PSF, indicating that the description of the detector response in the MC simulations is incorrect or insufficient. Systematic errors can occur on all stages of MC PSF generation, starting with the simulation of showers and their interactions in the atmosphere in the KASKADE code and ending with the improper reconstruction of γ-ray shower properties.
In this section, a systematic study is conducted to check whether the known dependencies of the PSF are described adequately in the simulations and how much some approximations contribute to the mismatch. All effects are studied on two levels: Expected systematic errors according to theoretical predictions from the MC, and systematic errors derived from the behaviour of observational data. For this examination, the PKS 2155−304 flare data set is not enough because it covers only a tiny part of the parameter space under investigation. Instead, the most-observed and brightest sources without a known significant extension were chosen, namely the complete H.E.S.S. samples on PKS 2155−304 and the Crab Nebula. Although these objects might well be intrinsically extended on a level visible for H.E.S.S. , they are eligible for this study since it is not the absolute value of the fitted size that is of importance here, but its relative behaviour under different conditions. The intrinsic source size cannot depend on the observation and analysis conditions in any way except for an energy dependence. Energy-dependent morphologies are a common phenomenon in γ-ray astronomy, see Chapter 2. Therefore, the tests of different energy thresholds presented in the following are conducted on the PKS 2155−304 flare data exclusively, since the flare must be a point source at all energies.

Energy threshold

Unlike in spectral fits (see Sec. 3.5), no energy threshold is introduced in morphology fits, albeit the correct reconstruction of event properties at the lowest energies is questionable. Since the highest event statistics are found close to the lowest reconstructed energies, a mismatch of MC and data in that energy range may have a strong influence on the apparent source size. As an example, the reconstructed energy distributions of events from the PKS 2155−304 flare runs and of matching Monte Carlo events are shown in Fig. 4.15. To model the conditions of the PKS 2155−304 flare data described in Sec. 4.4, MC simulations for an observation of a source with a spectral index of 3.4 with four telescopes with 50% muon efficiency, at an off-axis angle of 0.5° and zenith angles of 0° and 18° were chosen for comparison. The MC distribution is scaled to the flare data distribution. As can be seen in Fig. 4.15(a), the PKS 2155−304 data contain events with lower energies than can be reconstructed in the MC. Although the lowest energy simulated for this run was 30 GeV, the reconstructed energies of the MC events are all larger than ∼150 GeV and the peak of their distribution is shifted to higher energies compared to the flare data.
To check whether the mismatch between MC and data PSF is caused by the low-energy events, threshold energies were introduced. As described in Sec. 3.5, a threshold is best calculated dynamically depending on the effective areas $\mathcal{A}$ for the respective observation conditions C. However, a threshold at the energy corresponding to 15% of the maximum acceptance barely cuts into the energy distribution. Instead, the minimum allowed energies were chosen to be E_t and $2E_t$, with

$$E_t = \max\left(E^{-2} \times \mathcal{A}(E, C)\right). \tag{4.19}$$

This energy indicates the position of the peak of the expected energy distribution for a

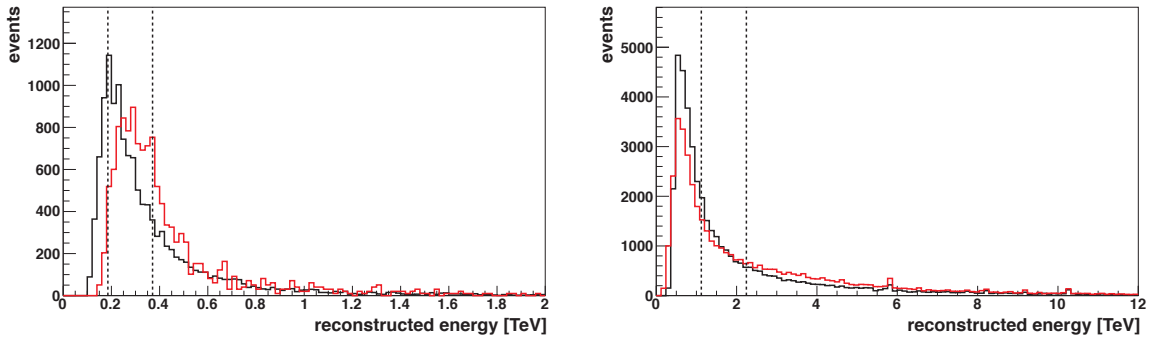

(a) (b)

Fig. 4.15.: (a) Distribution of reconstructed energies of the PKS 2155−304 flare events (black) and of a matching MC simulation (red). The vertical lines indicate E_t and $2E_t$. (b) Energy distribution of 10 runs on Mkn 421 at zenith angle of 60° to 63° (black) and of matching MC simulations (red). The energy threshold positions, denoted by the vertical lines, are shifted to higher energies accordingly. Note the different scale of the axes.

power-law spectrum with $\Gamma = 2$. Since most sources display softer indices, this threshold is expected to reject all events below the peaks of the reconstructed energy distributions. The remaining events are then reconstructed in an energy range displaying a rather flat effective area. However, in the MC in Fig. 4.15(a), the peak is at higher energies than E_t although an index of 3.4 was simulated. Therefore, also a threshold position of $2E_t$ was investigated. To illustrate how the threshold positions increase with zenith angle, the energy distribution of 10 runs on the AGN Mkn 421 at zenith angles above 60° is shown in 4.15(b).

In combination with the energy threshold, the HiRes cut configuration reduces the event statistics of the flare data set too drastically to allow for significant extension measurements. In the Faint cut configuration, the required minimum number of photo-electrons has an effect similar to the introduction of an energy threshold. Therefore, the energy threshold study was performed only for the Std cut configuration.

To generate MC PSFs for events above the respective thresholds, *Morphology Tables* with additional cuts on minimum energies of E_t and $2E_t$ were produced. After the analysis and the standard event selection, the threshold was calculated anew for each MC run from the tabulated effective areas. Only events with sufficiently high energies were filled into the (energy-weighted) histograms that constitute the PDF. In the data analysis, the thresholds were calculated from the effective areas corresponding to the mean observation conditions of each run of a data set. E_t and $2E_t$ were used for event rejection similarly to other cuts, except that the cut value changed for each run individually. The results of the fit of a Gaussian, convolved with the newly generated MC PSFs, to the PKS 2155−304 flare data, analysed including corresponding event rejection, are presented in Table 4.3. Although r_{68} of the MC PSF decreases, the energy thresholds do not change the apparent source size significantly. The difference between the angular distributions of MC and data seems to be constant throughout the PKS 2155−304 flare spectrum.

Table 4.3.: r_{68} of the MC PSF and σ_a of the flare of PKS 2155−304 for different energy thresholds.

threshold energy	-	E_t	2 E_t
r_{68} of MC [10^{-2} deg]	6.37 ± 0.04	6.31 ±0.04	5.86 ± 0.04
σ_a [10^{-2} deg]	$2.06^{+0.06}_{-0.07}$	$2.15^{+0.06}_{-0.06}$	$1.93^{+0.08}_{-0.08}$

Number of telescopes

The reconstruction of γ-rays is more precise the more stereoscopic information is available for each event. Therefore, observations with all four telescopes are expected to display a smaller PSF size in terms of r_{68} than the observations with three telescopes, see Fig.4.16(a). The difference is largest for high zenith angles and reduces at small zenith angles and small spectral indices, hower, it does not vanish. Although a minimum multiplicity of two telescopes is required for each event independent of the number of participating telescopes in a run, the mean multiplicity is higher in four-telescope observations. A comparison of PKS 2155−304 and Crab Nebula data taken with three or four telescopes was conducted. The overall number of used runs on PKS 2155−304 is 967, 758 of them four-telescope runs. For the Crab Nebula, 171 (51 of them taken with three telescopes) were analysed. No significant difference between the three- and four-telescope data was found, except for the sizes resulting from fits with the Std configuration, see Table 4.4. When taking into consideration the statistical errors on the MC simulations and the differences in observation parameters between the three- and four-telescope sample, a systematic effect of that size can be easily explained, even by the missing azimuth interpolation that will be presented next. Because of the better quality of the reconstruction and the smaller statistical errors on the MC simulations, only data taken with four telescopes are used in the subsequent studies.

Table 4.4.: Apparent source sizes of the Crab and PKS 2155−304 for analyses with three and four telescopes and for different analysis cuts.

source	cuts	σ_a, 3 telescopes [10^{-2} deg]	σ_a, 4 telescopes [10^{-2} deg]
Crab	Std	2.05 ± 0.07	2.30 ± 0.04
	HiRes	1.88 ± 0.08	1.97 ± 0.04
	Faint	1.98 ± 0.07	2.15 ± 0.04
PKS	Std	2.12 ± 0.10	2.26 ± 0.02
	HiRes	2.11 ± 0.12	1.91 ± 0.02
	Faint	1.91 ± 0.13	1.65 ± 0.03

Azimuth angle

MC simulations are generated for two azimuth angles, 0° (North) and 180° (South), which are close to the expected minimum and maximum of the azimuth dependence of the PSF. Unlike for most other observation parameters, no interpolation between the tables is applied for this quantity. The difference between MC simulations at the two azimuth angles depends on the index of the observed source (i.e. the energy of the γ-ray events that initiated the shower) and the zenith angle of the observation, see Fig. 4.16(b). For

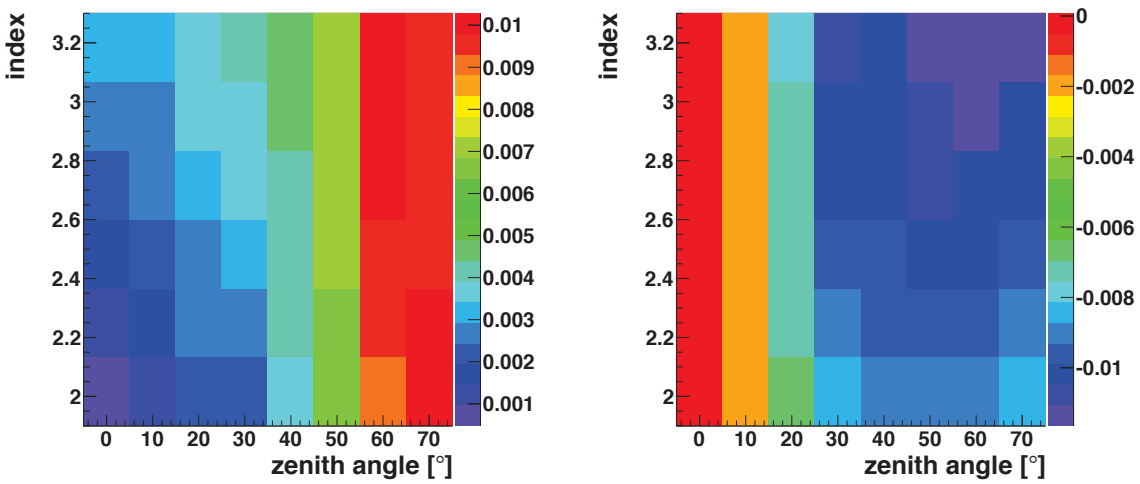

(a) (b)

Fig. 4.16.: (a) Difference between the *Morphology Tables* for 3-telescope observations and 4-telescope observations, for an off-axis angle of 0.5° and an azimuth angle of 0° (North), with a simulated muon efficiency of 100%. The colour scale visualizes the difference in r_{68}, $\Delta r_{68} = r_{68,3tels} - r_{68,4tels}$ in degrees. (b) Difference in *Morphology Tables* for observations pointed towards azimuth = 0° (North) and azimuth = 180° (South) for an off-axis angle of 0.5° and a muon efficiency of 100%. The colour scale for $\Delta r_{68} = r_{68,North} - r_{68,South}$ is given in degrees.

high zenith angles, r_{68} can differ by more than 0.01° between North and South, inducing a non-negligible error on the calculation of source sizes. To visualize it, the expected apparent source size of a virtual source with a spectral index of 2.6 and an intrinsic size of 0.02° , moving from North to East to South at a fixed zenith angle of 45° is shown in Fig. 4.17. The apparent size increases with increasing azimuth angles between 0° and 90° , becomes much lower than the intrinsic source size at 90° and inreases again towards an azimuth angle of 180° , where the original value is reached. The increase and decrease are neither linear nor symmetric due to the quadratic nature of the problem. The numbers in Fig. 4.17 were calculated with Eq. 4.15, assuming $r_{68} = 0.07°$, which is typical for Std cuts. In the following, it is assumed that the PSF behaves symmetrically in the East and in the West.

The effect on real data was studied with the PKS 2155−304 and Crab Nebula four-telescope samples. PKS 2155−304 is observed in the South direction, therefore the apparent source size is expected to decrease with increasing distance from 180° , while the Crab Nebula is a source of the northern sky, hence the opposite behaviour with distance from 0° is expected. Both samples were divided into bins of ≥ 30 runs according to the distance to azimuth = 0° and azimuth = 180° , respectively. The East or West orientation of the runs was not considered, i.e. the absolute values Δazimuth were used. The PKS 2155−304 sample covers a broad range in azimuth and consists of more than 750 runs, allowing for eight bins, whereas the azimuth range of the Crab Nebula as observed from the H.E.S.S. site is only ± 45° . The apparent source sizes for Std, HiRes and Faint cuts plotted against the mean azimuth angle are shown in Fig. 4.18.

A test for correlation of σ_a with the azimuth angle was conducted by comparing fits of a

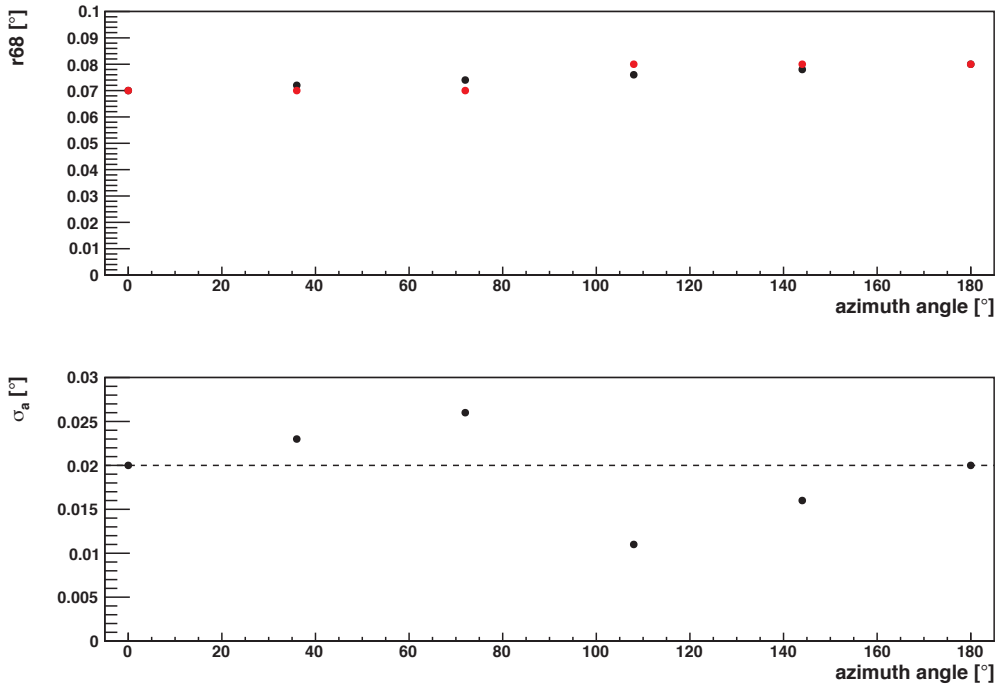

Fig. 4.17.: Expected behaviour of the apparent source size with azimuth. The apparent source sizes are given for a virtual source with an intrinsic extension of 0.02° and a spectral index of 2.6, that is always seen at 46° zenith angle for different azimuth angles.

constant and a first-order polynomial with an F-test. F-tests are statistical tests based on the Fischer-distribution (or F-distribution), which is a continuous probability distribution. They are used to compare fits with nested models, i.e. if model 1 is a nested model of model 2, the F-ratio is defined as

$$F = \frac{(\chi_1^2 - \chi_2^2)/(\mathrm{ndf}_1 - \mathrm{ndf}_2)}{\chi_2^2/\mathrm{ndf}_2} \tag{4.20}$$

where $\mathrm{ndf}_{1,2}$ and $\chi^2_{1,2}$ are the respective numbers of degrees of freedom and χ^2 values of the fits. The F-distribution has two parameters: $\Delta\mathrm{ndf} = \mathrm{ndf}_1$ - ndf_2 and ndf_2. The integral over the F-distribution for these parameters above the value F gives the probability p_1 that model 1 can be rejected. F-tests are preferred to χ^2-tests when an unknown systematic surpasses the statistical errors of the data, which clearly manifests itself in the high χ^2/ndf values in the studies at hand, see Table 4.5. The results of all fits and of the F-tests are summarized in the same table.
While no significant azimuth dependence is found for the Crab data due to the smaller azimuth range, the polynomial is preferred by more that 2σ to describe the PKS 2155−304 data. Remarkably, using the parametrisation by the polynomial, the difference in apparent source size between azimuth = 0° and azimuth = 70° matches what is expected from the *Morphology Tables* and employing Eq. 4.15 for an intrinsic source size of 0.02° . Also in the fits to the Crab data analysed with Std cuts, the slope implies that the apparent source size at 40° azimuth angle is 0.0036° larger than at azimuth = 0° , matching the prediction in Fig. 4.16(b) very well.
In summary, the measurements suggest that the tendencies can be attributed to the missing azimuth interpolation. The good agreement of the measured azimuth dependence of

source sizes with what is expected from a linear interpolation between North and South shows that the difference in PSF size between az = 0° and az = 180° is described correctly in the MC simulations.

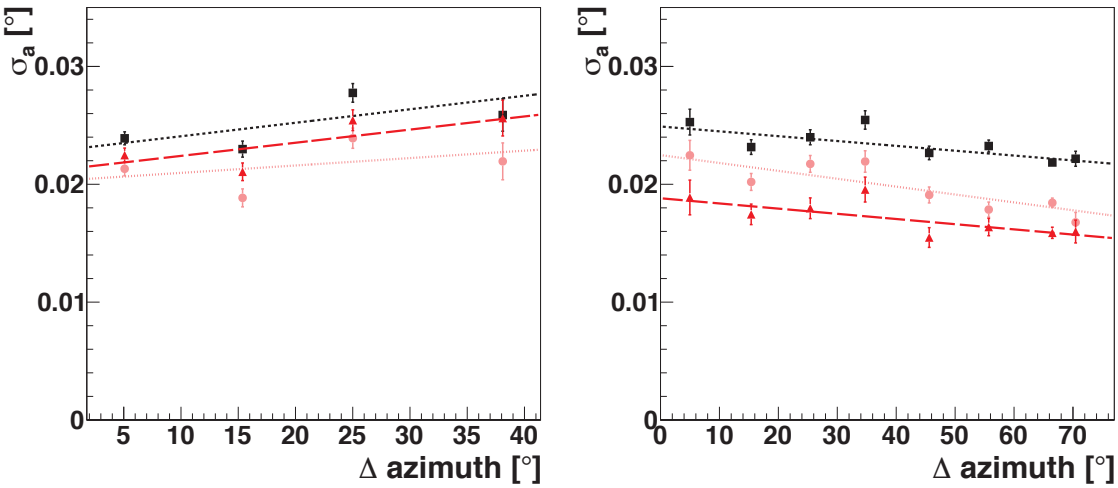

Fig. 4.18.: Apparent sizes of the Crab Nebula (left) and PKS 2155−304 (right) depending on the azimuth angle. Black filled squares indicate the fitted source sizes of different samples, binned according to the distance of their mean azimuth angle to an azimuth of 0° for the Crab Nebula and to 180° for PKS 2155−304. The black dashed line shows the fit of a first order polynomial to the data. For the same binning, the source sizes from analyses with HiRes (pink circles) and Faint (red triangles) cuts and the respective linear fits are shown.

Table 4.5.: Results of the fits of a constant and a polynomial to the apparent source sizes of the Crab Nebula and PKS 2155−304 depending on azimuth angle. The graphs are depicted in Fig. 4.18. c_1 is the best-fit value of a constant, χ^2_1/ndf_1 is the according sum of squared residuals divided by the number of degrees of freedom. c_2 is the constant of the linear fit, while a is its slope, given in degrees per degree of azimuth angle. p is $1 - p_1$, where p_1 is the probability of the polynomial being preferred resulting from the F-Test.

source	cuts	c_1 [10^{-2}deg]	χ^2_1/ndf_1	c_2 [10^{-2}deg]	a [10^{-5}]	χ^2_2/ndf_2	p
Crab	Std	2.46 ± 0.04	24.0/3	2.29 ± 0.06	11 ± 4	14.0/2	0.354
	HiRes	2.12 ± 0.04	19.8/3	2.03 ± 0.07	6 ± 4	17.3/2	0.646
	Faint	2.29 ± 0.04	18.1/3	2.13 ± 0.07	11 ± 4	10.2/2	0.340
PKS	Std	2.29 ± 0.02	30.5/7	2.49 ± 0.05	-4 ± 1	12.9/6	0.029
	HiRes	1.92 ± 0.02	46.7/7	2.25 ± 0.06	-6 ± 1	13.3/6	0.008
	Faint	1.67 ± 0.03	18.1/7	1.88 ± 0.07	-4 ± 1	7.9/6	0.033

Zenith angle

During one observation run, typically lasting 28 minutes, sources can move up to 7° in zenith. This maximum change is only reached by sources that culminate in zenith; the lower a source culminates, the smaller the difference in zenith angle during a run. On the other hand, the slope of r_{68} increases rapidly for high zenith angles. To keep the linear interpolation valid, the zenith angle bins of the MC simulations are chosen as arccos(1 − 0.05·i), with i ranging from 0 to 14. Judging by the slope of r_{68} between MC simulations, deviations from linearity between the zenith angle bins would be very small and are not expected to be visible in the data, see Fig. 4.19(a).

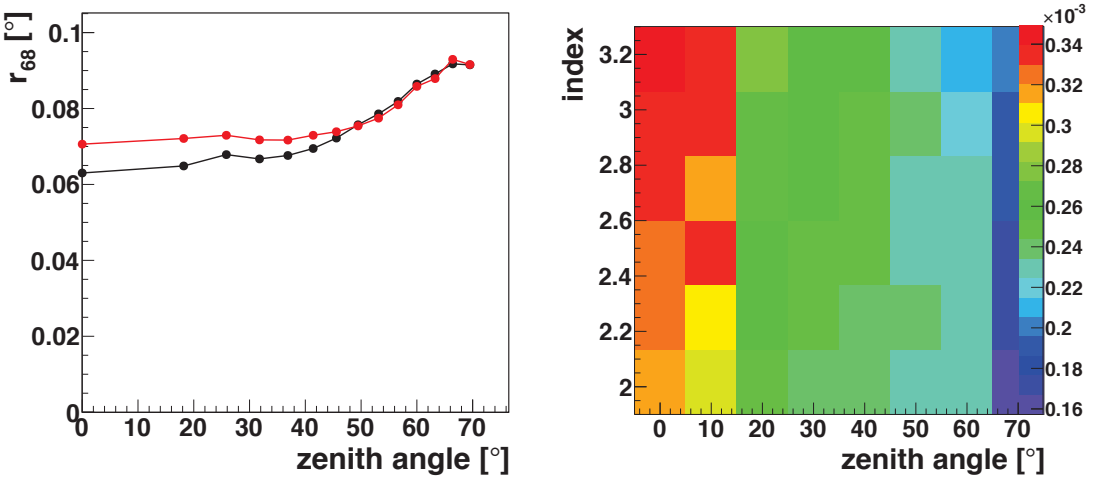

(a) (b)

Fig. 4.19.: (a) r_{68} of MC versus zenith angle for a spectral index of 2.2 (black) and 3.2 (red). The filled circles indicate the positions of the MC simulations, the lines symbolize the linear interpolation between them. (b) Error on r_{68} made by miscalculating the muon efficiency by 1%, depending on the spectral index of the source and the zenith angle of the observation. The colour scale is given in degrees. The plot was produced from MC simulations for an azimuth angle of 180° and an off-axis angle of 0.5° .

Since the zenith angle dependence of a source translates almost directly into its dependence on azimuth angle, the missing azimuth interpolation is expected to be the dominant effect. Only the different directions of the wobble offsets modify the azimuth-zenith correlation. Nevertheless, to check whether the apparent source size behaves as expected, the sample of 4-telescope runs of PKS 2155−304 was divided into zenith angle bins, each containing roughly 30 runs. PKS 2155−304 was observed at zenith angles ranging from 0° to 60° , i.e. the runs cover almost the whole zenith angle range of H.E.S.S. The resulting apparent source sizes for the 20 bins are shown in Fig. 4.20, and the fit parameters of a constant and a straight line are listed in Table 4.6. Applying F-tests, a line is only preferred by more than 2σ in the case of HiRes cuts, but Std and Faint cuts show the same tendency. Based on the linear azimuth interpolation introduced above, a source with a size of 0.03° is expected to appear 0.004° smaller in the last zenith bin, which is at an azimuth angle of ∼70° . The size and direction of the slope are in good agreement with that expectation, indicating that the dependence of the PSF on the zenith angle is reflected well in the MC simulations. This statement is supported by the fact that the apparent source size of the

Crab Nebula depends on the zenith angle in just the opposite way for Std and Faint cuts, see Fig.4.20. However, no significant dependences are found in the Crab Nebula data.

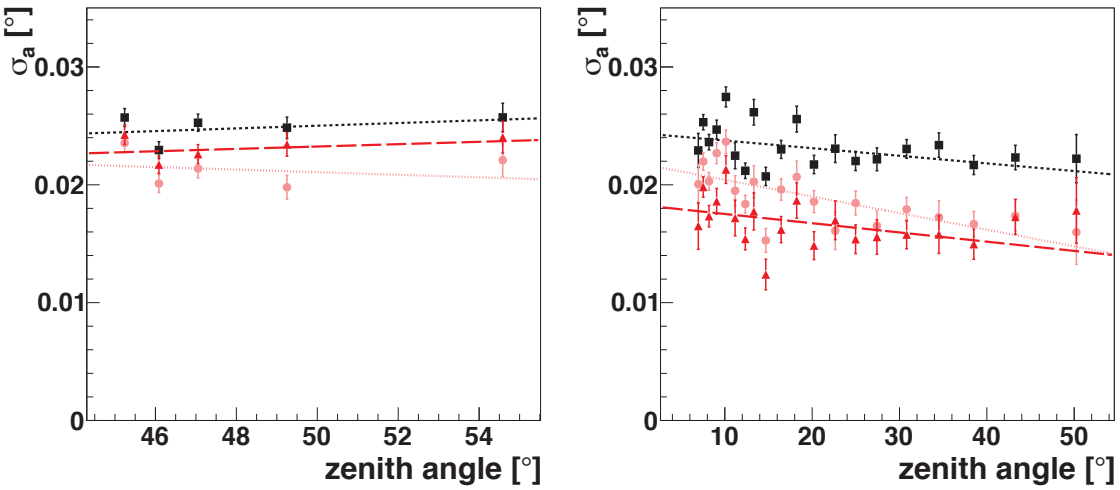

Fig. 4.20.: Dependence of the apparent source size of the Crab Nebula (left) and PKS 2155−304 (right) on the zenith angle. Black filled squares indicate the source sizes resulting form Std analyses, binned according to the mean zenith angle of a run. The black dashed line displays the best-fitting first-order polynomial. Apparent source sizes for HiRes and Faint cuts are shown as pink circles and red triangles, respectively. The fits of polynomials are shown as pink and red dashed lines, accordingly.

Table 4.6.: Test of the zenith dependence of apparent source sizes of the Crab Nebula and PKS 2155−304. Listed are the fit results of a constant and a polynomial to the graphs depicted in Fig. 4.20. χ^2_1/ndf_1 results from the fit of a constant, c_1, while χ^2_2/ndf_2 results from the fit of a polynomial with the constant c_2 and the slope a as parameters. a is given in degrees per degree of zenith angle. p is the probability of the constant being a sufficient description, calculated with the F-Test.

source	cuts	c_1 [10^{-2}deg]	χ^2_1/ndf_1	c_2 [10^{-2}deg]	a [10^{-5}]	χ^2_2/ndf_2	p
Crab	Std	2.47 ± 0.04	9.4/4	1.93 ± 0.70	11 ± 14	8.7/3	0.663
	HiRes	2.14 ± 0.04	12.7/4	2.65 ± 0.74	-11 ± 16	12.2/3	0.754
	Faint	2.30 ± 0.04	6.3/4	1.82 ± 0.7	10 ± 15	5.88/3	0.673
PKS	Std	2.320 ± 0.02	83.4/19	2.44 ± 0.04	-6 ± 2	70.5/18	0.086
	HiRes	1.93 ± 0.02	91.0/19	2.18 ± 0.05	-14 ± 2	51.9/18	0.002
	Faint	1.69 ±0.03	54.0/19	1.83±0.05	-8 ± 3	45.0/18	0.074

Muon efficiency

The calculation of the optical efficiency bears a systematic error and a statistical error, both described in Sec. 3.2. The systematic error amounts to up to 5%, while the statistical errors are 2–3%, depending on the calibration period. Varying the muon efficiency by 5% gives errors on r_{68} of up to 0.0017°, see Fig.4.19(b). For a point-like source, this corresponds to an apparent source size of 0.01° if $r_{68} = 0.07^\circ$. Also the correctness of the dependence of the MC PSF on the muon efficiency was checked. The data of PKS 2155−304 and of the Crab Nebula were split into bins of ≤ 30 runs according to the mean muon efficiency. For each bin, the apparent source size was fitted for Std, HiRes and Faint cuts, see Fig. 4.21. The graphs of the apparent sources sizes versus muon efficiency were fitted with a constant and with a first-order polynomial. The fit results and the p-values of the F-test are presented in Table 4.7. Neither of the descriptions is significantly preferred in most cases, only the fit to the PKS 2155−304 data analysed with Std cuts displays a 2σ evidence for a dependence on muon efficiency. However, the slopes in the Crab Nebula data are opposed to the slopes in the PKS 2155−304 data. Again, this might be explained by the missing azimuth interpolation, since the efficiency of the runs seems to be correlated with their mean azimuth angle, see the lower row in Fig. 4.21. Apparently, in the initial phase of the four-telescope H.E.S.S. array, when the optical efficiencies were still comparatively high, more observations of both PKS 2155−304 and the Crab Nebula were conducted at high zenith angles. This also implies larger values for Δazimuth. In addition, only in the early years observations at high offset angles were performed. The possible implications of this relation are described in the next subsection.

Table 4.7.: Results of the fits of a constant and a polynomial to the graphs of apparent source sizes depending on the muon efficiency. The graphs and the best-fit polynomial are depicted in Fig. 4.21. The naming scheme is the same as in Table 4.5, except for the slope a of the polynomial being given in degrees per percent of muon efficiency.

source	setting	c_1 [10^{-2}deg]	χ^2_1/ndf_1	c_2 [10^{-2}deg]	a [10^{-2}deg]	χ^2_2/ndf_2	p
Crab	Std	2.43 ± 0.04	17.9/4	1.86 ± 0.37	1.0 ± 0.7	15.5/3	0.543
	HiRes	2.11 ± 0.04	14.0/4	1.32 ± 0.40	1.4 ± 0.7	10.1/3	0.357
	Faint	2.25 ± 0.04	24.7/4	0.71 ± 0.39	2.8 ± 0.7	9.1/3	0.109
PKS	Std	2.38 ± 0.02	132.4/11	4.76 ± 0.30	-4.5 ± 0.6	68.9/10	0.013
	HiRes	1.99 ± 0.02	55.9/11	3.36 ± 0.35	-2.6 ± 0.6	40.1/10	0.075
	Faint	1.73 ± 0.03	38.1/11	2.38 ± 0.38	-1.2 ± 0.7	35.3/10	0.391

Off-axis angle

Up to an off-axis angle of 1.5°, the PSF is expected to be constant. Beyond, r_{68} increases (see Fig. 4.3) and the mean of the reconstructed events shifts away from the source position in the camera due to the asymmetric camera acceptance. In practice, observations of point-like sources are carried out at offset angles of 0.5° – 1°. Only in the beginning phase of H.E.S.S., when the capabilities and the performance of the instrument were tested, a few runs on the Crab Nebula with wobble offsets of up to 2° were performed. When splitting the Crab Nebula sample according to the mean pointing offset of the run, these runs form the last bin, see Fig. 4.22(a). Although the total observation time in that bin is almost

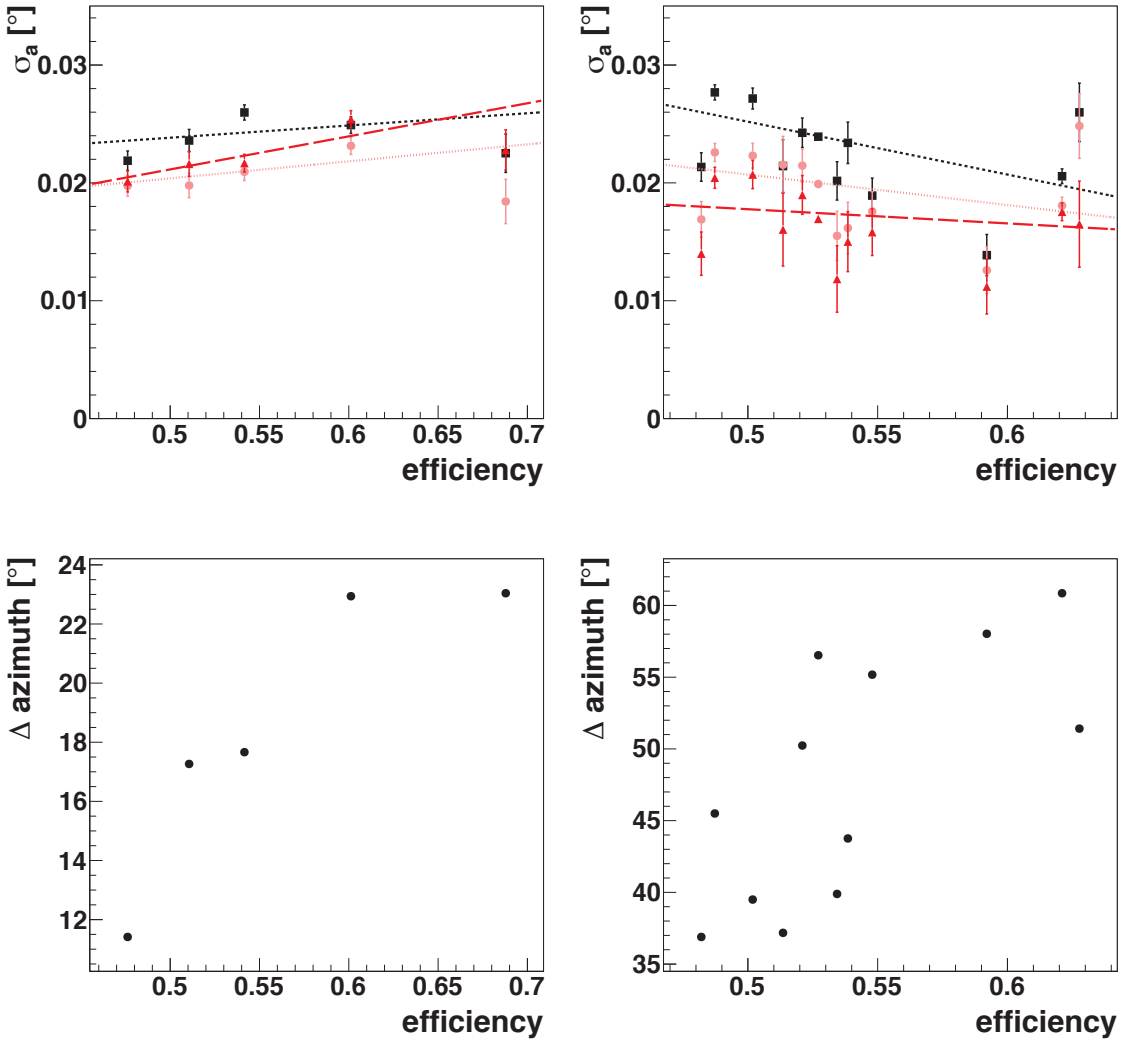

Fig. 4.21.: *Upper row*: Dependence of the apparent source sizes of the Crab Nebula (left) and PKS 2155−304 (right) on the mean muon efficiency of the run. The binned data are depicted as filled black squares for Std cuts, red triangles for Faint cuts and pink circles for HiRes cuts. The best-fit polynomials are indicated by the dashed lines in the respective colours. *Lower row*: Muon efficiency of Crab Nebula (left) and PKS 2155−304 (right) runs versus their mean azimuth angle, binned as in the graphs above.

9 hours, the event statistics are low since the acceptance diminishes rapidly towards the camera edges. To check whether the apparent source size varies with off-axis angle, a constant and a first-order polynomial were fitted to each of the graphs for Std, HiRes and Faint cuts. The fit results and corresponding F-test results are shown in Table 4.8. No significant dependence is found, but there is a tendency to fit smaller source sizes with increasing off-axis angle, especially when analysing with HiRes cuts. However, the large statistical errors on the data and on the MC PSF at large off-axis angles (see Sec. 4.3) should be kept in mind.

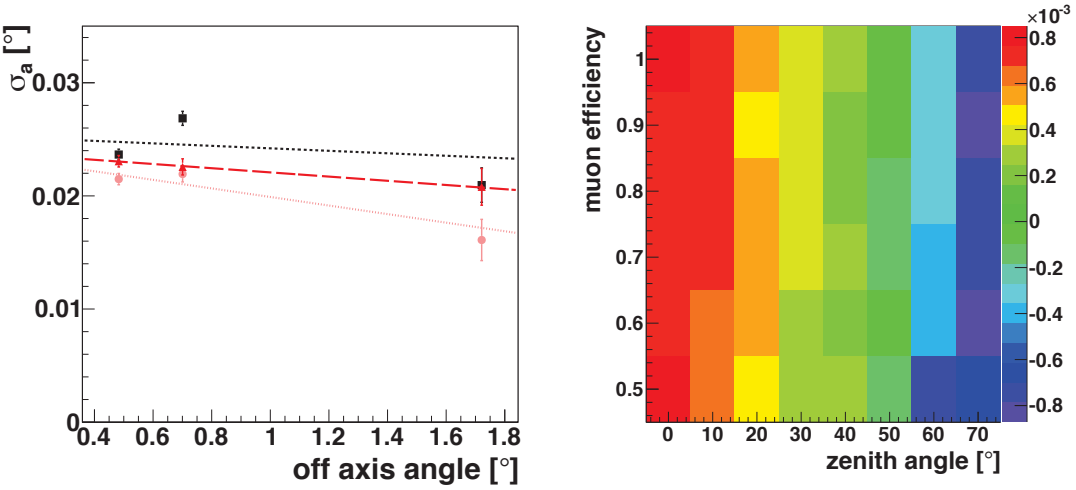

(a) (b)

Fig. 4.22.: (a) Dependence of the apparent source size of the Crab Nebula on the off-axis angle of the run. Black filled circles depict the fitted source sizes for Crab Nebula data, binned according to the mean off-axis angle of the run, while the red line represents the best-fit first order polynomial. (b) Expected errors on r_{68} made by miscalculating the spectral index by 0.1, calculated from MC simulations for an off-axis angle of 0.5° and an azimuth angle of 0° . The colour scale indicates the slope $\Delta r_{68} = (r_{68,\Gamma=3.2} - r_{68,\Gamma=2.2})/10$ in degrees per 0.1 index unit.

Table 4.8.: Results of the fits of a constant and a polynomial to the apparent source size of the Crab Nebula, depending on the off-axis angle (see Fig. 4.22(a)). Except for the slope of the polynomial a, which is given in degrees per degree of off-axis angle, the naming scheme is the same as in the previous tables.

source	setting	c_1 [10^{-2}deg]	χ^2_1/ndf$_1$	c_2 [10^{-2}]	a [10^{-5}]	χ^2_2/ndf$_2$	p
Crab	Std	2.46 ± 0.04	22.9/2	2.53 ± 0.09	-0.1 ± 0.1	22.2/1	0.884
	HiRes	2.14 ± 0.04	9.1/2	2.37 ± 0.10	-0.4 ± 0.1	2.6/1	0.357
	Faint	2.28 ± 0.040	1.9/2	2.39 ± 0.09	-0.2 ± 0.1	0.01/1	0.054

Spectral index

The error on the spectral index consists of the statistical error determined in spectral fits and the systematic error, which was estimated to be 0.1 in Aharonian et al. (2006a). Both lead to systematic errors in the PSF produced from MC. If the total error on the spectral index used for PSF calculation is of the order of the systematic error, the effect on r_{68} is negligible in most cases, see Fig. 4.22(b). For example, for a source with an intrinsic size of 0.03° and assuming a typical value of $r_{68} = 0.07°$, the apparent source size would increase to 0.0308° in the maximal cases, where $\Delta r_{68} = 8 \cdot 10^{-4}$. On the other hand, if the source was point-like, it would appear to be extended by 0.007° when using a spectral index wrong by 0.1.

To test the behaviour of the apparent source size depending on the spectral index, the 8 AGN listed in Fig. 4.11 and the two binaries LS 5039 and HESS J0632 were used. To extract the spectra, analyses with Std cuts using a θ^2 cut of 0.01 deg^2 were performed, in contrast to the morphological analyses in which the θ^2 cut was set to 0.16 deg^2. The spectral indices were fitted assuming a power law model. In Fig. 4.23, the apparent source sizes are plotted against the spectral index. The graphs were fitted with a constant and a polynomial of first order, which were compared in an F-test, see Table 4.9. A significant increase in the source size with spectral index was found for Std and HiRes cuts and a similar tendency is seen for Faint cuts.

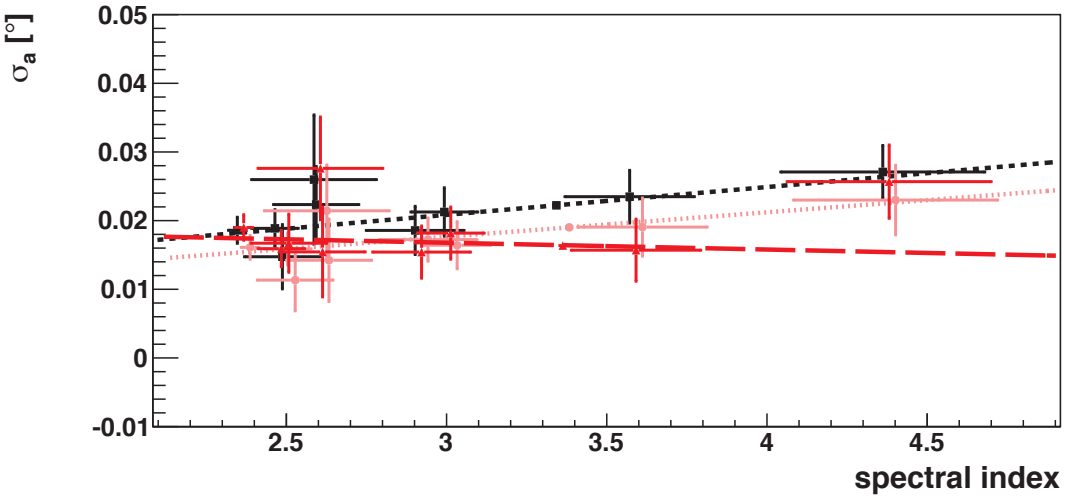

Fig. 4.23.: Apparent source sizes of the eight AGN listed in Fig. 4.11 and the two binaries LS 5039 and HESS J0632 plotted versus their spectral index. Black squares represent the source sizes with Std cuts, red triangles and pink circles represent Faint and HiRes cuts, respectively. The dashed lines in the corresponding colors display the best-fitting first order polynomials for each graph.

Table 4.9.: Test of the dependence of the apparent source size of eight AGN and two binary sources on the spectral index. The results of the fits of a constant and a polynomial to the graphs depicted in Fig. 4.23 are listed. Except for the slope of the polynomial a, which is given in degrees per unit of spectal index, the naming scheme is the same as in the previous tables.

setting	c_1 [10^{-2}deg]	χ^2_1/ndf$_1$	c_2 [10^{-2}]	a [10^{-2}]	χ^2_2/ndf$_2$	p
Std	2.04±0.1	10.7/9	0.6±0.5	0.5±0.2	3.7/8	0.005
HiRes	1.65±0.1	4.3/9	0.9±0.6	0.3±0.2	2.5/8	0.045
Faint	1.83±0.1	8.0/9	1.2±0.6	0.02±0.2	6.8/8	0.28

Pointing

Although the radial pointing precision described in Sec. 3.2 is far below r_{68} of the PSF, the contribution of mispointing to the determination of positions and sizes smaller than r_{68} is not negligible for sources with high statistics. The pointing corrections described in Sec. 3.2 are calculated period by period, leaving some uncertainty because of effects that change night by night, or even run by run (wind, temperature etc.). In addition, the refractional properties of the atmosphere vary. The way that optical light (the stars seen in the CCDs) is subject to refraction is different from the change of reconstructed direction of a γ-ray, especially at high zenith angles - this is taken into account in the calibration, but the accuracy of the correction has not been checked.

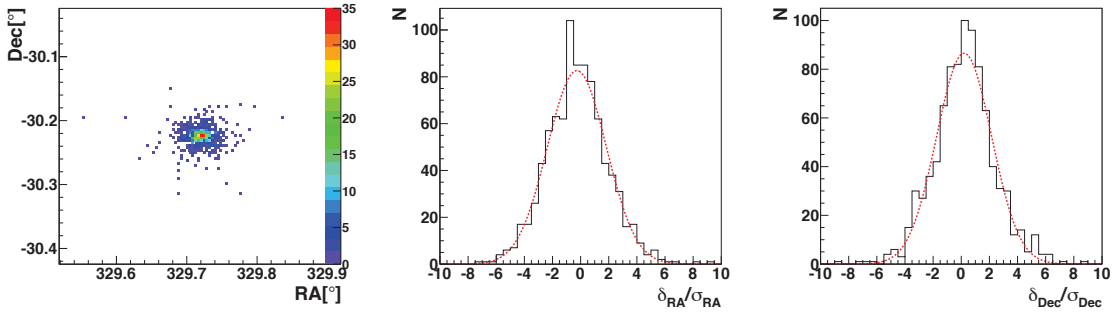

(a) (b) (c)

Fig. 4.24.: (a) Fit positions of single PKS 2155−304 runs. The color scale indicates the number of runs in one bin. (b) Corresponding distribution of $\delta_{RA} = x_i$ - x_0, divided by the statistical fit errors σ_{RA}. The black histogram displays the data, the dashed red line is the fit of a Gaussian. (c) Same as (b), but for Dec values.

Here, the absolute pointing precision is not considered, but the relative pointing deviations around the best-fit position. A jitter of the pointing position would smear the reconstructed directions, which could lead to an apparent extension of sources. Assuming that the jitter is normally distributed, the size σ_{syst} of the systematic error on the observation position per run can be determined experimentally.
For this investigation, the complete samples of PKS 2155−304 and the Crab Nebula were analysed run by run and the source position was fitted for each run separately using a point source model. The point source model contains the minimum number of parameters necessary for this investigation, reducing the number of failed fits. For PKS 2155−304, the positions (RA $= x_i \pm \sigma_{stat,x,i}$, Dec $= y_i \pm \sigma_{stat,y,i}$) of 701 runs can be determined in this way, and 120 run positions can be fitted for the Crab Nebula. The distribution of the fitted positions for PKS 2155−304 is displayed in Fig.4.24.
From the fit of the complete sample as one, the overall best-fit position for each source is determined to be at RA $= x_0$ and Dec $= y_0$. If the fits work correctly, the *pull distributions* of RA and Dec values

$$x'_i = \frac{(x_i - x_0)\cos(y_0)}{\sigma_{x,i}}, y'_i = \frac{y_i - y_0}{\sigma_{y,i}}, \tag{4.21}$$

with $\sigma_{x,i} = \sqrt{\sigma^2_{stat,x,i} + \sigma^2_{syst,x,i}}$ and equivalently for $\sigma_{y,i}$, should follow Gaussian distributions with a mean of 0 and a width of 1. Consequently, assuming radial symmetry and a correct choice of the central position, the distribution of the position misplacement

$\Psi^2 = (x_i - x_0)^2 * \cos^2(y_0) + (y_i - y_0)^2$,

$$\Psi'_i = \frac{\Psi_i^2}{\sigma^2_{stat,\Psi,i} + \sigma^2_{syst,\Psi,i}} \tag{4.22}$$

should follow an exponential function $\sim \exp(-\Psi'/2)$. Under the assumption that the systematic pointing error is the same in all runs, $\sigma^2_{syst,\Psi,i} = \sigma^2_{syst,\Psi}$, a scan of it can be performed to find the systematic error fulfilling that condition. In practice, this means the distribution from Eq. 4.22 is produced for a range of values of $\sigma^2_{syst,\Psi}$ and each time fitted with an exponential function $n_0 \exp(-x/(2a))$. The value of $\sigma^2_{syst,\Psi}$ that leads to $a = 1$ is a good estimate for the systematic error. To illustrate the procedure, the distribution of $\Psi^2/\sigma^2_{stat,\Psi,i}$ for PKS 2155−304 is displayed in Fig 4.25(a). A fit of an exponential function $n_0 \exp(-x/(2a))$ yiels $a = 1.624$. In Fig. 4.25(b), the values of a versus $\sigma^2_{syst,\Psi}$ are shown. The value of $\sigma^2_{syst,\Psi}$ corresponding to $a = 1$ is $(0.78 \pm 0.03) \cdot 10^{-2}$ deg. For the Crab Nebula, the Gaussian width of the jitter was found to be $(0.62 \pm 0.05) \cdot 10^{-2}$ deg with the same procedure as described above, see Fig. 4.25(d). These values mark the systematic smearing of the measured spatial event distribution through the run-by-run pointing jitter. The effect is not negligible, but small in comparison to the apparent source sizes in Sec. 4.4. The position fits of PKS 2155−304 seem generally worse than the ones for the Crab Nebula, which is caused by the variability of the source, i.e. in some runs there are too few excess events for a good position fit, visible as the outliers in Fig. 4.25(b). The Crab Nebula, on the other hand, is a constant source in our current understanding.

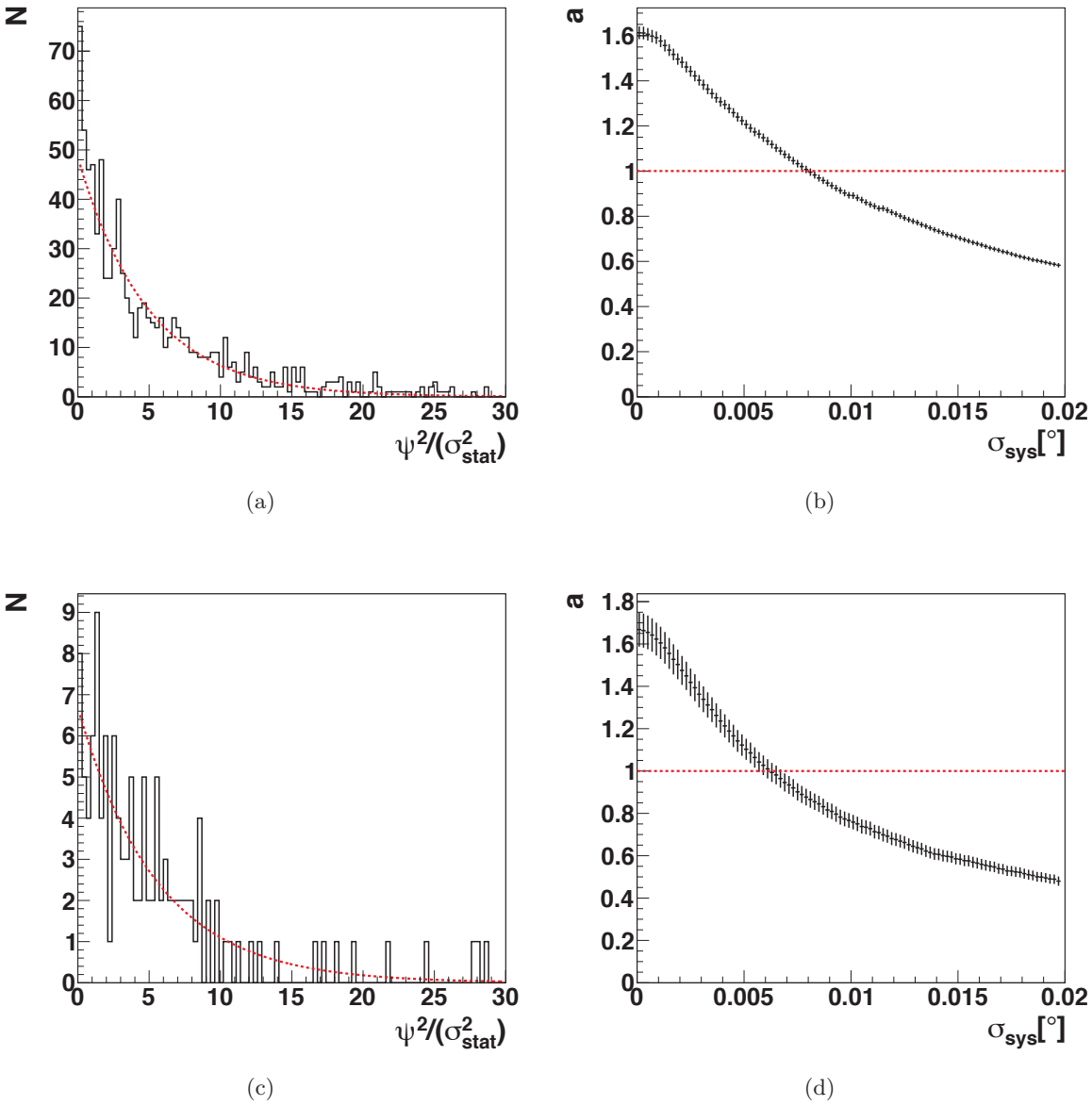

Fig. 4.25.: (a) and (c): Distributions of Ψ^2/σ_{stat} (black histogram), Ψ being the position misplacement, and fit with an exponential function $n_0 \exp(-x/(2a))$ (dashed red curve) for PKS 2155−304 and the Crab Nebula. (b) and (d): The black crosses mark the fitted values of a when a systematic error of σ_{syst} is introduced in the histograms on the left . The dahed red line denotes $a = 1$.

Broken pixels

When camera pixels are broken, shower information is missing. The number of photo-electrons in the pixel is seemingly zero and may affect the evaluation of even more pixels because of the image cleaning. In an analysis with Hillas ellipses, a missing pixel can easily corrupt the complete reconstruction of a shower. The Model++ reconstruction is expected to be more robust. Since it employs a likelihood fit, the photo-electron number in the broken pixel is not treated as a measurement of zero, but the pixel is simply not included in the *Goodness*, *MSSG*, *Background Goodness* and *NSB Likelihood* calculations. Whether one pixel is missing or not, the same shower template can be fitted to the image. Moreover, each shower is fitted in all camera images simultaneously, thus the choice of the template is comparatively stable. However, when too many pixels are broken, the reconstruction will not be able to compensate and the PSF is expected to degrade. Especially when a whole drawer in a central part of the camera is broken, the loss of information might be severe although only 1/60 of the camera is affected. In MC simulations, the effect is rather small. Example MCs with broken pixel fractions of 10% and 20% in all four telescopes were produced for different spectral indices at a zenith angle of 0° and without an offset from the source position. In the simulations, half of the broken pixels were arranged in batches of 4 (TODO: which is a typical RING SAMPLER?! error) while the other half were randomly distributed. TODO: MISSING COMPLETE DRAWERS WAS NOT SIMULATED. r_{68} was calculated from the θ^2 distributions of these simulated runs, the results for Std, HiRes and Faint cuts are listed in Tables 4.10 – 4.12. Significant increases in r_{68} with percentage of broken pixels are found for low spectral indices for Std and HiRes cuts, while Faint cuts seem not affected. The largest difference between r_{68} for 0% broken pixels and 20% broken pixels is found to be $(0.22 \pm 0.05)\cdot 10^{-2}$ deg for the MC with index 2.0 analysed with Std cuts, which corresponds to an apparent source size of a point-like source of 0.011° . As is done in the *Morphology Tables*, the events for all simulated indices were accumulated into one histogram. Except for the histogram generated for HiRes cuts, which is $(0.09 \pm 0.03)\cdot 10^{-2}$ deg broader at 20% broken pixels than without broken pixels, no significant increase is found. With observational data, such a comparison is difficult to accomplish. In most runs, the percentage of broken pixels varies from telescope to telescope. In the standard run selection, all runs with less than 15% of broken pixels in at least three of the telescopes pass. Reducing the allowed percentage of broken pixels in that selection to 5% yields 16 runs in the Crab Nebula sample and 72 runs from the PKS 2155−304 sample. In the complete Crab Nebula sample of H.E.S.S. , only three runs were found that have less than 5% of broken pixels in all four telescopes, and their mean off-axis angle is 1.8° . With the same strict selection, only one run was found for PKS 2155−304. Similarly, among the H.E.S.S. observations of PKS 2155−304 only four runs with more than 10% of broken pixels in all four telescopes exist, and 36 with more than 10% of broken pixels in at least three telescopes. For the Crab Nebula, there are six runs and 29 runs with more than 10% of broken pixels in all four or at least three telescopes, respectively. The resulting apparent source sizes for all of the samples are summarized in Table 4.13. No consistent trend is found, so no conclusive statement can be made about how broken pixels affect the PSF. Likely, other factors have a dominant impact on the PSF.

Other possible effects

Although the studies performed are extensive, there is a multitude of other possible influences on the PSF. The mismatch between the MC PSF and the data distributions may stem from early stages of the MC production. First of all, the development of showers

in the atmosphere, simulated with KASKADE, might not display the actual statistical spread of shower shapes or positions. Since the KASKADE code has been in use for more than 20 years in a variety of experiments, the description of particle interactions in the atmosphere is assumed to be accurate. However, the description of the atmosphere by

Table 4.10.: r_{68} of Monte Carlo simulations with 10% and 20% of broken pixels and without broken pixels, for Std cuts. The numbers for "all" were calculated with added θ^2 plots of all MC for the respective percentage of broken pixels, i.e. the events for the spectral indices of 2.0, 2.4, 2.6, 2.8, 3.0, 3.2 and 3.4 were accumulated. r_{68} are given in 10^{-2} deg.

index	0 %	10 %	20%
2.0	6.67 ± 0.03	6.83 ± 0.04	6.89 ± 0.04
2.4	7.05 ± 0.05	7.08 ± 0.05	7.17 ± 0.05
3.2	7.75 ± 0.09	7.74 ± 0.10	7.71 ± 0.10
all (added)	7.14 ± 0.02	7.17 ± 0.02	7.17 ± 0.02

Table 4.11.: Same as in Table 4.10, but for HiRes cuts.

index	0 %	10 %	20%
2.0	4.74 ± 0.03	4.81 ± 0.03	4.85 ± 0.03
2.4	5.08 ± 0.05	5.05 ± 0.05	5.24 ± 0.05
3.2	5.89 ± 0.10	6.04 ± 0.11	5.90 ± 0.10
all (added)	5.08 ± 0.02	5.13 ± 0.02	5.17 ± 0.02

Table 4.12.: Same as in Table 4.10, but for Faint cuts.

index	0 %	10 %	20%
2.0	6.43 ± 0.04	6.34 ± 0.04	6.41 ± 0.04
2.4	6.53 ± 0.06	6.47 ± 0.05	6.60 ± 0.05
3.2	7.14 ± 0.10	7.16 ± 0.11	7.13 ± 0.11
all (added)	6.62 ± 0.02	6.57 ± 0.02	6.59 ± 0.02

Table 4.13.: Apparent source size of the Crab Nebula and PKS 2155−304 for runs with less than 5% and more than 10% of broken pixels in at least three or in four cameras, respectively. The table entries are σ_a in 10^{-2} deg.

source	cuts	< 5%		> 10%	
		4Tels	≥ 3Tels	≥ 3Tels	4Tels
Crab	Std	0.5 ± 0.9	2.2 ± 0.1	2.5 ± 0.1	2.4 ± 0.3
	HiRes	0.0 ± 0.5	2.0 ± 0.1	2.0 ± 0.1	1.3 ± 0.4
	Faint	0.4 ± 1.0	2.2 ± 0.1	2.2 ± 0.1	2.3 ± 0.3
PKS	Std	2.7 ± 0.4	2.42 ± 0.06	1.8 ± 0.2	1.1 ± 1.3
	HiRes	2.3 ± 0.5	1.97 ± 0.07	1.8 ± 0.2	0.2 ± 1.5
	Faint	2.1 ± 0.5	1.74 ± 0.08	1.0 ± 0.3	0.0 ± 1.6

the "Windhoek Average" model might be insufficient. Atmospheric conditions change rapidly on the H.E.S.S. site, and their large variation manifests itself in a broad range of trigger rates, for example. Its influence is even seen in reconstructed fluxes. Furthermore, depending on the region in the sky, the level of NSB differs. The MC simulations are generated for the NSB level of the night sky around the Crab Nebula (0.1 GHz), which is similar or higher than the NSB level for most extra-galactic sources. However, in regions like Eta Carinae, the NSB rate can reach ∼10 times that value. Camera images are contaminated by pixels triggering on NSB photons, and if such pixels end up next to pixels defined as the shower (see Sec. 3.3) the *Model* fit may be affected.
Mechanical effects like the fluttering of cameras in the wind or vibrations of the whole telescope structure might lead to a widening of the PSF as well. Such effects are neither studied nor included in the mechanical models of the telescopes, not to mention in the simulations. The electronics of the H.E.S.S. cameras and statistical processes taking place in them are simulated, but their uncertainities might be underestimated. A wider spectrum of electronic noise was introduced in some example simulations. Applying the same analysis procedure as for the MC production used throughout this work, the values of r_{68} are found to be larger by 0.003°, which is nearly 1/3 of the current mismatch in r_{68} between MC and data PSF.
Another source of systematic PSF errors might be the homogeneous treatment of all four telescopes. For example, the muon efficiencies of the four telescopes usually differ by ∼10%, but in the simulations four telescopes with the same muon efficiency are assumed. Run-wise simulations that contain the actual properties of each telescope (number and position of broken pixels, electronic response, muon efficiency etc.) might fix the phenomenon of apparently extended sources at least partly.

4.6. Summary

In summary, a mismatch between data and MC PSF is present under all observation conditions and for all studied sources. Compared to the data, the MC PSF is too narrow, leading to apparent source sizes of $\sim 0.015^\circ - 0.03^\circ$. Except for the index dependence and the missing interpolation between an azimuth angle of 0° and of 180°, the MC simulations describe the behaviour of the PSF well. An estimation of all systematic errors on the PSF is shown in Table 4.14. The apparent source sizes therein are calculated for a range of observation conditions. The upper values display the systematic errors in a worst-case scenario, i.e.

- a zenith angle of 60°, which is usually the maximum zenith angle for H.E.S.S. observations,
- a source observed in the south, passing through azimuth angles close to 90°,
- a spectral index $\Gamma = 3.2$.
- an off-axis angle of 2°.

Except for the pointing, the errors can take positive and negative values. The numbers indicate that there is much room for improvement. Most efficiently, the systematic error on source size measurements can be reduced by introducing an azimuth interpolation. Still, a systematic error related to the azimuth would remain because the effect of the magnetic field on the PSF is probably not linear, the deformation of shower ellipses is different in the East and in the West and the magnetic field lines are not perfectly aligned with the North-South direction.

Table 4.14.: Systematic errors on the apparent source size caused by the effects studied in this work. The resulting apparent source sizes are given as Gaussian widths in 10^{-2} deg.

effect	size	σ_{syst}, Std
azimuth interpolation		0.0 - 2.0
muon efficiency syst.	5%	0.7 - 1.0
muon efficiency stat.	3%	0.5 - 0.8
spectral index syst.	0.1	0.0 - 0.7
spectral index stat.	$\Delta\Gamma$	0.0 - $8{\cdot}10^{-3} \cdot \Delta\Gamma$
spectral index dep.		$\leq$0.5
zenith angle dep.		$\leq$0.1
MC statistics	1σ	0.3 - 2.0
Pointing		$\leq$ 0.8
Broken Pixels	max. found	$\leq$ 1.1
1σ systematic errors		0.9 - 3.5

The error on MC statistics can quite easily be avoided by simulating more events, especially at high zenith angles and high off-axis angles. Third in size are the systematics caused by the errors on the muon efficiency. Although they cannot be avoided with the current method of muon efficiency determination, in a few seconds of observations without coincidence requirement enough muon rings could be measured to drastically reduce the statistical error.
The smearing of the PSF by mis-pointing is inevitable, but it could be significantly reduced if the "precision pointing" developed in Braun (2007) was employed in H.E.S.S. observations. However, the method was not systematically checked for its robustness under different observation conditions.
Estimating the systematics of the spectral index and how they could be avoided is a work on its own. A different approach would be to use the distribution of reconstructed energies for PSF calculation instead. However, such a distribution would be contaminated by background events. That approach is followed in the ctools software package[3], which is being developed to fit the energy and direction of each event simultaneously in three-dimensional fits.
Besides, systematics could be reduced by introducing run-wise simulations, as mentioned above, since the homogeneous treatment of all telescopes an the approximation of a stable atmosphere could have effects on the PSF, although not mentioned in Table 4.14.
In the next chapters, two phenomena that require a thorough understanding of the PSF are searched for: Extended emission from the Crab Nebula and around AGN.

[3] Available at http://cta.irap.omp.eu/ctools.

5. The size of the Crab Nebula at VHE

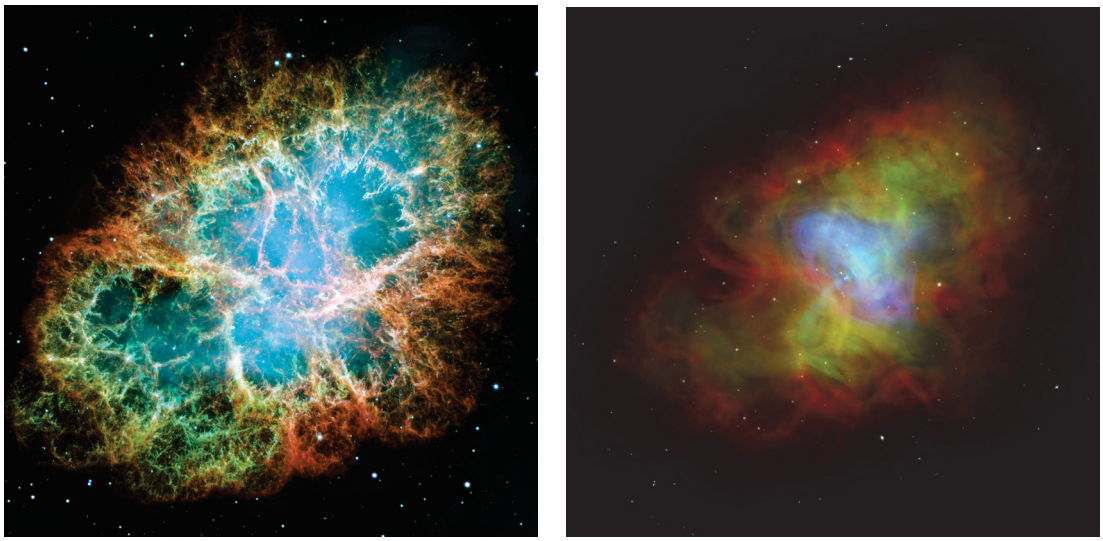

(a) (b)

Fig. 5.1.: (a) Composite image of the Crab Nebula in the light of different optical and UV emission lines, taken by the *Hubble Space Telescope*. Emission by [O III] is shown in red, [S II] in green, and [O I] in blue. In addition, the optical emission of the nebula, filling the "cage" of filaments, is shown in blue. The angular size of the image is ∼7'× 7'. Image Credit: NASA, ESA and Allison Loll/Jeff Hester. (b) Composite image of the Crab Nebula of the same size, displaying radio measurements in red, the optical emission detected by the *Hubble Space Telescope* as in (a) in green, and and X-ray emission detected by the *Chandra* satellite in blue. Credits: X-ray: NASA/CXC/ASU/J. Hester et al.; Optical: NASA/HST/ASU/J. Hester et al.; Radio: NRAO/AUI/NSF

After Chinese astronomers saw the "guest star", the supernova of 1054, even during daylight for three weeks (Clark & Stephenson 1977), it disappeared from human awareness until John Bevis discovered the corresponding nebula in 1713. 45 years later, Charles Messier declared it to be the first object in his catalogue of nebular objects. At the end of the 19^{th} century, William Parsons, third Earl of Rosse, gave the nebula the name that it is known under nowadays: the Crab Nebula. Today, the Crab Nebula is one of the most-studied astronomical objects beyond our solar system (for a review, see, e.g., Hester (2008)). At VHE, it is the brightest invariable source in the sky and it was the first object detected in that energy band (Welford & Winston 1989).
The Crab Pulsar is the neutron star remaining of the progenitor of SN 1054, and the Crab Nebula is the PWN powered by it. It is the prototype of a young PWN, but at the same time it is an exceptional specimen of that class due to the high conversion efficiency of the spin-down luminosity of its pulsar into synchrotron radiation (Kennel & Coroniti 1984). This property and its proximity of ∼2 kpc (Trimble 1973) make the Crab, referring to the pulsar and the nebula, "one of our prime laboratories to study non-thermal processes in

the Universe" (Bühler & Blandford 2014). Although it was deeply observed in the past 100 years, it does not cease to surprise even the experts, for example by the giant outbursts at MeV energies that were first detected in 2010 (Abdo et al. 2011; Tavani et al. 2011) and are not visible in any other energy band (see Appendix A).
The nebula is visible at all wavelengths, spanning from radio to TeV γ-rays. Depending on the energy band of the observation, it displays different features and morphologies (see Fig. 5.1(b)). This chapter aims at deriving an upper limit (U.L.) on the size of the TeV γ-ray emission of the Crab Nebula. First, an introduction to the morphological components of the Crab Nebula and the wavelengths they are visible in is given. The relationship between the morphology at GeV and TeV energies is sketched and model predictions as well as existing upper limits for the size of the VHE γ-ray emission region are presented. Finally, with the knowledge gained in the previous chapter, the H.E.S.S. PSF is calibrated and the size of the Crab Nebula is measured. A detailed accounting of the systematic errors is presented in order to obtain an upper limit.

5.1. Energy-dependent morphology

As mentioned above, the morphology of the Crab Nebula depends on the energy band of the observation. To estimate the expected morphology of the emission at VHE γ-rays, an understanding of the energetics and the structure of the whole complex, consisting of the pulsar, the PWN and the invisible SN ejecta, is necessary.
The outermost layer connected to the Crab is the shell of invisible supernova ejecta of SN 1054. They are in a free expansion phase and probably did not hit enough interstellar material to be radiating (yet). The existence of expanding ejecta is assumed because of the properties of the shock that is driven into them by the synchrotron nebula (Hester 2008). The shock causes Rayleigh-Taylor instabilities that manifest themselves as inward-pointing filaments of dense gas (Hester et al. 1996). The photo-ionised gas is visible in optical and UV emission lines, see Fig. 5.1(a). The SN ejecta limit the nebula to a size of $\sim 4.4\text{pc} \times 2.9$ pc (Hester 2008), which corresponds to $0.13^\circ \times 0.08^\circ$.
The central engine of the PWN is the Crab Pulsar (Pacini 1967), which has a rotation period of 33 ms (Cocke et al. 1969). It is visible as the central bright point in Fig. 5.2. As described for PWNe in general in Chapter 2, it generates a cold wind of relativistic particles which flow freely along the magnetic field lines. Due to magnetic collimation effects, the particle wind forms a torus and jets. These features are clearly visible in the Crab Nebula, see Fig. 5.2. The jets are almost aligned with the major axis of the ellipsoidal nebula as seen in Fig. 5.1(a) ($\sim$45° running from South-East to North-West), and are known to be tilted into the plane of the sky at an angle of $\sim$30° (pointing to the north-west direction) (Loll et al. 2007).
To match the boundary condition of the relatively slowly expanding SN ejecta, the ultra-relativistic particles of the wind need to be decelerated. This occurs at the termination shock (Rees & Gunn 1974), which marks the point of equilibrium between the ram pressure of the pulsar wind and the pressure of the particles in the nebula. At the termination shock, the momenta of the electrons and positrons are isotropised, i.e. they are no longer aligned with the magnetic field and start to emit synchrotron radiation. For the Crab Nebula, Rees & Gunn (1974) predict the termination shock to have a radius of $\sim 0.003^\circ$. This prediction roughly matches the radius of the "inner ring" in Fig. 5.2, which has a radius of $\sim 0.004^\circ$.
The termination shock is thought to be the birth place of the nebular electron spectrum[1] .

[1] This is only partly true. There are, most probably, two electron populations - the primordial electrons

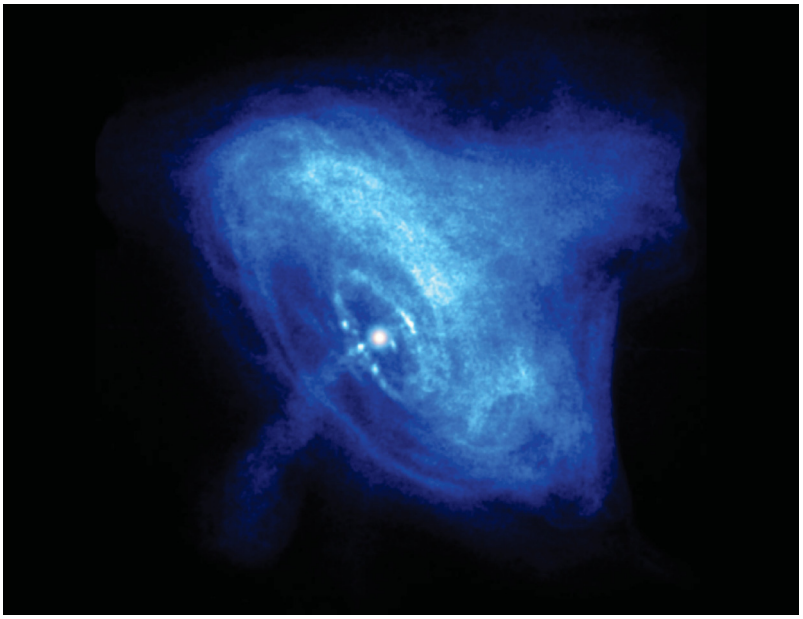

Fig. 5.2.: Soft X-ray emission of the Crab Nebula in the energy range of 0.3 – 10 keV observed by the ACIS instrument on-board the Chandra satellite.

The synchrotron and IC emssion of the electrons manifest themselves in two broad peaks in the spectral energy distribution, that intersect at ∼600 MeV (see Fig. 5.3).
Due to the high magnetic field of the Crab Nebula, the synchrotron photons are the dominant photon field in the energy range relevant for the IC process, hence the scenario is called "synchrotron-self-compton" (SSC, see, e.g. Gould 1965; de Jager & Harding 1992; Atoyan & Aharonian 1996). However, infrared (IR) photons of dust emission (visible as the narrow peak in Fig. 5.3), starlight and the cosmic microwave background (CMB) also contribute as target fields for IC scattering.
The morphology visible in VHE γ-rays is thus determined by the density of the photon fields and the spatial distribution of electrons with sufficiently high energies. Since the particles are accelerated at the termination shock and then cool adiabatically via synchrotron radiation, the most energetic particles are found close to the shock and the size of the nebula increases with decreasing energy in both peaks of the Crab Nebula spectrum. While the Crab Nebula can be morphologically resolved at different synchrotron energies, the size of the IC emission region is unknown. To give an estimate of the expected size of the Crab Nebula at energies of (0.5 – 10) TeV, a simple approximation of the synchrotron photon energies imaging the same electrons is given in the following.
The IC up-scattering of synchrotron photons to γ-rays with energies above 200 GeV takes place in the Klein-Nishina scattering regime rather than in the Thomson regime (Hillas et al. 1998). To produce photons with an energy E_γ (in units of TeV), electron energies of

$$E_e \approx 5E_\gamma \cdot (\frac{E_\gamma}{1\,\mathrm{TeV}})^{-0.12}, \tag{5.1}$$

are required according to Hillas et al. (1998). Following de Jager & Djannati-Ataï (2009),

(the SN-accelerated ones that now mostly radiate at radio energies) and the wind electrons, see Atoyan & Aharonian (1996).

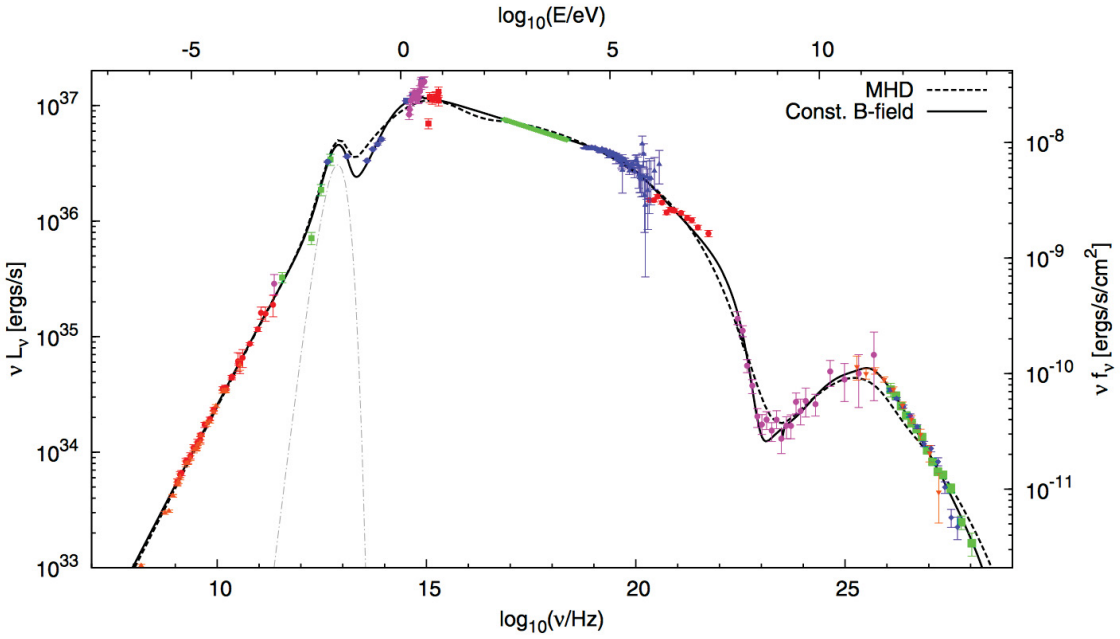

Fig. 5.3.: Spectral energy distribution of the Crab Nebula. Figure taken from Meyer et al. (2010), based on observational data compiled in Aharonian et al. (2004).

an electron needs a minimum energy of

$$E_e = (70\,\mathrm{TeV})\sqrt{\frac{E_{\mathrm{keV}}}{10^5 B_G}} \tag{5.2}$$

to radiate synchrotron photons with a mean energy of $\mathrm{E_{keV}}$ (in units of keV) in a transverse magnetic field with a strength B_G in units of G. Assuming that the main target field for the IC process are the synchrotron photons, the relation between IC up-scattered photons and synchrotron photons originating in electrons of the same energy can be written as

$$E_{\mathrm{keV}} = \left(\frac{5E_\gamma (E_\gamma/1\,\mathrm{TeV})^{-0.12}}{70\,\mathrm{TeV}}\right)^2 \cdot 10^5 B_G. \tag{5.3}$$

Meyer et al. (2010) find the average B-field in the Crab Nebula to be $(124 \pm 6(\mathrm{stat})\,^{+15}_{-6}(\mathrm{syst}))\ \mu$G. Inserting this value into the equations above and assuming VHE photon energies in the range of (0.5 – 10) TeV, the required electron energies are roughly (3 – 40) TeV while the photons of the target field must have energies of (0.013 –3.6) keV. The upper part of this energy range is covered by the Chandra satellite, which detects photons with energies of (0.3 – 10) keV. Therefore, the size of the TeV emission should be similar to what is depicted in Fig. 5.2, i.e. $\sim$0.03° in diameter, or even larger. Parametrizing the morphology with a Gaussian, widths of $\sim$0.01° are expected.
Following a similar reasoning, Hillas et al. (1998) describe the energy-dependent morphology of the Crab Nebula empirically with a Gaussian of a width

$$\sigma_H = (0.47 + 3.46[E_{\mathrm{eV}}/0.02\,\mathrm{eV}]^{-0.09}) \cdot 180/\pi \cdot 10^{-4}\,\mathrm{deg} \tag{5.4}$$

for energies E_{eV} (in units of eV) above 0.02 eV. Hence, the size of the synchrotron photon emission corresponding to the TeV range of (0.5 – 10) TeV would be (0.009 – 0.014)° in diameter.

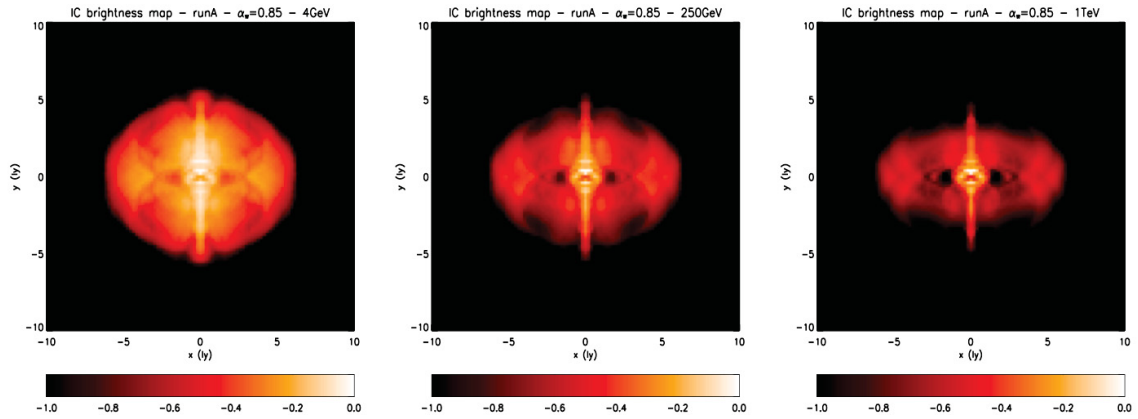

Fig. 5.4.: Total surface brightness in logarithmic scale resulting from the 2D MHD simulations in Volpi et al. (2008) at different IC energies. 1 ly corresponds to $\sim 0.009^\circ$.

However, unlike in Eq. 5.4, the morphology is not a simple Gaussian, but displays a torus and jets and the magnetic field is not expected to be constant throughout the nebula. In addition, the target photon field for IC scattering consists of three components (synchrotron, far IR and CMB), each displaying a different spectrum and a different morphology. To model the processes in the Crab Nebula adequately, all of that information needs to be included. This was done most recently by Volpi et al. (2008) in 2D magneto-hydro-dynamical (MHD) simulations and by Porth et al. (2014) in 3D MHD simulations. Volpi et al. (2008) present surface brightness maps of the IC emission, which reproduce the morphological features visible in Fig. 5.2 well, see Fig. 5.4. According to the map for IC photon energies of (0.85 – 1) TeV, the jet brightness stays at 60% of the maximum flux at these energies even at distances of $\sim$2 ly from the pulsar, i.e. the jet axis appears extended with a length of almost 0.04° .
Measurements of the emission region size can confirm or exclude such model predictions. The size of the synchrotron photon field and the spatial distribution of electrons, depending on the energy, are important input parameters also for purely spectral simulations like the one presented in Meyer et al. (2010). A measurement or upper limits on the size of the TeV emission would impose boundary conditions on the distributions and thereby restrict the scenarios of IC and synchrotron photon production in the Crab Nebula.
Experimentally, no extension of the VHE emission has been found yet. The most restricting upper limits were provided by Aharonian et al. (2000) using data taken with the HEGRA experiment. By selecting events with small errors on the direction reconstruction, similarly to the HiRes event selection, angular resolutions as low as 0.03° (Gaussian width) were achieved. The lowest statistical 99% upper limit on the size of the Crab Nebula in that publication is 1' (0.017° , given as a Gaussian width). Including systematic errors due to mis-pointing, extensions larger than 1.5' (0.025°) were excluded.
Also with HEGRA observational data, Aharonian et al. (2004) excluded extensions larger than 2' (0.033°) for energies between 1 TeV and 10 TeV at a 99% confidence level. The angular resolution was given as a Gaussian width of 0.06° (corresponding to $r_{68} = 0.09$), and the systematic pointing error of 25" (0.007°) was included in the limit. Employing monoscopic data taken with the MAGIC telescope, Albert et al. (2008) determine an upper limit on the Crab Nebula size of 0.037° at a 95% confidence level (C.L.) for energies above 500 GeV. In this energy range, the authors determined an $r_{68} \approx 0.1^\circ$ for their PSF. No details on the possible effect of systematic errors were given. Compared to the reconstruction

methods used in these three publications, the *Model Analysis* is more advanced and even better angular resolutions can be reached. However, for source sizes far smaller than the PSF, systematic effects dominate extension measurements. In the next section, the size of the VHE γ-ray emission region of the Crab Nebula is probed employing H.E.S.S. data and the *Model Analysis* with different cut configurations, and systematic effects are considered in detail.

5.2. Morphology with H.E.S.S.

From the studies of the PKS 2155−304 flare data set it is clear that the MC PSF is too narrow. However, in Sec. 4.5, the cause of this systematic mismatch could not be identified. Except for a slight dependence on the spectral index and the missing azimuth interpolation, no dependence between the mismatch and observational quantities was found. Therefore, in the following, the MC PSF is calibrated on the PKS 2155−304 flare data set in order to measure the size of the Crab Nebula correctly.

5.2.1. Calibration of the MC PSF

To achieve an agreement between the MC PSF and the point-like nature of the PKS 2155−304 flare, the MC PSF needs to be widened. The widening of the MC PSF was performed by applying a Gaussian smearing to the simulated events which are filled into the *Morphology Tables*. The width of the Gaussian was chosen as the apparent size of the PKS 2155−304 flare as given in Sec. 4.4. With the three measurements for Std, Faint and HiRes cuts, new *Morphology Tables* for the corresponding cuts were generated. To check whether the procedure results in the desired dissappearance of the source size of the PKS 2155−304 flare, the same data set was re-analysed with the new tables. The results are listed in Table 5.1, showing that no significant extension is found anymore. Additionally, the effect on the binary systems and AGNs presented in Sec. 4.4 was tested. The source sizes fitted with the new tables are shown in Fig. 5.5. To measure their offset from 0° , their Likelihood Profiles were fitted simultaneously. The original best-fit constant of 0.022° decreases to 0.013° for Std cuts, and a similar decrease is found for HiRes and Faint cuts, see Table 5.2. The differences in size between the sources and between the analysis cuts give an estimate of the remaining systematics, which are partly induced by the index dependence of source size measured with Std and HiRes cut configurations. Most source sizes are compatible with 0° within 3σ and many even within 1σ for HiRes cuts.

Table 5.1.: Apparent size of the PKS 2155−304 flare data set, fitted with the widened morphology tables. -3σ, -1σ, +1σ and +3σ denote the minimum/maximum size in agreement with the measurement at the respective confidence level, according to the statistical errors on the Likelihood Profiles.

cuts	-3σ	-1σ	σ_a [10^{-2} deg]	+ 1σ	+ 3σ
Std	0.0	0.0	0.2	0.4	0.9
HiRes	0.0	0.3	0.8	1.10	1.30
Faint	0.0	0.0	0.4	0.6	0.9

Table 5.2.: Mean apparent source size of the eight AGN and two binaries listed below, fitted with the old and the new, widened *Morphology Tables*.

cuts	σ_a, old [10^{-2} deg]	χ^2/ndf	σ_a, new [10^{-2} deg]	χ^2/ndf
Std	2.06 ± 0.1	9.4/9	1.03 ± 0.04	9.7/11
HiRes	1.70 ± 0.1	8.0/9	0.71 ± 0.05	10.4/11
Faint	1.81 ± 0.1	5.6/9	0.93 ± 0.05	12.9/11

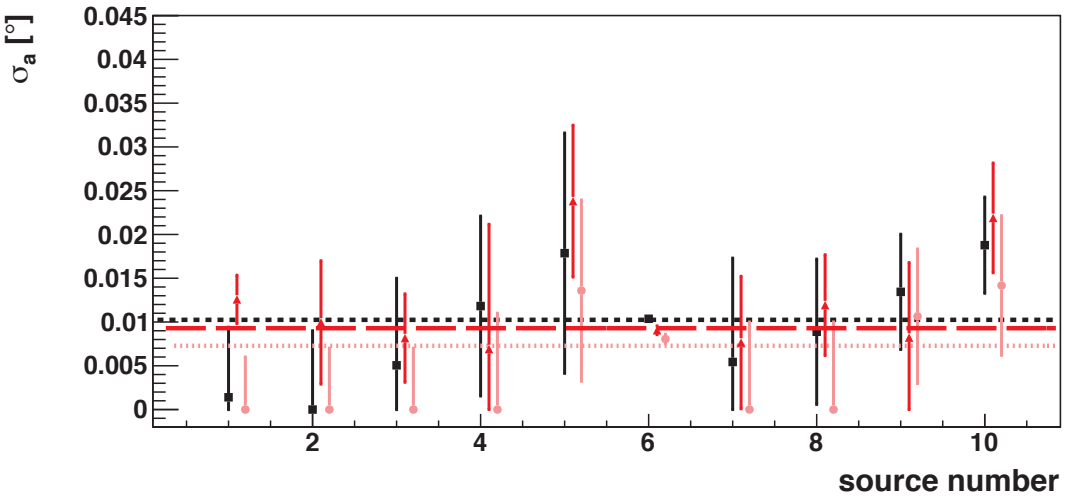

Fig. 5.5.: Apparent source sizes of the eight AGN and two binaries listed below, fitted with the new, widened MC PSF. The mean apparent size is estimated by the fit of a constant, which is depicted as the black dashed line for Std cuts, a red dashed line for Faint and a pink dashed line for HiRes cuts.

1 - LS 5039 4 - PKS 1514−241 7 - 1ES 0229+200 10 - PKS 0447−439
2 - HESS J0632 5 - PKS 0548−322 8 - 1ES 1101−232
3 - M 87 6 - PKS 2155−304 9 - 1ES 0347−121

5.2.2. Application to the Crab Nebula data

As concluded in Chapter 4, the systematic errors on the PSF can result in apparent source sizes similar to what is expected for the Crab Nebula size at TeV energies. For a source as bright as the Crab Nebula and the total number of H.E.S.S. observation runs pointed at it, the systematic errors outweigh the statistical errors by far. To reduce the systematic errors and to be able to estimate them correctly, a strict run selection is applied. In the following, the selection parameters and the resulting distribution of the runs in the parameter space important for PSF generation will be presented. Subsequently, a fit of the source position and morphology fits with a symmetric and an asymmetric Gaussian model are shown for the chosen sample.

Run selection and position fit

Taking into account the results of the PSF studies described in Chapter 4, a sample of H.E.S.S. runs on the Crab Nebula was selected. Only runs taken with all four telescopes at wobble offset angles of 0.5° and lasting more than 25 minutes were chosen. The zenith

angle range was restricted to <50° for two reasons: First, the MC PSF is smaller and has lower statistical errors in that range; second, the azimuth angle is limited to ±30° by that restriction. Although no conclusion on the effect of broken pixels could be found, the maximum broken pixel percentage was set to 10% in all of the four telescopes to avoid a possible widening of the PSF on the one hand, and to make the data set comparable to the PKS 2155−304 flare data set on the other hand.

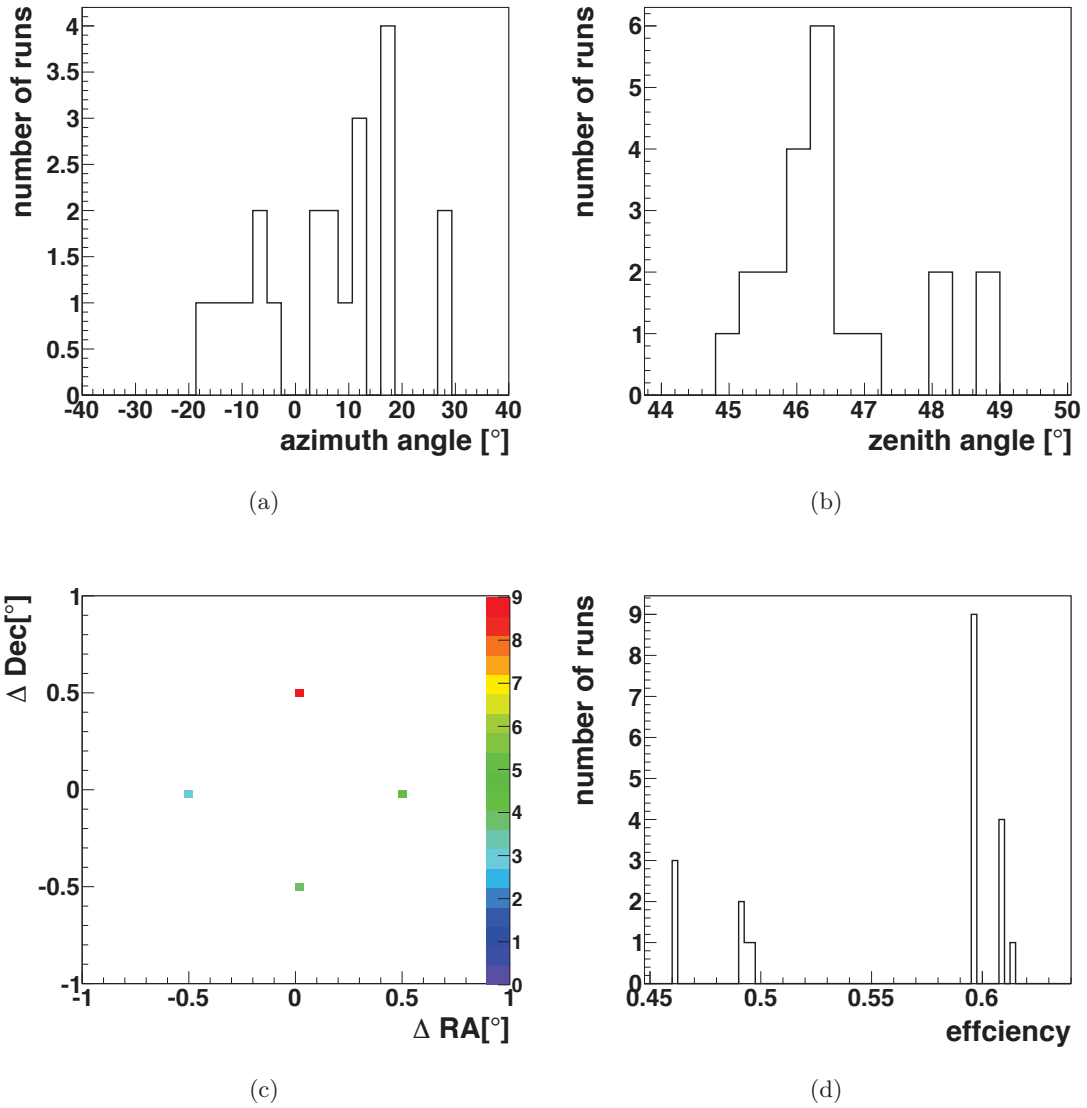

Fig. 5.6.: Distribution of (a) mean azimuth angles, (b) mean zenith angles, (c) wobble positions and (d) muon efficiencies of the selected runs on the Crab Nebula.

The 21 runs that pass this selection were taken in the years 2004 to 2009. The distributions of their mean zenith angles, azimuth angles, offset angles and muon efficiencies are shown in Fig. 5.6. By analysing these runs and fitting a point source model to the event distribution, the best fit position was found to be (RA = 83d 37' 43.2" ± 2.5"| Dec = 22d 0' 46.2" ± 2.4"). The result is visualised in Fig. 5.8. The centre of the emission found here is compatible with the pulsar position and with the position found by Aharonian et al. (2004) within systematic pointing errors. It was used to re-analyse the data and to generate a θ^2

histogram centered on that position.
For an analysis region with a radius of 0.1° , a spectrum was produced. A fit with a power law yields a normalisation of 41.9± 0.8)·10^{-8}m^{-2}s^{-1} TeV^{-1} at 1 TeV and a spectral index of 2.71±0.03, which is compatible with the measurement published in Aharonian et al. (2006a) within systematic errors. While the minimum event energies found in the data are ∼300 GeV, the threshold of the spectal fit is ∼500 GeV.
The θ^2 excess histogram and the spectral index were used for the morphology fits described subsequently.

Upper limit on the size

The fit of an exponential function (see Eq. 4.9), convolved with the MC PSF, yields extension measurements that are statistically significant. They are summarised in Table 5.3 and visualised in the form of Likelihood Profiles in Fig. 5.7. However, the measurement is dominated by systematic effects and well compatible with the AGN sizes found in the last section. Going through the known sources of systematic errors one by one, an upper limit on the size of the Crab Nebula at TeV energies will be calculated subsequently.
Since the Crab Nebula is located in the North, the missing azimuth interpolation leads to an underestimation of r_{68} of the MC PSF ($r_{68,MC}$) of up to 0.0017° for an azimuth difference of 30° and zenith angles of up to 50° , as in the chosen data sample (see Fig. 4.16(b)). Thus the source appears larger than it should already, and no systematic error must be added to the upper limit to account for the azimuth dependence.
The same applies for the pointing error. It widens the distribution of the data, but it is not included in the MC PSF, hence the source can only be smaller than the size measured here. This statement is still true for the calibrated MC PSF, since the pointing jitter is at most partly included in the PKS 2155−304 flare sample. The three runs of the PKS 2155−304 flare were taken one after the other at low zenith angles, therefore the mispointing by bending of the telescope structure is probably rather small.
The off-axis angle is the same as for the PKS flare runs, therefore the size measurement is not affected by that parameter. The same assumption is made about broken pixels - since 5 – 10% of camera pixels were broken in the PKS 2155−304 flare runs, the effect on the Crab Nebula sample should be the same. If there is an incrase in r_{68} with broken pixel percentage, it would be incorporated in the Gaussian smearing used to correct the MC PSF.
A systematic influence that cannot be avoided is the error on the muon efficiency. It is assumed to consist of a 5% systematic error and 3% statistical error, which could lead to an overestimation of $r_{68,MC}$ of the MC PSF by 0.0018° (see Fig. 4.19(b)). This would make the Crab Nebula appear too small by ∼0.012° employing Eq. 4.15, since $r_{68,MC}$ was found to be 0.0712° for this sample employing the widened *Morphology Tables* for Std cuts. Values for HiRes and Faint cuts were calculated using the corresponding tables, resulting in a systematic error on the Crab Nebula size of 0.009° and 0.010° , respectively.
No dependence on the zenith angle was found, except for a tendency to fit smaller source sizes at larger zenith angles for HiRes cuts (see Fig. 4.20). Following the parametrisation of the zenith dependence of PKS 2155−304 from Table 4.6, the size decreases with (14 ± 2)·10^{-5} deg per degree of zenith angle. Since the effect of the missing azimuth interpolation is included in the slope, it needs to be subtracted. A linear estimation of the decrease in source size with increasing azimuth distance from 180° for PKS 2155−304 results in 5·10^{-5} deg per degree of zenith angle. Taking the 2σ fit errors into account, a slope of 13·10^{-5} deg per degree of zenith angle remains. The difference between a zenith angle of

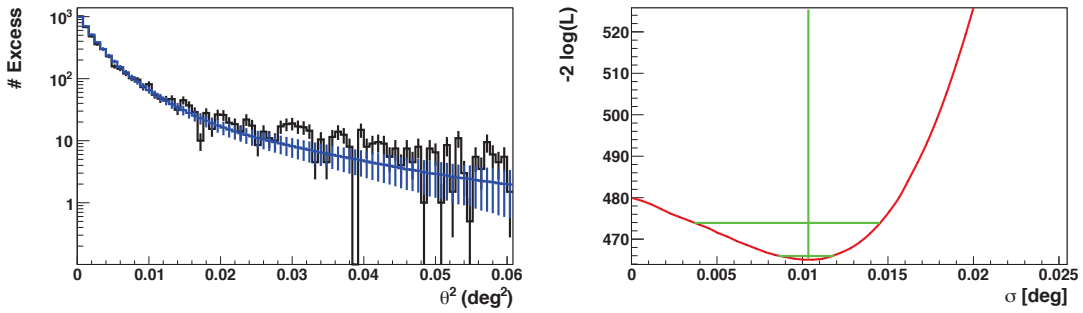

(a) Std

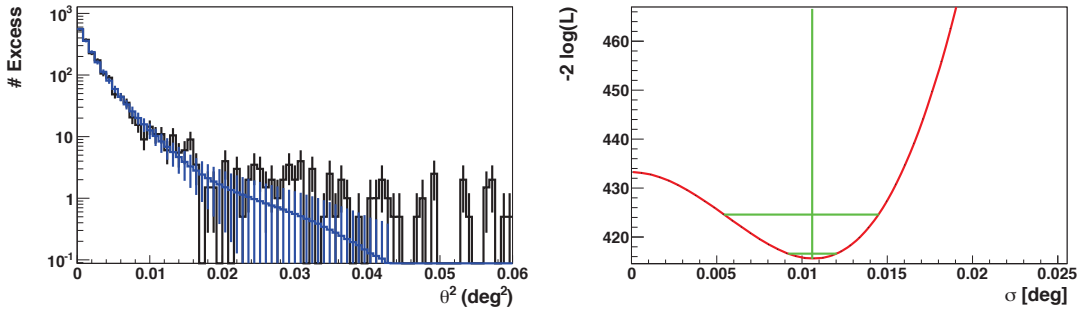

(b) HiRes

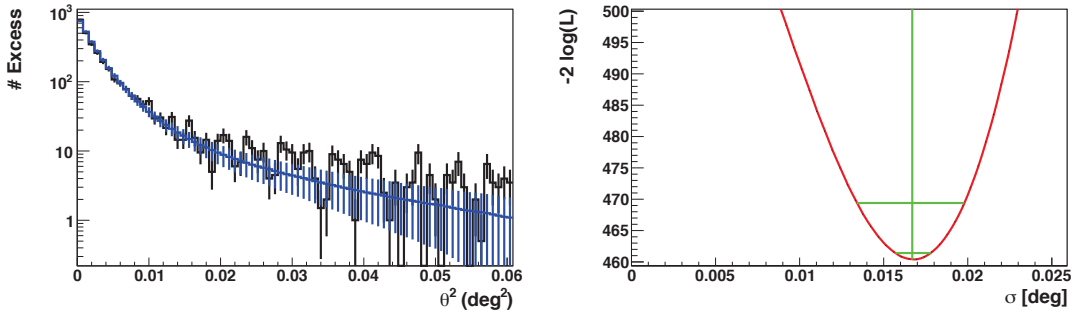

(c) Faint

Fig. 5.7.: *Left panels*: Fitted excess distribution of the Crab Nebula in logarithmic representation. The data are depicted in black, the fitted function in blue. *Right panels*: Log-likelihood profiles of the parameter σ_a. The negative log-likelihood function is shown in red, a vertical green line marks the best-fit position and horizontal green lines visualize 1σ (lower) and 3σ (upper) error intervals. From top down, the dataset was analysed with (a) Std, (b) HiRes and (c) Faint cuts and the corresponding widened MC PSF was used for the fit.

Table 5.3.: Apparent size of the Crab Nebula σ_a and its confidence intervals, all in $[10^{-2}\,\mathrm{deg}]$, for different analysis cuts.

cuts	-3σ	- 1σ	σ_a	+ 1σ	+ 3σ
Std	0.37	0.86	1.04	1.19	1.46
HiRes	0.54	0.92	1.07	1.20	1.45
Faint	1.34	1.57	1.68	1.78	1.98

13° , where the PKS flare measurement lies, and the mean zenith angle of the sample at hand (46.5°), is 33.5° , leading to a systematic error on σ_a of 0.0043° for HiRes cuts. For Std and Faint cuts, the calculation has been done with the corresponding slopes. Since the zenith angle dependence is not signficant for these cases, the systematic error is given as a 2σ upper bound.
A larger systematic error comes from the uncertainties on the spectral index. In addition to the systematic error of 0.1 on the index from the spectral fit, an error is made because of the power law assumption of the spectral shape. For a power law with an exponential cutoff, an index of 2.39 ± 0.03 and a cutoff energy of 14.3 ± 2.1 were found as the best fitting spectral description for the Crab Nebula in Aharonian et al. (2006a). Conservatively assuming that the energy distribution of the Crab Nebula rather follows a power law index of 2.39 (which is reasonnable, since the vast majority of events has energies below 10 TeV), $r_{68,MC}$ would be $4{\cdot}10^{-4}$ smaller (see Fig. 4.22(b)). Adding the error on r_{68} stemming from the systematic error on the index, Δr_{68} would be $6{\cdot}10^{-4}$. For the given sample, the source would then appear to be 0.0061° larger (0.005° for HiRes, 0.0056° for Faint cuts). Furthermore, an index dependence of the fitted source sizes was found for Std and HiRes cuts. Following the parametrisation from Table 4.9, the apparent source size diminishes by 0.0067° for Std and 0.0048° for HiRes cuts when accounting for an index difference of 0.95 between the Crab Nebula and PKS 2155−304. For Faint cuts, no dependence was found. The systematic 1σ error is therefore estimated to be smaller than the effect of the 2σ errors of the fitted slope.
The systematic error on r_{68} arising from limited MC statistics is 0.006° at 50° zenith angle for the lowest muon efficiency and an off-axis angle of 0.5° (see Fig. 4.8(d)).
All the effects influencing the systematic error are summarized in Table 5.4 for Std, HiRes and Faint cuts. Partly, they may already be included in the calibration on the PKS 2155−304 flare data set. For example, if the measured muon efficiencies were systematically shifted to lower values, the MC PSF would always appear too small compared to the data. Similarly, a systematic under-estimation of the spectral index would have the effect of apparently extended sources. If the contribution of such systematic shifts was known, the overall systematic error on the source size measurement would diminish accordingly.
The positive systematic errors are quadratically added to the 2σ statistical extension limit. Under the assumption that the PKS 2155−304 flare of 2006 displays a point source for H.E.S.S. , the 95% C.L. upper limit on the size of the Crab Nebula above 0.5 TeV is 0.034° for Std cuts, 0.032° for Faint cuts, and 0.029° for HiRes cuts. The missing azimuth interpolation and the pointing jitter lead to an asymmetric error on the source size measurement. These two components do not affect the U.L., but they imply that even the measurement of a larger size would be compatible with a point source nature of the VHE emission. The largest contributions to the systematic error are the errors on the muon efficiency and on the spectral index. While the statistical error on the muon efficiency could be reduced, as proposed in Sec. 4.6, dedicated studies would be necessary to reduce the systematic errors on both muon efficiency and spectral index.

Table 5.4.: Systematic effects on the apparent size of the Crab Nebula given as Gaussian widths in 10^{-2} deg.

effect	size	σ_{syst}, Std	σ_{syst}, HiRes	σ_{syst}, Faint
muon efficiency syst.	5%	0.97	0.80	0.90
muon efficiency stat.	3%	0.66	0.54	0.61
spectral index syst.	0.3	0.61	0.50	0.56
spectral index stat.	0.03	0.02	0.02	0.02
spectral index dep.		0.67	0.48	<0.19
zenith angle dep.		<0.10	0.43	<0.2
MC statistics	1σ	0.60	0.40	0.60
pointing		0.62	0.62	0.62
azimuth		1.03	0.87	0.95
1σ errors		- 1.94 + 1.60	-1.71 + 1.33	- 1.78 + 1.39

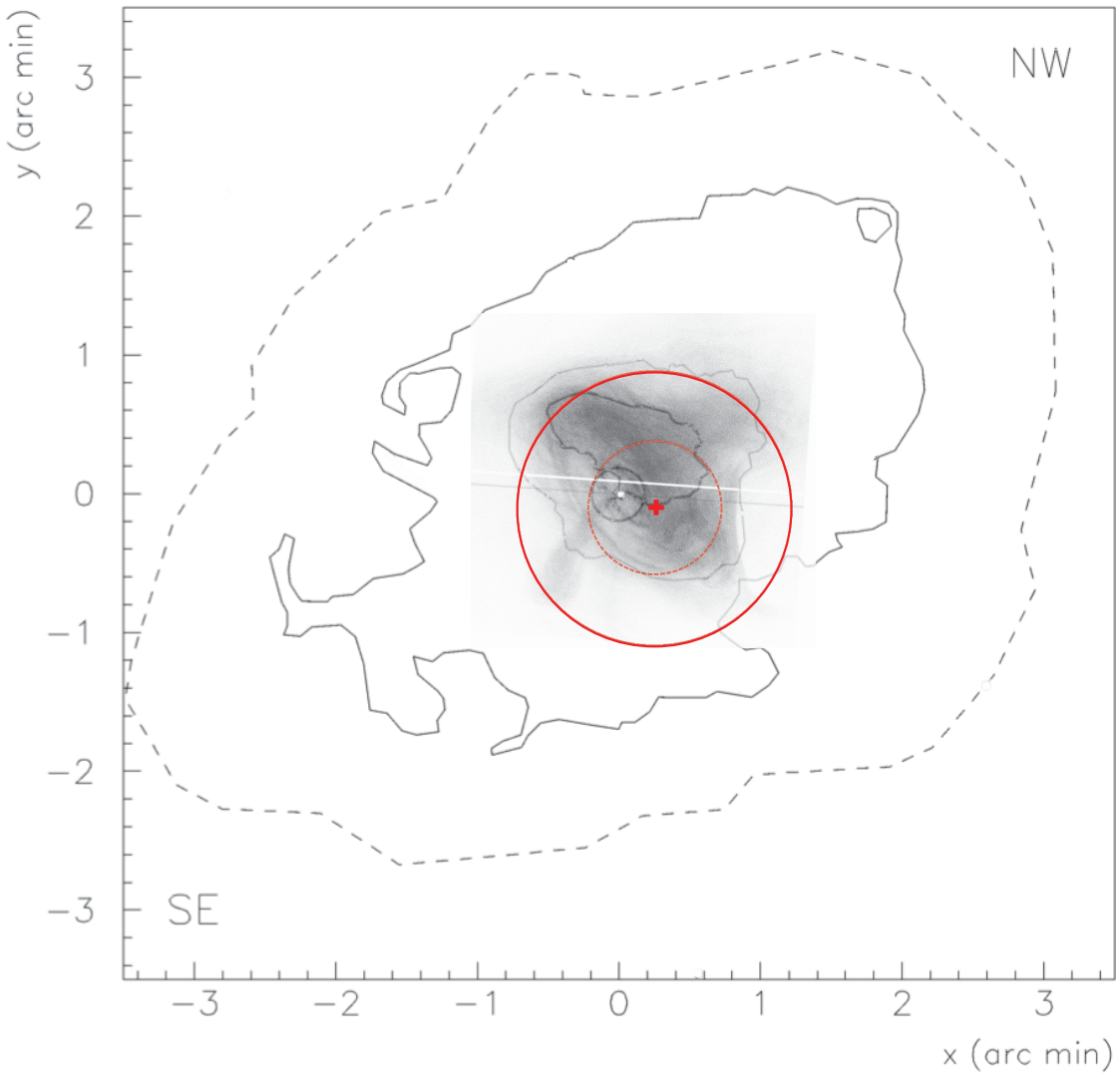

Fig. 5.8.: Best fit position and upper limit on the source size. The red cross marks the best fit position, its size corresponds to the statistical errors on the position. The dashed red circle depicts the pointing precision. The outer red circle represents the 2σ U.L. on the Crab Nebula size derived in this work. The figures are overlaid on a Chandra X-ray skymap and embedded in a schematic representation of the whole nebula, which was adapted from Hillas et al. (1998). The innermost contours mark the 70% (darker) and 30% (lighter) flux level of the peak soft X-ray emission. The outer solid line encloses 35% of the peak flux of 20 cm radio emission, and the dashed outer contours are the approximate outer boundary of radio emission according to Hillas et al. (1998).

6. Search for Extended Emission around AGN

About 50 AGN with redshifts up to $z = 0.6$ have been detected at TeV energies so far. Because of the large distances, the primary emission from most AGN is expected to be point-like given the current resolution of IACTs. However, secondary γ-ray emission formed in electromagnetic cascades may occur and cause extended emission around these sources. Two possible phenomena will be described and investigated here: So-called Pair Haloes (PH) and Magnetically Broadened Cascades (MBC). Both appear when multi-TeV gamma rays interact with the Extragalactic Background Light (EBL) and produce electron-positron pairs. These pairs, in turn, can Compton-upscatter Cosmic Microwave Background (CMB) photons, which can again pair-convert and so forth. Being electrically charged particles, the pairs are deflected by magnetic fields before they interact with the CMB. Since the mean free path lengths of the pair-producing photons are of the order of hundreds of Mpc (Aharonian et al. 1994), the magnetic field deflecting the electrons and positrons is not the local field of the emitting AGN, but the Extragalactic Magnetic Field (EGMF). The search for extended γ-ray emission around AGN is hence a good tool to indirectly measure the EGMF. Depending on the EGMF strength, the shape of the electron-positron distribution (and thereby of the γ-ray emission region) changes:

- **$\mathbf{B \geq 3.14 \times 10^{-6}\,G}$:** For EGMF strengths higher than $B = 3.14 \times 10^{-6}$G, no cascades develop since synchrotron energy losses dominate over IC losses. Following Eq. 2.18 in Blumenthal & Gould (1970), the energy loss-rate of an electron with energy E_e due to IC scattering in the Thomson regime is

$$\left(-\frac{dE_e}{dt}\right)_{IC} = \frac{4}{3}\sigma_T c\gamma^2 \epsilon_{iso} \tag{6.1}$$

  with $\gamma = \frac{E_e}{mc^2}$. The Thomson cross-section for an electron is $\sigma_T = 6.65 \cdot 10^{-25}\mathrm{cm}^2$, and the energy density of the target photon field (i.e. the CMB) is $\epsilon_{iso} = 0.26\mathrm{eV/cm}^3$. For an electron with an energy of 3 TeV, $\gamma = 5.9 \cdot 10^6$ and hence $-dE/dt = 2.4 \cdot 10^{-10}\,\mathrm{GeV\,s}^{-1}$.

  The energy loss due to synchrotron radiation is calculated according to Eq. 2.21 in Blumenthal & Gould (1970):

$$\left(-\frac{dE_e}{dt}\right)_{synch} = \frac{4}{3}\sigma_T c\gamma^2 \frac{B^2}{2\mu_0}, \tag{6.2}$$

  resulting in $-\frac{dE}{dt} = 2.3 \cdot 10^{-11}\mathrm{GeV/s}$. Using these equations, the equilibrium between the loss rates is found at magnetic field strengths of $3.2 \cdot 10^{-7}$ G. Below 10^{-7} G, the electrons loose their energy mainly in IC processes, which are of interest for the generation of cascades.

- $\mathbf{10^{-12}\,G < B < 10^{-7}\,G}$: If the EGMF strength B is between 10^{-12} and 10^{-7} G, the gyroradius of the electrons and positrons, given by

$$r_g \approx \left[\frac{E}{\mathrm{TeV}}\right]\left[\frac{B}{10^{-9}\mathrm{G}}\right]^{-1}\ \mathrm{pc}, \tag{6.3}$$

is smaller than the mean free path length limited by IC interactions,

$$\lambda_e \approx 10 \cdot \left[\frac{E}{100\mathrm{TeV}}\right]^{0.5} \cdot \left[\frac{B}{10^{-9}\mathrm{G}}\right]^{-0.5}\ \mathrm{kpc}, \tag{6.4}$$

see Aharonian et al. (1994). For example, for electrons with an energy of 3 TeV and a B-field strength of 10^{-10} G, these numbers compare as $\lambda_e \approx 5.5$ kpc and $r_g \approx 0.3$ kpc. Therefore, the pairs isotropise around the source, forming a pair halo. After this first step of the cascade, the electrons and positrons have still enough energy ($\sim$ half of the original photon energy E_0) to produce VHE γ-rays via IC scattering on the 2.7 K CMB. Given these numbers, the inverse-Compton peak of the secondary photons is at

$$E_1 \approx \frac{4}{3}(E_0/2m_ec^2)^2 \cdot (2.7kT_{CMB}) \approx \left[\frac{E_0}{40\ \mathrm{TeV}}\right]^2\ \mathrm{TeV}. \tag{6.5}$$

- $\mathbf{B \leq 10^{-14}\,G}$: In EGMF regimes below 10^{-14} G, the gyroradius of TeV electrons and positrons becomes larger than the mean free path length between IC interactions, e.g. for B = 10^{-15}G, $\lambda_e \approx 1.7$ Mpc and $r_g \approx 3$ Mpc for 3 TeV electrons. This means that the cascade propagates along the line of sight and is only slightly deflected by magnetic field interactions, hence the phenomenon is called a magnetically broadened cascade (MBC). Although both MBCs and PHs are expected to produce extended emission detectable at VHE, the different origin and resulting different spatial and spectral distributions require a separate treatment of the phenomena.

Due to their dependence on the magnetic field strength, the detection or exclusion of PH and MBC can probe very low EGMF values. These are of special interest in cosmology, since the primordial "seed" fields, that galactic fields are believed to have developed from via dynamo effect, may be extremely weak. The seed fields are expected to persist in voids outside galaxies and galaxy clusters. Such voids are believed to make up a significant part of the space volume (see, e.g., Kronberg 1994; Grasso & Rubinstein 2001). Their detection could provide a glimpse on early stages of the cosmological evolution, e.g. the inflationary epoch.
However, it is currently discussed to which amount the development of both PH and MBC could be suppressed by plasma instabilities. A substantial part of the energy of the first electron and positron pairs might be lost in the electrostatic turbulence, see Broderick et al. (2012); Schlickeiser et al. (2012). The debate about the rate of growth of such instabilities is still on-going (Miniati & Elyiv 2013), but in the newest simulations, an energy loss of less than ten percent of the cascade energy is predicted (Sironi & Giannios 2013).
In the following, characteristics and dependencies of PH and MBC are briefly summarized. Subsequently, the choice of three VHE-γ-ray sources for the search for these phenomena is explained. The analysis of the H.E.S.S. observations of these sources is presented in Sec. 6.3 and two methods to derive upper limits on extended emission are introduced in Sec. 6.4. Finally, the results are discussed in Sec. 6.5, also in the context of the publication H.E.S.S. Collaboration et al. (2014b).

6.1. Pair Haloes

The shape and intensity of pair-halo emission depend on a multitude of factors: While the exact magnetic field strength is unimportant for the size of the pair halo, the primary photon spectrum, the distance to the observer, the EBL and, for $z > 0.1$, its cosmological evolution influence the development of cascades. In addition, the energy range and field of view of the instrument limit what we can see of a pair halo since the highest energy secondary emission is concentrated close to the source, while particles with lower energies fill a larger volume. Eungwanichayapant & Aharonian (2009) studied these effects extensively using Monte Carlo simulations. According to their calculations, the angular shape at energies >10 GeV is dictated by the highest energy primary photons. Therefore, simulations with hard spectra up to 100 TeV yield almost the same results as a monoenergetic injection of 100 TeV particles, see Fig. 6.1. If the energy cutoff of a source lies below that value, the flux and maximal energy of cascade photons decrease accordingly.

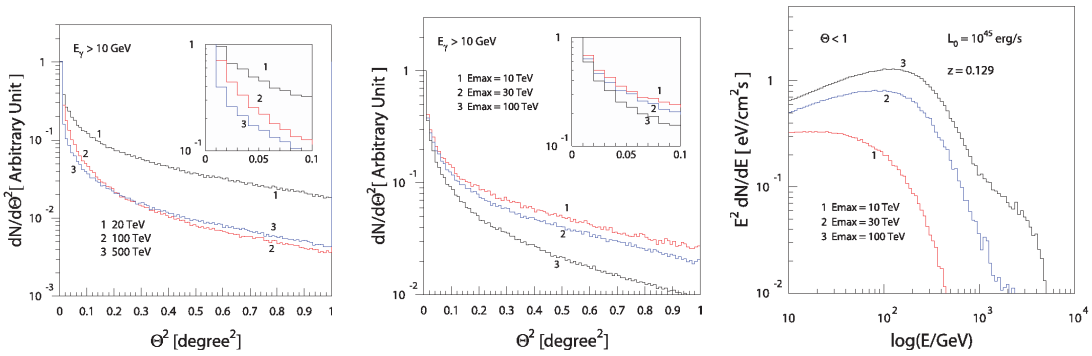

(a) (b) (c)

Fig. 6.1.: (a) Angular distributions of pair-halo photons with energies larger than 10 GeV for monoenergetic primary gamma rays with E = 20 TeV, E = 100 TeV and E = 500 TeV. (b) Angular distributions of pair halo photons simulated with power law injection spectra with an index of 1.5 and cutoff energies of E_{max} = 10 TeV,E_{max} = 30 TeV and E_{max} = 100 TeV. (c) Spectral energy distributions corresponding to the simulations with different injection spectra. Figures courtesy of Eungwanichayapant & Aharonian (2009).

The cross-sections of pair production and IC scattering depend strongly on the EBL and CMB levels. Since the energy densities of these background radiations are not constant over time, their flux at earlier epochs, i.e. at higher redshifts, shapes the pair halo emission around high-redshift AGN. The spectral shape and cosmological evolution of the CMB are comparatively well-known (see, e.g., Komatsu et al. 2009; Fixsen 2009; Battistelli et al. 2002; Noterdaeme et al. 2011): The energy density of the CMB decreases with time and its peak shifts to lower wavelengths in accordance with the established cosmological ΛCDM model, resulting in the current black-body spectrum with T_k =2.73 K. In the case of the EBL, however, neither its current energy density nor its evolution are determined equally well. Direct measurements can only give upper limits because of foreground contamination like the zodiacal light, galaxy counts provide lower limits, and the systematic errors on indirect measurements are large (H.E.S.S. Collaboration et al. (2013)), leaving a broad band of spectral models possible (for a broad overview of EBL measurements see, e.g., Gilmore et al. 2012, and references therein). The evolution of the EBL reflects the cosmological evolution of galaxies, stars and dust, which are modeled using assumptions and therefore bear some uncertainties. The models discussed in Eungwanichayapant &

Aharonian (2009) are Malkan & Stecker (1998) and Primack et al. (2001) and the EBL development with redshift is shown for the latter in Fig. 6.2. For multi-TeV photons, the EBL range of 1 - 10 μm is decisive for the development of a pair halo.
Since electrons are accumulated in the pair halo over thousands of years, the detection or upper limits on extended emission can be used to set limits on the past γ-ray output from an AGN on such time scales. Also, limits on the PH γ-ray energy flux of an AGN can be converted into limits on the accumulated electron energy density in its vicinity.

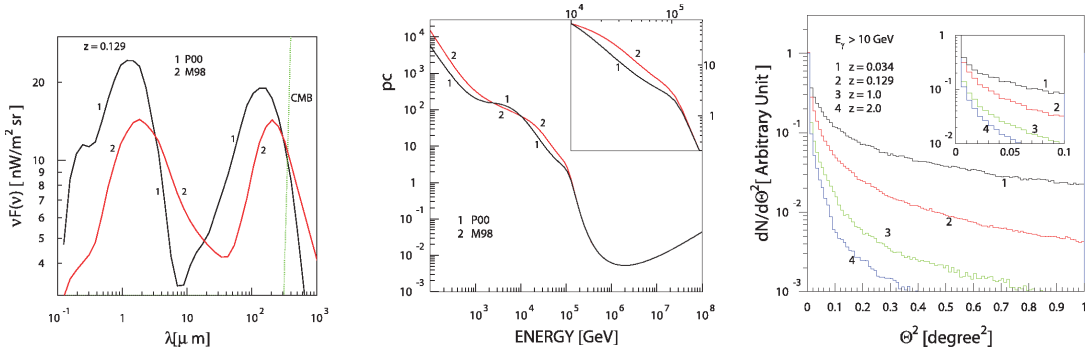

(a) (b) (c)

Fig. 6.2.: (a) Fluxes of the EBL according to the models by Malkan & Stecker (1998) (M98) and Primack et al. (2001) (P00). (b) Mean free path length for gamma rays assuming these models. (c) Expected angular distribution of a pair halo at different redshifts assuming the Primack et al. (2001) EBL model . Figures taken from Eungwanichayapant & Aharonian (2009).

6.2. Magnetically Broadened Cascades

The radial distribution of γ-rays in a MBC depends on the EGMF strength - the stronger the magnetic field, the broader the MBC becomes. To estimate the observable size, the distance of the AGN to the observer is a crucial parameter. On the one hand, the broadening is below typical PSF sizes of IACT if the AGN is closer than $z = 0.2$ and the EGMF is weaker than 10^{-16}. On the other hand, broader cascades do not necessarily result in a better detectability since the overall flux of the cascade remains the same. In addition, the radial distribution of the MBC emission is expected to depend weakly on the orientation and opening angle of the AGN jet (Aharonian et al. 1994). Assuming that the observer is not too close to the "edge" of the jet, the observable differences are negligible for BL Lac objects. Furthermore, the coherence length scale λ_B, i.e. the typical size of regions with approximately the same EGMF strength, is of some importance in the modelling of MBCs. If it is larger than the cooling length of the cascade electrons, the EGMF strength can be assumed as a constant. However, if it is shorter, the models become more complicated and the actual value of λ_B becomes important.
As is the case with PH, the MBC accumulates particles and therefore reflects the time-integrated flux of primary particles. Also, as for PH, the EBL and its evolution are of importance when predicting MBC fluxes. Since a cascade is affected by EBL absorption differently than direct γ-rays, the existence of MBCs can be probed by the combined evaluation of energy spectra in HE and VHE γ-rays. A simulation of the attenuation of the original source spectrum by the EBL and the influence of a (unbroadened) cascade on

the spectral energy distribution between 1 GeV and 30 TeV is shown in Fig. 6.3, for the source PKS 2155−304. It illustrates that the secondary radiation (i.e. the MBC) can even dominate over the primary component in the GeV energy range, if the primary spectrum of γ-rays is hard and extends beyond 10 TeV. In the simulation, the EBL model by Primack et al. (2001) was employed. For a more detailed discussion on that topic and upper limits derived by employing that method, the reader is referred to Taylor et al. (2011a).
MBC are of great interest, because limits on the EGMF strength can be derived from the fraction of secondary to primary photons. As mentioned above, although higher field strengths are expected, "voids" on 100 Mpc scales with values as low as 10^{-17} G cannot be excluded (Miniati & Bell 2011; Durrer & Neronov 2013). The search for MBCs in both spectra and angular distributions of blazars is used to probe this cosmological concept.

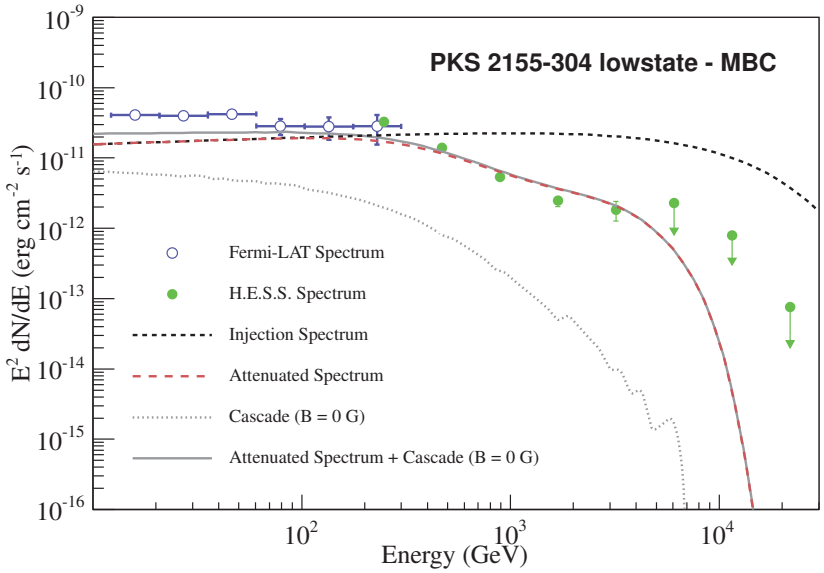

Fig. 6.3.: The spectral energy distribution of PKS 2155−304, including *Fermi* data (blue empty circles) and the H.E.S.S. results (green solid circles). The dotted grey line depicts the expected spectral energy distribution of a cascade, assuming the EGMF strength is 0 G. The solid grey line is an addition of the cascade component to the primary γ-ray emission after EBL absorption (dashed red line). Figure taken from H.E.S.S. Collaboration et al. (2014b).

6.3. Data sets and analyses

Although $\sim$ 20 AGN are detected by H.E.S.S. , only few of them are suitable for the search of extended emission. Most importantly, there is a preferred distance for the observation of both PH and MBC with H.E.S.S. , which is the range of hundreds of Mpc to one Gpc ($z \sim$0.1 – 0.4). The near limit for PHs originates in the field of view of the H.E.S.S. experiment: If the source was closer than z = 0.1, the PH would fill the whole 5° field of view. For MBCs, the near limit stems from the fact that cascades only become visible in γ-rays after few pair production lengths. For γ-rays with energies of a few TeV, a typical pair production length is 10 Mpc. The far limit is set by the expected reduction of the secondary emission flux to a non-detectable level in both cases. Of the nine H.E.S.S. sources

Table 6.1.: Summary of the H.E.S.S. analysis results for 1ES 1101−232, 1ES 0229+200 and PKS 2155−304. The live-time, number of ON and OFF source events, γ-ray excess and significance (σ), mean zenith angle (Z_{mean}), mean offset (ψ_{mean}) and the photon index Γ for each source are listed.

Source Name	T_{live} (hours)	N_{ON}	N_{OFF}	Excess	σ	Z_{mean} (deg.)	ψ_{mean} (deg.)	Γ
1ES 1101−232	64.3	2170	19314	879	21.4	26	0.58	3.1
1ES 0229+200	93.6	1178	8633	458	14.9	47	0.56	2.6
PKS 2155−304	483	99589	40338	91464	92179	515.6	0.53	3.4

fitting the distance criterion, only three have fluxes larger than 1% of the Crab Nebula flux: PKS 2155−304, 1ES 1101−232 and 1ES 0229+200. 1ES 1101−232 and 1ES 0229+200 are both BL Lac objects first detected with H.E.S.S. in 2004 (Aharonian et al. 2007c,a). They are located at redshifts of $z = 0.186$ and $z = 0.140$ and their average fluxes are 1.8% and 2% of the Crab Nebula flux, respectively. The redshift of PKS 2155−304 is $z = 0.117$. The spectra of all three of the sources are consistent with a power-law model with a cutoff at multi-TeV. The assumption of multi-TeV photon injection is crucial because only then cascades detectable with H.E.S.S. can develop.
In the scope of this thesis, the paper H.E.S.S. Collaboration et al. (2014b) was published, which consists of the search for extended emission around these three objects. Although the methods employed for that publication were developed and the original analyses were performed before the start of this thesis, the cross-check analysis, final checks and writing of the publication were part of this work. In H.E.S.S. Collaboration et al. (2014b), the analyses were performed with a Hillas-type reconstruction (H.E.S.S. analysis package, version 10-06) on data that were calibrated independently. Here, a re-analysis of the three sources with the *Model Analysis* in Std configuration is presented. The *Model Analysis* PSF is smaller and it was calibrated on the flare of PKS 2155−304 in 2006, as described in Chap. 5. In addition, the number of observation runs on 1ES 0229−200 and PKS 2155−304 increased since more data fulfilling the 'good quality' criterion has been taken in the meantime.
As in the chapters before, only observation runs taken with four telescopes were used for the analyses. For comparability with H.E.S.S. Collaboration et al. (2014b), an analysis region with a radius of $\sqrt{0.22}^{\circ}$ was chosen and the *Reflected Region* method was used for background determination. The flare of PKS 2155−304 that took place in 2006 was excluded from the sample, since the fraction of events originating in extended emission must be extremely low in that period, see 4.4. A summary of the analysis results is given in Table 6.1.

6.4. Methods

Although extended emission around AGN was searched for with various VHE instruments, until now only simple geometrical models of the expected emission were compared to the observational data in order to derive upper limits on the flux. The first studies were conducted on Mkn 501 by the HEGRA collaboration (Aharonian et al. 2001), resulting in an upper limit of (5−10)% of the Crab Nebula flux at energies $\geq$ 1TeV for an angular distance of 0.5° to 1° from the source. A similar approach was used by the MAGIC collaboration to investigate the angular distribution of γ-rays around Mkn 501 and Mkn 421 with a

significantly lower energy threshold of 300 GeV (Aleksić et al. 2010). The upper limits on the flux were found to be $< 4\%$ and $< 5\%$ of the Crab Nebula flux for extended emission around Mkn 421 and Mkn 501, respectively. The results on Mkn 501 were also used to give a qualitative estimate of the EGMF strength, excluding magnetic field strengths between $4 \cdot 10^{-15}$ G and $1.3 \cdot 10^{-14}$ G. Both sources are not the ideal candidates for the search of extended emission, since their distances are rather small (z = 0.034 for Mkn 501 and z = 0.031 for Mkn 421). Therefore, a pair halo would probably be larger than the entire field of view of the MAGIC telescopes, which is only 3.5°, making it difficult to distinguish from background.
In the GeV energy band, *Fermi*-LAT data were used to search for extended emission around AGN. There are three publications on the topic, all of them using stacked data of large AGN samples. In the first study, containing 11 months of *Fermi* data, evidence for MBCs has been claimed (Ando & Kusenko 2010), however, it was contradicted by Neronov et al. (2011). The apparent extension of the AGN must have been an effect of systematic problems with the LAT PSF, and it vanished in the later analysis after a new PSF model was introduced (Ackermann et al. 2013a), which underlines the importance of a good knowledge of the PSF systematics. In Ackermann et al. (2013a), 115 BL Lac-type AGN were divided into high- (z > 0.5) and low-redshift (z < 0.5) blazars, and a search for disk- and Gaussian-shaped extended emission was conducted in the stacked angular data. Different radii of a hypothetical pair halo between 0.1° and 1° were tested, resulting in no evidence for any extension. For 1ES 0229+200 and 1ES 0347-121, two objects with spectra extending to TeV energies, upper limits on the energy flux assuming these radii were given between 1 and 100 GeV. Most recently, evidence for pair halos in the stacked data of 24 low-redshift blazars was found with a 6σ significance in the few-GeV range by Chen et al. (2014). In that study, the PSF was compared to the angular distribution of pulsars and flat spectrum radio quasars (FSRQs), which appear perfectly point-like.
In all these publications, a model parameter reflecting the angular size was varied and the derived upper limits strongly depend on that parameter. For the methods presented in the following, the shape and angular size of the extended emission are either not needed at all or fixed by model predictions, therefore the upper limits on the flux are independent of such assumptions. The two methods used to give upper limits on PH fluxes are referred to as model-independent and model-dependent method from here on.

6.4.1. Model independent method

The model independent method basically consists of a comparison of the angular distribution of the H.E.S.S. PSF and the observed source emission. In order to derive a flux upper limit, the residual number of events after point source subtraction was calculated. A range of $0.125\,\mathrm{deg}^2 < \theta^2 < 0.2\,\mathrm{deg}^2$ was chosen to obtain this number, since it is predicted that a pair halo would dominate over the PSF in this region. For comparison, r_{68} of the *Model Analysis* MC PSF produced for the PKS 2155−304 data set is only $\sim 0.006\,\mathrm{deg}^2$ in θ^2 representation. In Fig. 6.4, the θ^2 range is visualized. The lower value was chosen according to the standard selection cut for point-like sources in the H.E.S.S. analysis package (HAP) analysis. The upper limit on the number of residual events is calculated as described by the confidence interval method in Feldman & Cousins (1998). Differential flux limits were obtained by dividing the maximum number of events compatible with the measurement at a 99% C.L. by the exposure of the data set for assumed spectral indices of 1.5 and 2.5.

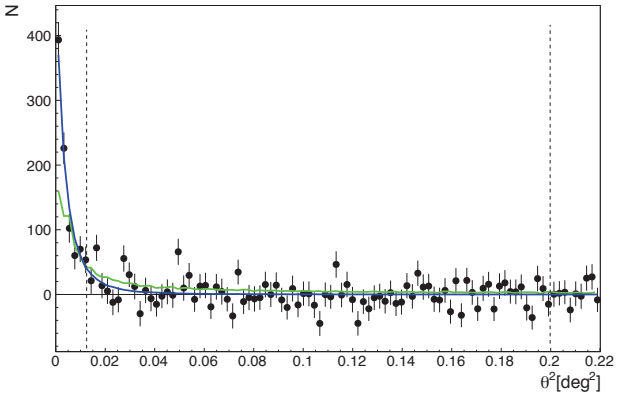

(a)

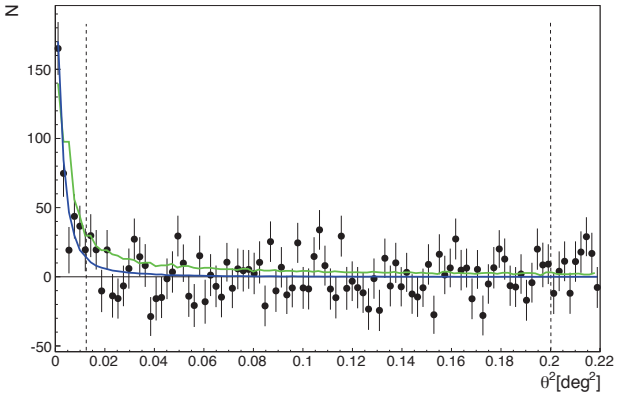

(b)

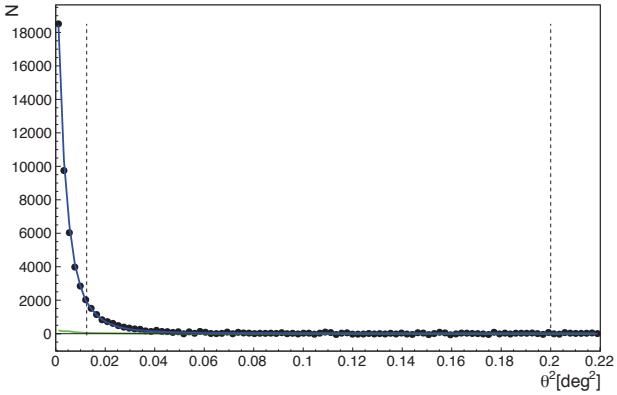

(c)

Fig. 6.4.: Angular distribution of excess events of (a) 1ES 1101−232, (b) 1ES 0229+200 and (c) PKS 2155−304. Data are shown as filled black circles, while the MC PSF is depicted as the blue line and the maximum allowed model dependent PH component as the green line. The angular PH distributions shown here were calculated with the Primack et al. (2001) EBL model.

These values represent a broader range of possibilities for the spectral index of the cascade emission, which is expected to follow an index of $\Gamma \sim 2$ at the high-energy end. The exact shape of the spectral energy distribution (SED) of a PH does, however, strongly depend on the cutoff energy of the injection spectrum. The resulting numbers are listed in Table 6.2 (A). Relative to the flux of central source, the U.L. on PKS 2155−304 are the most restricting, amounting for at most 4% of the events. Compared to H.E.S.S. Collaboration et al. (2014b), the U.L. calculated here are up to a factor of 10 lower. This result is expected due to the higher event statistics and hence smaller relative Poissonian error in the PH extraction region and the much smaller PSF size (factor ∼0.7). The model independent upper limits are very robust concerning systematic errors on the PSF size: If the PSF was broader, the U.L. would decrease. The opposite case, i.e. a true PSF smaller than the MC PSF, was tested by using the un-calibrated PSF of the *Model Analysis*. As described in Chap. 5, the broadened PSF differs from the simulated PSF by a Gaussian width of $\sigma \sim 0.02^\circ$, which corresponds roughly to the 2σ systematic error. In the θ^2 range of the model-independent calculations, the resulting upper limits on the flux differ by less than 1%, see Table 6.2 (B).

Table 6.2.: Pair halo flux upper limits for 1ES 1101−232, 1ES 0229+200, and PKS 2155−304 at a 99% C.L. calculated with the *Model Analysis* for energies >0.2 TeV for PKS 2155−304 and 1ES 1101−232, and >0.5 TeV for 1ES 0229+200. The upper three rows (A) were calculated with the calibrated PSF, while the lower three rows (B) were calculated with an artificially narrow PSF. All values are limits on the differential flux at 1 TeV given in units of $10^{-12}\,\mathrm{TeV}^{-1}\,\mathrm{cm}^{-2}\,\mathrm{s}^{-1}$.

		Model dependent				Model independent	
	Source name	Franceschini EBL		Primack EBL			
		$\Gamma = 1.5$	$\Gamma = 2.5$	$\Gamma = 1.5$	$\Gamma = 2.5$	$\Gamma = 1.5$	$\Gamma = 2.5$
A	1ES 1101−232	0.15	0.06	0.15	0.07	0.13	0.06
	1ES 0229+200	0.10	0.14	0.14	0.10	0.07	0.12
	PKS 2155−304	0.09	0.04	0.06	0.03	0.15	0.07
B	1ES 1101−232	0.14	0.06	0.14	0.06	0.13	0.06
	1ES 0229+200	0.07	0.13	0.07	0.10	0.07	0.12
	PKS 2155−304	0.19	0.05	0.12	0.05	0.15	0.07

6.4.2. Model dependent method

Search for Pair Haloes

As described above, detailed simulations of the formation of PH under different conditions were performed in Eungwanichayapant & Aharonian (2009). For the model dependent flux upper limits, the angular distribution the authors obtained with the Primack et al. (2001) EBL model for $z = 0.13$ and $\mathrm{E}_\gamma > 100\,\mathrm{GeV}$, which best suits the data at hand, was taken from Fig. 6 of Eungwanichayapant & Aharonian (2009) . It follows a profile of $dN\,/\,d\theta \propto \theta^{-5/3}$ (see Fig. 6.1). In H.E.S.S. Collaboration et al. (2014b), an angular model for a pair halo assuming the Franceschini et al. (2008) EBL model was generated additionally. The Franceschini et al. (2008) and Primack et al. (2001) models each represent one of the highest and lowest EBL predictions in the (1-10) μm range relevant for PH at TeV energies, hence they bound the uncertainities on the pair halo models. The

angular distribution for the Franceschini et al. (2008) EBL model is a broadened version of the angular distribution obtained with the Primack et al. (2001) model, accounting for the 40% higher EBL flux. In general, the effect of different EBL models cannot be described by such a simple relation. However, it is adequate for the very narrow range of relevant energies and redshifts discussed here (Eungwenichayapant & Aharonian, private communication, Sep 2013). Since the effect of the difference between the redshift of the angular model and the redshifts of the analysed sources is smaller than the effect of different EBL models, it is neglected subsequently. The spatial model of the pair halo was convolved with the PSF to create "halo functions": $N(\theta^2) = N(\theta^2)_{PSF} + N(\theta^2)_{PH}$. These functions were used to fit the angular distributions of the three sources, the normalisation of the PSF being the only free parameter. The number of pair-halo events was increased until the fit probability decreased to $p< 0.01$. The differential flux limit was determined by dividing the maximum possible number of halo events by the exposure for spectral indices of 1.5 and 2.5, respectively. While this procedure worked for all three of the chosen sources in H.E.S.S. Collaboration et al. (2014b), fitting the PKS 2155−304 data set with a point-like source model is highly rejected in the *Model Analysis* used here. As presented in Chap. 4, the apparent size of that source is $\sigma_a = (0.021 \pm 0.003)$ deg, employing a Gaussian source model. Therefore, a scan of the fit probability depending on the number of added PH events was conducted. The highest probability was found for ∼1100 events in PH shape, however, that probability was only 0.08%, indicating that although the θ^2 distribution of the source does not match the MC PSF, the mismatch cannot completely be explained by a pair halo. The most probable number of PH events is visualised in Fig. 6.4(c), together with the θ^2 distribution of PKS 2155−304 and the according MC PSF. The corresponding fluxes assuming spectral indices of 1.5 and 2.5 are listed in Table 6.2. For the two other sources, the lower event statistics allow for a broader spectrum of compatible shapes. However, the U.L. calculated with the model dependent method are again much lower than what was found in H.E.S.S. Collaboration et al. (2014b). The maximum allowed PH components at a 99% C.L. are depicted in Fig. 6.4(a) and Fig. 6.4(b). The resulting upper limits on the flux are listed in Table 6.2 (A).
Systematic errors on the PSF play a bigger role in the model dependent method than in the model independent one. Again, if the MC PSF was small compared to the true PSF, a higher fraction of events would be compatible with the PH model, thus the U.L claimed in Table 6.2 would be a conservative estimate. The case of a too broad MC PSF was tested with the un-calibrated *Model Analysis* PSF. For PKS 2155−304, even small fractions of a pair halo component are more strongly rejected if a narrower PSF is used. However, the method is very sensitive not only to the PSF width, but also to its shape. To calculate more conservative upper limits, the PH model was convolved with a single Gaussian with a width of only 0.03°, corresponding to the width of the PSF after subtracting the 3σ systematic errors as found in Chapter 4. With that convolution, higher PH event numbers are compatible with the measurement of PKS 2155−304, while the numbers for the 1ES objects are the same or lower, see Table 6.2 (B). The same procedure was tested with a Gaussian width of $\sigma = 0.07^\circ$, i.e. the systematic errors were added to widen the PSF. The convolved PH shape was added to a widened PSF. As expected, the limits obtained in that way are lower and are therefore not listed here.

Search for Magnetically Broadened Cascades

The model-dependent method was also employed to calculate U.L. on the fraction of MBC events. Instead of the angular model of a pair halo, the expected angular distributions of MBCs for different magnetic field strengths were simulated for each source. The models,

which were produced for H.E.S.S. Collaboration et al. (2014b), were convolved with the MC PSF obtained from the analyses in this thesis and added to the expected point source emission (i.e., the MC PSF). For the MBC simulations, a 1 Mpc coherence length was adopted, although larger values were discussed in Durrer & Neronov (2013).
For each magnetic field and for both EBL models, an "MBC function" $N(\theta^2) = N(\theta^2)_{PSF} + N(\theta^2)_{MBC}$ was created. Again, the point-soure fraction was used as a free parameter in the fit while the number of MBC events was increased step by step. The maximum allowed number of MBC events (on a 99% C.L.) was divided by the overall excess to obtain the cascade fraction. By comparing these fractions to model predictions, which were calculated for H.E.S.S. Collaboration et al. (2014b) for each of the three sources, a range of EGMF strengths was excluded.

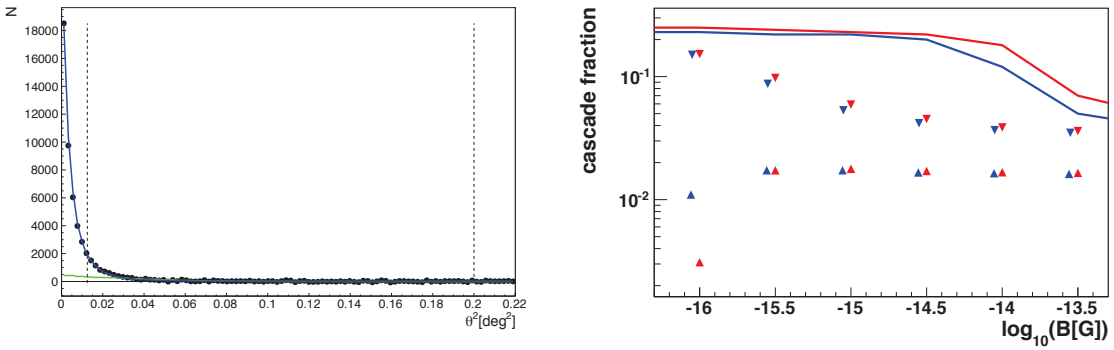

(a) (b)

Fig. 6.5.: (a) Maximum MBC fraction for PKS 2155−304, assuming an EGMF of $10^{-13.5}$G and the Franceschini et al. (2008) EBL model. The black points represent H.E.S.S. data, the blue and green lines are the MC PSF for the PKS 2155−304 data set and the angular model of the cascade, respectively. (b) EGMF constraints from PKS 2155−304. The expected fractions of MBC events depending on the EGMF strength, assuming the Franceschini et al. (2008) and the Primack et al. (2001) EBL models, are depicted as the blue and red lines, respectively. The upward-pointing triangles are the 99% C.L. U.L on the cascade fraction. Systematic errors on the PSF shape are neglected. The downward-pointing triangles depict the U.L. H.E.S.S. data at a 99% C.L.

Due to the rather low statistics, fits to the data sets of 1ES 1101−232 and 1ES 0229+200 did not constrain the cascade fraction enough to test the model predictions. The data set on PKS 2155−304, on the other hand, was used to exclude EGMF values of $10^{-15.5}$ G – 10^{-14} G in H.E.S.S. Collaboration et al. (2014b). Here, with the improved analysis and PSF, an even broader range of EGMF could be excluded. For all studied B-field strengths, ranging from 10^{-16} G to $10^{-13.5}$ G, the maximum fraction of MBC events compatible with the H.E.S.S. observations of PKS 2155−304 is below the predicted cascade fraction, see Fig 6.5. However, these limits depend strongly on the assumed PSF width and shape. In the case of an EGMF strength of 10^{-16} G, the U.L. drops by a factor 5 for the EBL model by Primack et al. (2001), which should be regarded with caution. For such low EGMF values, the MBC shape is very narrow, hence its compatibility with the measured data depends on the first few bins of the θ^2 histogram which are dominated by emission in PSF shape. As was done with the PH constraints, the MBC models were therefore convolved with Gaussians with a width $\sigma = 0.03°$ instead of the actual PSF to obtain more conservative upper limits, and the un-calibrated PSF was used in the fit. As shown

in Fig. 6.5, the resulting U.L are significantly higher, but still below the expected cascade fractions and the whole EGMF range can be excluded. Nevertheless, the limits derived from the PSF-convolved MBC shapes are shown to visualize the potential of the method and the importance of PSF systematics.

6.4.3. *Fermi*-LAT observations and analyses

In addition, observational data of the LAT instrument on the *Fermi* Gamma-ray Space Telescope was analysed in H.E.S.S. Collaboration et al. (2014b). Observations of the three sources taken between 4th August, 2008 and 1st March, 2013 were analysed with the LAT Science Tools package v9r23p1 (updated on 1st August 2011 to include newer PSFs) with the P7SOURCE_V6 post-launch instrument response function[1]. The analyses were performed with a standard event selection for sources outside the galactic plane and the standard procedure of fitting all sources published in Nolan et al. (2012) within a radius of 10° around the source of interest was applied. The energy range was restricted to 100 MeV –300 GeV to reduce uncertainties in the effective area. The energy range was split into logarithmically equal bins. Assuming a power law as spectral model, a fit of the normalisation was performed in each bin, while the power law index was fixed to $\Gamma = 2$. The morphology and spectrum are fitted simultaneously in the *Fermi* analysis. The PKS 2155−304 and 1ES 1101−232 were detected in the datasets with significances of $>100\sigma$ and 8.8σ, respectively, and the results of their spectral analyses are in agreement with the spectra published in (Nolan et al. 2012). 1ES 0229+200 was not detected in (Nolan et al. 2012) yet, but an analysis of the source was presented in Vovk et al. (2012). The results obtained in H.E.S.S. Collaboration et al. (2014b) are in agreement with that publication and the source was detected with a significance of 5.6σ. To search for a possible PH contribution, a spatial model $\propto \theta^{-5/3}$ was convolved with the *Fermi* PSF and added to the point-like source, similar to the model-dependent method employed with H.E.S.S. data. The newly obtained source model was fitted in the same manner as the point source before, i.e. all 2FGL sources within a radius of 10° were fitted simultaneously. Since the addition of a pair halo component did not increase the overall log-likelihood values for either source, upper limits on the maximum compatible PH fluxes in each energy bin were calculated (H.E.S.S. Collaboration et al. 2014b).

6.5. Discussion

Unlike what is typically expected, the model-independent limits on the 1ES objects are almost a factor two lower than the model-dependent ones. This result is caused by the low statistics for these two objects, that allow fitting almost the complete angular event distribution with a PH model. In addition, the model-independent upper limits are calculated for $\theta^2 > 0.0125\,\mathrm{deg}^2$, i.e. the solid angle is smaller and omits the region of the highest flux.

For PKS 2155−304, very strong model-dependent constraints were derived. A PH shape is clearly rejected down to fluxes of few per mille of the Crab Nebula flux, and this statement holds true taking the PSF systematics into account. Assuming the lower EBL fluxes predicted by the Franceschini et al. (2008) model, the extended emission is expected to be broader and is therefore constrained at an even higher level. Furthermore, *Fermi*-LAT data of the three sources were analysed in H.E.S.S. Collaboration et al. (2014b), yielding no significant emission shaped like the expected $\theta^{-5/3}$ profile. Nevertheless, a

[1] See http://fermi.gsfc.nasa.gov/ssc/data/ for public *Fermi* data and analysis software.

non-detection of pair haloes does not necessarily mean an exclusion of the EGMF range of 10^{-7} –10^{-12} G, since the extended emission could be very faint or fill up the entire field of view, rendering the background subtraction inaccurate.
Instead, the exclusion of an EGMF range is sensible under the assumption of MBCs. However, some uncertainties on the model predictions have to be kept in mind. The effect of the coherence length can be neglected if it is larger than the cooling length of the multi-TeV cascade electrons of relevance here, which is the case for, e.g., 3 TeV electrons in a magnetic field of 10^{-14} G. If λ_B is shorter than the cascade electron cooling length, the lower EGMF limit scales as $\lambda_B^{-1/2}$ according to Neronov et al. (2013). The bound on the EGMF presented here is compatible with the analytic estimates shown in Aleksić et al. (2010), which were also derived by assuming the non-detection of extended emission.
A general drawback of the model-dependent method is that upper limits become more constraining the more the shape of the expected extended emission deviates from the PSF. In the studies at hand, the PSF systematics were accounted for by assuming a Gaussian form of systematic errors in the angular distribution of MC simulations. If the systematic errors change the angular shape of the PSF in a different way, higher cascade fractions might be compatible with the data.

7. Summary and Outlook

The point spread function (PSF) is one of the essential characteristica of every imaging instrument. In γ-ray astronomy, the PSF depends on a multitude of factors, ranging from observational conditions to analysis cuts. A profound understanding of the PSF is required to facilitate the correct description of morphologies. Especially the investigation of structures that are smaller than the 68% containment radius, r_{68}, suffer from systematic errors on the PSF. In this work, the PSF of the H.E.S.S. experiment was systematically studied by employing MC simulations and observational data of point sources. A general mismatch between them was found, leading to an apparent extension of all sources. By examining different parameters, some possible causes of the mismatch were found. However, not all of the mismatch could be attributed to the effects that were found, hence the PSF generated from MC simulations was calibrated on a flare of the AGN PKS 2155−304, which is guaranteed to be a point source. With the calibrated PSF, the size of the Crab Nebula and extended emission around three AGN were probed.

No significant extension of the VHE emission region of the Crab Nebula has been found. With all three cut configurations used in this work, the angular event distribution is compatible with a point-source assumption given the systematic errors on the PSF. Considering only the statistical errors, the measurement constrains the source size to values below 0.02°. However, the systematic errors are of the same order of magnitude, hence a conservative U.L. of 0.034° at the 95% C.L. is given. In the current understanding of the IC emission process in the Crab Nebula, the size at TeV energies should at least display the size seen by the Chandra satellite, which corresponds to a Gaussian width of $\sim 0.01^\circ$ (Hillas et al. 1998). The upper limit found in this work is still far above that expectation and comparable to the limits found in Aharonian et al. (2000). As described in Aharonian et al. (2000), the limit approaches the sizes expected for hadronic production models as proposed as additional or alternative mechanisms by Atoyan & Aharonian (1996) and Bednarek & Protheroe (1997). According to these models, the VHE γ rays could be produced more or less throughout the nebula, which is $\sim 0.1^\circ$ in size. In addition, following Volpi et al. (2008), a measurable extension of the Crab Nebula, or at least the measurement of an asymmetry, seems within reach. According to the surface brightness maps generated for that publication, the jet axis should be elongated in VHE γ-rays. In this work, no evidence for such a structure was found.

The upper limit found in this work is one of the most restrictive of all published VHE constraints, and the precision of the systematics estimation is unprecendented. With the current generation of IACT experiments, substantial effort not only in understanding the PSF but also adjacent fields, like the spectral reconstruction, is required to improve the limit presented here.

In the search for pair halos and magnetically broadened cascades, no extended VHE γ-ray emission was found in the regions surrounding 1ES 1101−232, 1ES 0229+200 and PKS 2155−304. Flux upper limits constraining a possible pair halo or magnetically broadened cascade at the level of less than 0.5% of the Crab Nebula flux at above 1 TeV[1] were

[1] The integral flux of the Crab Nebula above 1 TeV is $(2.26 \pm 0.03) \times 10^{-11}$ cm^{-1} s^{-1}, see Aharonian et al. (2006a).

calculated independently of model predictions. Employing the model by Eungwanichayapant & Aharonian (2009), the maximum pair halo flux was derived for two different EBL models. While the model-dependent limits are not as constraining as the model-independent ones for the 1ES objects, a very strong model-dependent constraint was derived for PKS 2155−304.
Also the fluxes of MBCs for different magnetic field strengths are considerably constrained by the model-dependent analysis of PKS 2155−304. For the simulated coherence length of 1 Mpc, EGMF values in the range of $(0.1 - 10) \cdot 10^{-15}$ G are excluded for both EBL models at a 99% C.L. Assuming that the true H.E.S.S. PSF is not narrower than the MC PSF calibrated on the flare data set of PKS 2155−304, even the whole studied range of 10^{-16} G – 10^{-13} G can be excluded.
While the limits obtained in H.E.S.S. Collaboration et al. (2014b) are comparable to previously obtained values from other experiments, the limits calculated here with the *Model Analysis* mark a significant improvement for both PHs and MBCs. The detailed angular modeling developed for H.E.S.S. Collaboration et al. (2014b) is an important step forward in the search for pair halos and magnetically broadened cascades around AGN. Especially in the search for MBCs, the method offers a complementary probe to the constraints provided by the multi-wavelength SED method employed in Neronov & Vovk (2010), Dolag et al. (2011), Tavecchio et al. (2011) and Taylor et al. (2011b)) since it is independent of the variability timescale of the source.
The search for extended emission around AGN on Mpc scales is still ongoing. Only recently, the detection of pair halos in a stacked sample of 24 BL Lac objects at ∼1 GeV was claimed (Chen et al. 2014). With the angular profile found in that publication, the EGMF strength was estimated to be $\sim 10^{-17}$–10^{-15} G, a regime that would lead to MBC production in the energy range of H.E.S.S. With H.E.S.S. , the analysis could be improved by employing the HiRes cut configuration of the *Model Analysis*, that results in even smaller r_{68} than the Std cut configuration used here. A narrower PSF would allow us to probe the region closer to the point source, which is also expected to provide a higher cascade flux. Especially for the search for MBCs that develop in magnetic field strengths below 10^{-15} G a better angular resolution is necessary. However, since the observations of the 1ES objects barely provide enough statistics for studies with standard (Std) cuts, only extremely luminous or well-observed objects like PKS 2155−304 are suited for this study using HiRes cuts.

A better angular resolution is one of the goals of the next generation of IACT experiments. The *Cherenkov Telescope Array* (CTA) will be an international observatory consisting of two arrays of 50 – 100 telescopes, one in the northern an one in the southern hemisphere. Telescopes of three sizes will be combined to create an observable energy range of few tens of GeV up to more than 100 TeV, and the instrument is designed to be a factor 10 more sensitive than current generation IACTs.
The goal for the PSF size of CTA is $r_{68} \leq 0.03°$ above 1 TeV, see Acharya et al. (2013). In a Gaussian approximation, this corresponds to $\sigma_{PSF} = 0.02°$. The means of improvement are a higher efficiency of Cherenkov photon detection due to the dense spacing of telescopes in the core region of the array and PMTs with higher quantum efficiencies (≤35% compared to 25% with H.E.S.S.). Besides the traditional Davies-Cotton design, Schwarzschild-Couder dual-mirror designs are tested. The dual-mirror designs would allow for more finely pixelated cameras, which could significantly improve the PSF (Hofmann 2006). Since, according to Acharya et al. (2013), a factor of 4–5 compared to current experiments

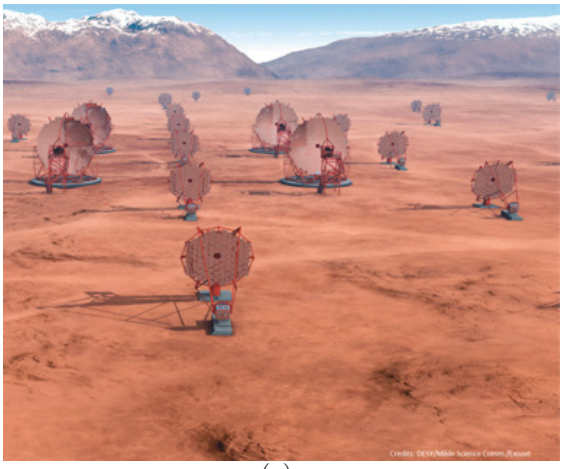

(a)

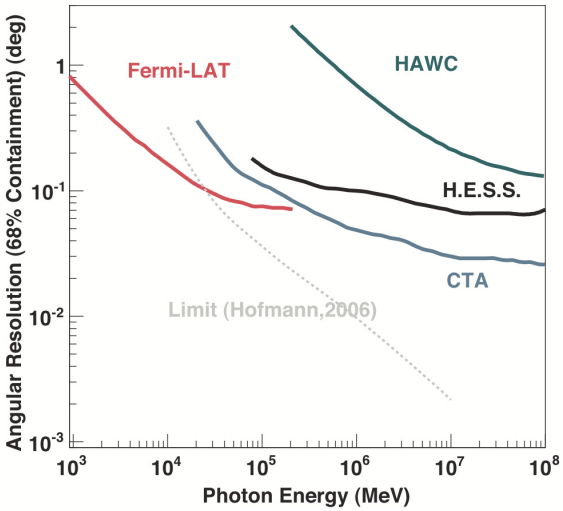

(b)

Fig. 7.1.: (a) Simulated view on a future CTA site. Image taken from https://portal.cta-observatory.org. (b) Angular resolution of CTA and some current experiments, courtesy of Funk & Hinton (2013). The grey dotted curve is the lower limit on the PSF size found by Hofmann (2006), which was also shown in Fig. 4.2.

is aimed for, a value of r_{68} of 0.03° seems to be outdated or quite pessimistic. In Fig. 7.1, the angular resolution of current experiments and CTA is compared. The curve shown for H.E.S.S. is clearly not representative for the newest analysis methods. With the *Model Analysis* in HiRes cut configuration, r_{68} as low as 0.045° at 1 TeV can already be reached with H.E.S.S. Hence, a PSF with $r_{68} = 0.01°$ does not seem unrealistic under optimal observation conditions, especially considering that reconstruction methods and analysis cuts are being developed and improved continuously. The desired PSF size is only a factor of two above the lower limit on the PSF size calculated by Hofmann (2006), which corresponds to r_{68} ∼0.01° at 1 TeV. However, Hofmann (2006) write that "the ultimate performance of instruments might still be better", knowing that the analysis with Hillas ellipses they used was not optimal.
With a smaller PSF size, systematic errors become even more important. The missing azimuth interpolation and insufficient MC statistics of H.E.S.S. can easily be avoided. However, to achieve a precise shower reconstruction also at low energies, the azimuth dependence probably needs to be included on the level of shower templates, unlike in the H.E.S.S. software. The pointing precision of CTA is supposed to be 5" per axis, corresponding to a Gaussian widening of the PSF of 0.002° . The errors on the muon efficiency are assumed to be 1/3 smaller for CTA than for H.E.S.S. , since the goal for the energy resolution is 10% for CTA compared to 15% for H.E.S.S. at 1 TeV. If the dependencies of the PSF were as they are for H.E.S.S. , the systematic errors would decrease to 0.006° , see Table 7.1. On an absolute scale, this is an improvement compared to H.E.S.S. , but in comparison to the desired r_{68} of CTA the systematic error is inacceptably large. The largest contribution stems from the errors on muon efficiency, but as mentioned in Sec. 4.6 at least the statistical errors could be reduced without much effort.

The size of the Crab Nebula at VHE will probably be measured with CTA. With the sensitivity of CTA, enough events for a statistically significant size fit will be collected within

Table 7.1.: Estimated systematic effects on the apparent source size for CTA. The errors are given as Gaussian widths in 10^{-2} deg. A PSF with $r_{68} = 0.03°$ was assumed.

effect	size	σ_{syst}
muon efficiency syst.	3%	0.43
muon efficiency stat.	2%	0.28
spectral index syst.	0.1	0.23
Pointing	5" per axis	0.20
1σ systematics		0.60

a few minutes, i.e. no pointing systematics will smear the sample. Assuming the remaining systematic error to be 0.0056° , as presented in Table 7.1, extensions above 0.017° will be detected with a 3σ significance. If, however, the Crab Nebula is less extended, the systematic errors will need to be reduced. It is seen as a fact that the TeV emission stems from outside the termination shock, hence the smallest possible extension, more or less in agreement with the current Crab Nebula models, is the radius of the "inner ring" in Fig. 5.2, which is ∼0.004° .
A localisation of the TeV emission of the Crab would allow for a more precise modelling of the object. The geometries of the photon and electron fields are important input parameters for spectral modelling as performed in Meyer et al. (2010), for example. It would therefore help to determine the nebular electron spectrum as well as the strength, or even the structure, of the magnetic field inside the nebula (see Meyer et al. (2010)).

The prospects for observing both extended halo emission and magnetically broadened cascades with CTA are promising. The field of view of CTA is planned to cover 8° for γ-rays with energies larger than 1 TeV, allowing to search for pair halos of nearby objects like Mkn 421 and Mkn 501 with a reliable background subtraction. To detect MBCs, distant objects (z >0.1) must be observed due to the larger electron cooling lengths in lower magnetic fields. In that case, with the improved sensitivity of CTA, much lower cascade fluxes will be probeable. Most importantly, the smaller PSF of CTA will allow to distinguish secondary emission much closer to the source, where the expected cascade flux is higher. If the EGMF strength is as low as derived in Chen et al. (2014), only a slight cascade broadening is expected, rendering a small PSF size even more important. Besides, the improved sensitivity of CTA will increase the number of detected VHE γ-ray sources. With a larger amount of AGN at different redshifts, stacking analyses will make sense, as is currently the case in the GeV energy range.
Another field where a small PSF at VHE will be advantageous are correlation studies with observations from other wavebands. For example, the measurement of the width of the γ-ray emitting shell would provide sensitive constraints on the acceleration mechanism in SNRs. Since the electrons leading to synchrotron radiation are of the same population as the ones responsible for IC emission, a strong correlation between these two energy bands is seen as evidence for leptonic scenarios of γ-ray production. Typically, the synchrotron wavelengths corresponding to TeV γ-rays are in the soft X-ray band, see Chapter 5. With satellites such as Chandra, the resolution at X-rays is much better than at VHE. Hence, a smaller PSF could contribute to solving the question of cosmic-ray acceleration in SNRs. Also, a smaller PSF facilitates smaller areas to derive spectra in. In objects like the SNR RXJ 1713.7−3946, the different spectra in different zones can be used to estimate the magnetic fields throughout the remnant (Berge 2014).

The PSF determines the minimum distance of two sources required to separate them. Source confusion, i.e. not being able to separate two sources, is a major problem in regions in the sky that are densly populated by VHE sources. For example, the attribution of PWNe candidates to pulsars, which densly populate the galactic plane, is one of the challenges in (H.E.S.S. Collaboration et al. 2015, in prep.). With CTA, source confusion will be an even more important topic, since a factor of 10 in detected sources is expected. A smaller PSF will allow for a better identification of objects that are close to each other.

In conclusion, the high angular resolution will be one of the key features for scientific progress with CTA. It will facilitate the study of new phenomena that are not accessible with current generation experiments.

A. The MeV γ-ray flare of the Crab Nebula in March 2013

In the scope of this thesis, a "Letter to the Editor" on H.E.S.S. observations of the Crab Nebula during a flare observed by the *Fermi* satellite was written and published (H.E.S.S. Collaboration et al. 2014c). Here, a summary of that publication is given.

A.1. Introduction

In March 2013, the Large Area Telescope (LAT) onboard the *Fermi* satellite measured fluxes from the direction of the Crab Nebula that were multiple times the average flux. The LAT detects γ-rays with energies of $\sim$20 MeV to $\sim$300 GeV, which covers the intersection of the synchrotron and the IC "bump" of the spectral energy distribution of the Crab Nebula (see Fig. 5.3. With data of the AGILE satellite, which observes a similar energy band, the high flux state was confirmed (Striani et al. 2013; Verrecchia et al. 2013). The flare lasted from MJD 56346 to 56370 and reached its peak flux on MJD 56357, see Fig. A.1. The *Fermi* satellite was set to a pointed target of opportunity observation mode and an Astronomer's Telegram was published on March 4th (Ojha et al. 2013)), strongly encouraging the observation of the Crab Nebula with other instruments. In Fig. A.1, the observation times of the experiments that followed that suggestion are depicted, among them H.E.S.S. The flare in March 2013 was the second brightest detected to that date. As

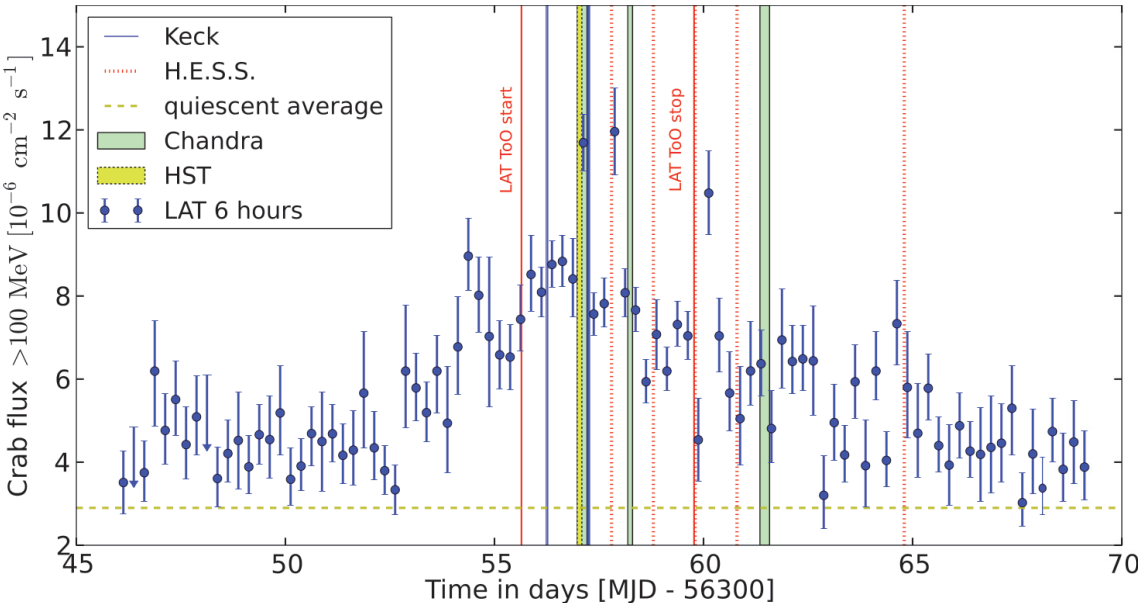

Fig. A.1.: Integral flux from the Crab measured by the *Fermi*-LAT, binned in 6-hour intervals. Figure from Mayer et al. (2013).

in previous flares (see, e.g., Buehler et al. (2012)), the lightcurve of the pulsar itself did not show any unusual behaviour and the high flux was attributed to the high-energy end of the

synchrotron component (Mayer et al. 2013). Likewise, the spectrum of the synchrotron component displayed a hardening with increasing flux level (Mayer et al. 2013).
Assuming common SSC models as presented in Chapter 5, the enhanced flux level could be caused either by changes in the magnetic and electric fields or by an increased production of electrons and positrons. No change in flux is expected in the IC component in the former case. In the latter case, the flare observed in the synchrotron energy range would cause a counterpart in the IC component. However, the enhancement in the VHE range is difficult to predict and depends on the model scenario. While a relative enhancement at the level of $\sim 10^{-2}$ times the average flux is expected at tens of TeV from, e.g., Fig. 8 in Lobanov et al. (2011), significantly smaller fluxes are expected at a few TeV (Bednarek & Idec 2011; Kohri et al. 2012). Since the systematic uncertainities of flux measurements with ground-based γ-ray experiments are typically 20%–30%, a significant detection of such a small change in flux would be improbable.
Nevertheless, the contemporaneous search for an IC component is required, given that the origin of the flares is poorly understood and a multitude of scenarios exists. In combination with observations of the flaring Crab Nebula at other wavelengths, ranging from infrared to X-rays (Mayer et al. 2013), coverage of the VHE band is needed to facilitate broadband modelling. Furthermore, the ARGO-YBJ group claimed nearly four times higher event rates than average over a period of eight days (Aielli et al. 2010) during a flare observed with *Fermi*-LAT (Buehler et al. 2010) and AGILE (Tavani et al. 2010) in September 2010. The ARGO-YBJ experiment detects air showers induced by γ-rays in the energy range of 0.5 –20 TeV, which overlaps with H.E.S.S.. An independent confirmation of the ARGO-YBJ measurement is still pending.

A.2. H.E.S.S. observations and dataset

During the flaring period in March 2013, the Crab Nebula was observed with H.E.S.S. from 2013 March 6 to March 10 (MJD 56358 - MJD 56365). Selecting only the runs that pass the quality criteria, a total dataset of 4.4 live-hours during five nights is obtained. The dates listed in Table A.1 were the only nights with good observation conditions contemporaneous with the target of opportunity observations with *Fermi*. At that time, the Crab Nebula was visible for H.E.S.S. only in the evenings shortly before setting, i.e. at very high zenith angles.

Table A.1.: Analysis results and for each night and the complete data set as given in H.E.S.S. Collaboration et al. (2014c). The live-time (T_{live}), mean zenith angle (Z_{mean}), the number of ON and OFF source events, the excess and its significance σ are reported. The normalisation at 1 (I_0) is given in units of ($10^{-11}\mathrm{cm}^{-2}\mathrm{s}^{-1}\mathrm{TeV}^{-1}$) and integral fluxes above 1 TeV and above 5 TeV in units of $10^{-11}\mathrm{cm}^{-2}\mathrm{s}^{-1}$.

Date 2013	T_{live} (s)	Z_{mean} (deg.)	N_{ON}	N_{OFF}	N_{exc}	σ	I_0 (1 TeV)	Index	Flux >1 TeV	Flux > 5 TeV
03-06	3181	54	202	498	175	20	3.5 ± 0.5	2.6 ± 0.1	1.89 ± 0.19	0.11 ± 0.03
03-07	3152	52	223	455	198	23	4.2 ± 0.4	2.8 ± 0.1	2.37 ± 0.21	0.08 ± 0.03
03-08	3155	53	184	460	159	19	3.5 ± 0.5	2.6 ± 0.1	2.24 ± 0.21	0.18 ± 0.04
03-09	4827	55	199	557	169	19	3.3 ± 0.5	2.7 ± 0.1	1.76 ± 0.18	0.12 ± 0.03
03-13	1596	54	62	173	53	11	5.2 ± 1.4	3.4 ± 0.3	2.06 ± 0.36	0.06 ± 0.05
full set	15911	54	870	2143	754	42	3.8 ± 0.2	2.7 ± 0.1	2.14 ± 0.10	0.12 ± 0.01

The dataset comprises three- and four-telescope data, taken with the H.E.S.S. Phase I array. The large telescope of Phase II was still in its commissioning phase, hence only

few observation runs could be taken with it and they were not included in H.E.S.S. Collaboration et al. (2014c). Unlike most other analyses presented in this work, the data were analysed with the H.E.S.S. Analysis Package[1] for shower reconstruction and a multivariate analysis (Ohm et al. 2009) for the rejection of hadronic background events. The analysis results for each night and for the complete sample are listed in Table A.1. They were obtained with the *Reflected Region* background method as presented in Sec. 3.4. The *Model Analysis* was only used as a cross-check. However, a difference of ∼20% between the flux normalisations resulting from the two analyses indicates a large systematic error. Hence, the numbers in Table A.1 are subject to estimated systematic errors of 30% for all fluxes and 0.1 for spectral indices.

A.3. Results

To compare the energy spectra of the flare data set with the energy spectrum during quiescence, the publication Aharonian et al. (2006b) was used as a reference. Motivated by the results in it, a simple power law and an exponential cut-off power law were used to model the energy distribution. However, due to the low statistics for E >10 TeV in the data set at hand, none of the models is significantly preferred. This is not a characteristic of this specific data set: A sample of 10 runs on the Crab Nebula from an earlier period, chosen to result in a similar telescope participation, did not allow for a discrimination between a power law model and a power law model with exponential cut-off, either. Hence, a power law model was adopted for all spectral fits, since it is numerically more stable. In Fig. A.2, the power law spectrum of the complete flare sample and the exponential cut-off power law spectrum taken from Aharonian et al. 2006b are shown. The energy range of that and the fits to the night-wise flare data is $[0.681 - 46.46]$ TeV. The lower bound is set by the relatively high energy threshold at the zenith angles of the observations. On the other hand, the inclination angle of the induced air showers at high zenith angles results in large effective areas, providing a high sensitivity for multi-TeV γ rays. All fit results and their statistical errors are compiled in Table A.1. The spectral analysis results of both night-wise and complete samples are compatible with Aharonian et al. (2006b), where an exponential cut-off power law was the best-fitting spectral model with $I_0(1\,\mathrm{TeV}) = (3.76 \pm 0.07) \cdot 10^{-11}\mathrm{cm}^{-2}\mathrm{s}^{-1}\mathrm{TeV}^{-1}$, $\Gamma_\gamma = 2.39 \pm 0.03$, $E_{\mathrm{cutoff}} = (14.3 \pm 2.1)$ TeV.
A χ^2-test was conducted to probe the agreement between the spectrum from Aharonian et al. (2006b) and the spectrum of the flare data set. The spectrum from Aharonian et al. (2006b) served as the null hypothesis for testing the photon spectrum above 1 TeV, 5 TeV and 10 TeV, resulting in χ^2/ndf values of 32.6/31, 15.7/14 and 5.0/7, respectively. These values indicate no significant difference in the spectra, although the optimistic assumption of cancelling systematics was made. Considering the low statistics in the last bin of the spectrum, a Likelihood Profile was calculated additionally. For the four ON events and one OFF event in that bin, the method described in Rolke et al. (2005) was followed. It results in a deviation of the last spectrum point from the expected flux according to Aharonian et al. (2006b) at a level of about 2.5 σ. The deviation is not significant, albeit neither systematic uncertainties nor the statistical uncertainties on the spectrum from Aharonian et al. (2006b) were included.
Since the highest flux enhancement accompanying an MeV-flare is expected at tens of TeV (Lobanov et al. 2011), flux variations above different energy thresholds were searched for. For the night-wise lightcurves, integral fluxes above 1 TeV and 5 TeV were calculated (see Fig. A.3). Higher energy thresholds were tested but are non-restrictive

[1] HAP version hap-12-03-pl02

due to low statistics. Fits of constants to the night-wise flux measurements result in $(2.0\pm0.1)\cdot 10^{-11}\mathrm{cm}^{-2}\mathrm{s}^{-1}$ with $\chi^2/\mathrm{ndf} = 6.1/4$ and $(0.11\pm0.1)\cdot 10^{-11}\mathrm{cm}^{-2}\mathrm{s}^{-1}$ with $\chi^2/\mathrm{ndf} = 1.2/4$ for an energy threshold of 1 TeV and 5 TeV, respectively. Within 2σ statistical errors, they are consistent with the the integral fluxes of the spectrum published in Aharonian et al. (2006b), which are $(2.26\pm0.08)\cdot 10^{-11}\mathrm{cm}^{-2}\mathrm{s}^{-1}$ and $(0.14\pm0.01)\cdot 10^{-11}\mathrm{cm}^{-2}\mathrm{s}^{-1}$, respectively.

The highest flux level in the March 2013 flaring period (Mayer et al. 2013) was detected by *Fermi*-LAT on MJD 56358, which is coincident with the first night of H.E.S.S. observations. For that night, upper limits on an enhancement of integral fluxes above 1 TeV and above 5 TeV were calculated separately. To compare the flux level in this publication with the one found in Aharonian et al. (2006b), the two flux values F_{2006} and F_{2013} were determined by integration of the fitted spectral functions. This method is preferred to event-number based upper limit calculations, since it takes the different energy migrations and efficiencies of the two analyses correctly into account. No significant deviation of F_{2013} from F_{2006} is found, and $F_{2006} > F_{2013}$. Hence, a conservative 95% C.L. upper limit is determined as $F_{2006} + 2\sigma$, where σ comprises the quadratically added statistical and systematic errors.

The upper limit on an enhancement of the integral flux above 1 TeV for the first night, calculated with this method, is $3.66 \cdot 10^{-11}\mathrm{cm}^{-2}\mathrm{s}^{-1}$ at a 95% confidence level. This corresponds to an enhancement factor of 1.63 compared to the integral flux published in Aharonian et al. (2006b). For the integrated flux above 5 TeV, the U.L. on the relative flux enhancement is 1.78 at a 95% confidence level.

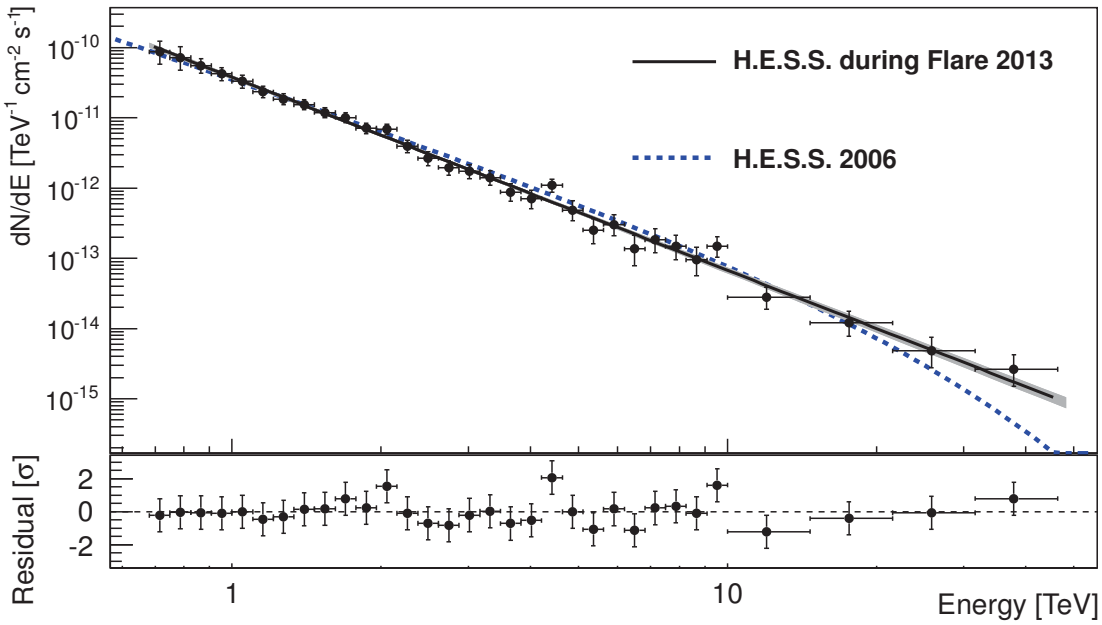

Fig. A.2.: Crab photon spectrum. Black circles indicate the H.E.S.S. Crab Nebula data taken in the nights from 2013 March 6 to March 10, fitted with a power law model. The grey shaded area is the corresponding 1σ error butterfly. The grey line corresponds to the spectrum reported in Aharonian et al. (2006b).

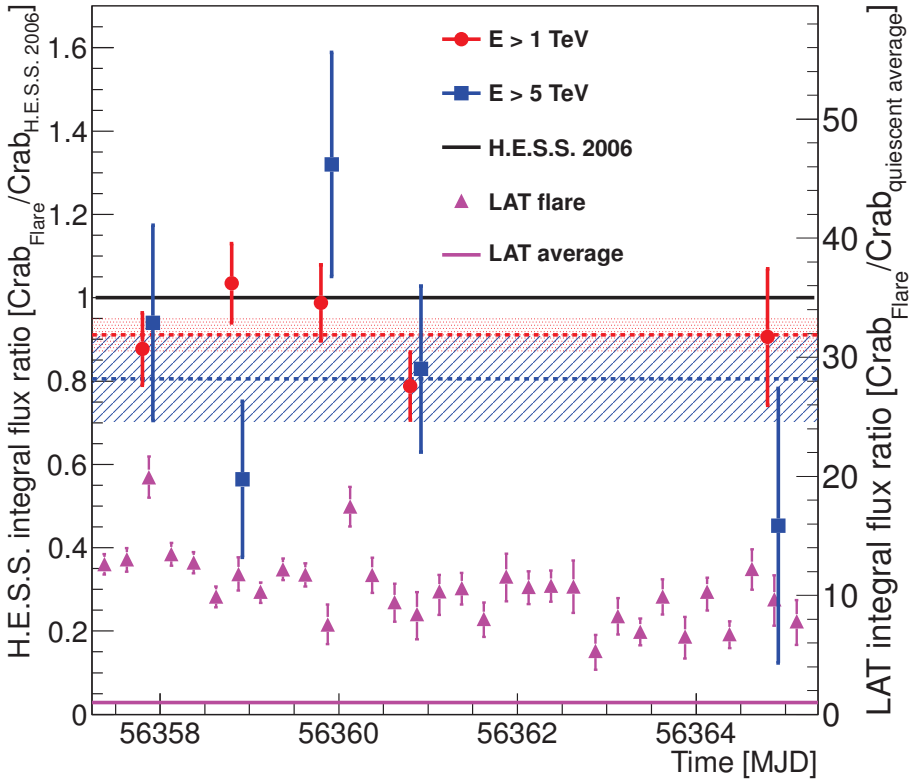

Fig. A.3.: Night-wise light curves for energy thresholds of 1 and 5 TeV. Red squares indicate integral fluxes >1 TeV relative to the integral flux above 1 TeV obtained from Aharonian et al. (2006b). Error bars depict 1σ statistical errors. The dashed red line is the fit of a constant to this light curve, the hatched red area marks the 1σ statistical error. The equivalent data for an energy threshold of 5 TeV are presented in blue.

A.4. Conclusion

No significant enhancement of the Crab flux was detected with H.E.S.S. in the (0.7−50) TeV energy band. Combining the upper limits found here with the flux enhancement measured with *Fermi*-LAT, constraints on the Doppler-factor of the emission region can be calculated. The energy spectra of the flaring component measured with *Fermi*-LAT extend to energies of a few hundred MeV, hence at least a modest Doppler boosting is favoured. However, observations of moving features in the nebula at other wavelengths do not show direct evidence for bulk flow with $v > 0.5c$. They suggest that higher Doppler factors could only be realised at the region close to the termination shock, or that the optically resolved knot, displaced from the pulsar at 0.6" ("knot 1") could be responsible for the γ-ray variability (Komissarov & Lyutikov 2011). In the latter scenario, the Doppler boost is expected to lead to an apparent enhancement of the IC component. By the results presented in H.E.S.S. Collaboration et al. (2014c), the Doppler factor is limited to $\leq 100\,(\mathrm{B}/122\,\mu\mathrm{G})$. The results at hand are consistent with the non-detection of a flaring VHE component with the VERITAS telescope in 2013 (The VERITAS Collaboration et al. 2013) and with the MAGIC telescope in 2011 (Zanin 2011). Earlier claims of a flaring VHE component (Bhat et al. 1984; Bartoli et al. 2012) are rendered unlikely.

List of Figures

List of Tables

Bibliography

Abdo, A. A., Ackermann, M., Ajello, M., et al. 2011, Science, 331, 739

Acero, F., Aharonian, F., Akhperjanian, A. G., et al. 2009, Science, 326, 1080

Acharya, B., Actis, M., Aghajani, T., et al. 2013, Astroparticle Physics, 43, 3

Ackermann, M., Ajello, M., Allafort, A., et al. 2013a, ApJ, 765, 54

Ackermann, M., Ajello, M., Allafort, A., et al. 2013b, Science, 339, 807

Aharonian, F., Akhperjanian, A., Beilicke, M., et al. 2004, ApJ, 614, 897

Aharonian, F., Akhperjanian, A., Beilicke, M., et al. 2004, ApJ, 614, 897

Aharonian, F., Akhperjanian, A. G., Aye, K.-M., et al. 2005, A&A, 442, 1

Aharonian, F., Akhperjanian, A. G., Barres de Almeida, U., et al. 2007a, A&A, 475, L9

Aharonian, F., Akhperjanian, A. G., Bazer-Bachi, A. R., et al. 2007b, ApJ, 664, L71

Aharonian, F., Akhperjanian, A. G., Bazer-Bachi, A. R., et al. 2008, A&A, 481, 401

Aharonian, F., Akhperjanian, A. G., Bazer-Bachi, A. R., et al. 2006a, A&A, 457, 899

Aharonian, F., Akhperjanian, A. G., Bazer-Bachi, A. R., et al. 2006b, A&A, 457, 899

Aharonian, F., Akhperjanian, A. G., Bazer-Bachi, A. R., et al. 2007c, A&A, 470, 475

Aharonian, F., Akhperjanian, A. G., Bazer-Bachi, A. R., et al. 2007d, A&A, 464, 235

Aharonian, F., Akhperjanian, A. G., Bazer-Bachi, A. R., et al. 2006c, A&A, 460, 365

Aharonian, F., Akhperjanian, A. G., de Almeida, U. B., et al. 2009, The Astrophysical Journal, 692, 1500

Aharonian, F., Buckley, J., Kifune, T., & Sinnis, G. 2008, Reports on Progress in Physics, 71, 096901

Aharonian, F. A., Akhperjanian, A. G., Aye, K.-M., et al. 2004, Nature, 432, 75

Aharonian, F. A., Akhperjanian, A. G., Barrio, J. A., et al. 2000, A&A, 361, 1073

Aharonian, F. A., Akhperjanian, A. G., Barrio, J. A., et al. 2001, A&A, 366, 746

Aharonian, F. A., Coppi, P. S., & Voelk, H. J. 1994, APJ Letters, 423, L5

Aielli, G., Camarri, P., Iuppa, R., et al. 2010, The Astronomer's Telegram, 2921, 1

Albert, J., Aliu, E., Anderhub, H., et al. 2008, ApJ, 674, 1037

Aleksić, J., Antonelli, L. A., Antoranz, P., et al. 2010, A&A, 524, A77+

Ando, S. & Kusenko, A. 2010, ApJ, 722, L39

Arons, J. & Scharlemann, E. T. 1979, ApJ, 231, 854

Atoyan, A. M. & Aharonian, F. A. 1996, MNRAS, 278, 525

Balzer, A. 2010, Diploma thesis, Friedrich-Alexander-Universität Erlangen-Nürnberg

Balzer, A., Füßling, M., Gajdus, M., et al. 2014, Astroparticle Physics, 54, 67

Bartoli, B., Bernardini, P., Bi, X. J., et al. 2012, The Astronomer's Telegram, 4258, 1

Battistelli, E. S., De Petris, M., Lamagna, L., et al. 2002, ApJ, 580, L101

Bednarek, W. & Idec, W. 2011, MNRAS, 414, 2229

Bednarek, W. & Protheroe, R. J. 1997, Physical Review Letters, 79, 2616

Berge, D. 2014, presentation at the H.E.S.S. collaboration meeting

Berge, D., Funk, S., & Hinton, J. 2007, A&A, 466, 1219

Bhat, P. N., Gupta, S. K., Ramana Murthy, P. V., et al. 1984, Advances in Space Research, 3, 135

Blumenthal, G. R. & Gould, R. J. 1970, Reviews of Modern Physics, 42, 237

Braun, I. 2007, Dissertation

Broderick, A. E., Chang, P., & Pfrommer, C. 2012, ApJ, 752, 22

Brucker, J. 2013, Dissertation, Friedrich-Alexander Universität Erlangen-Nürnberg

Buehler, R., D'Ammando, F., & Hays, E. 2010, The Astronomer's Telegram, 2861, 1

Buehler, R., Scargle, J. D., Blandford, R. D., et al. 2012, ApJ, 749, 26

Bühler, R. & Blandford, R. 2014, Reports on Progress in Physics, 77, 066901

Chalmé-Calvet, R., de Naurois, M., Tavernet, J.-P., & for the H.E.S.S. Collaboration. 2014, ArXiv e-prints

Chandrasekhar, S. 1931, ApJ, 74, 81

Charnes, A., Frome, E., & Yu, P. 1976, The Equivalence of Generalized Least Squares and Maximum Likelihood Estimates in the Exponential Family (Lancaster Press)

Chen, W., Buckley, J. H., & Ferrer, F. 2014, ArXiv e-prints

Cheng, A., Ruderman, M., & Sutherland, P. 1976, ApJ, 203, 209

Clark, D. & Stephenson, R. 1977, The Historical Supernovae

Cocke, W. J., Disney, M. J., & Taylor, D. J. 1969, Nature, 221, 525

Commichau, S. C., Biland, A., Contreras, J. L., et al. 2008, Nuclear Instruments and Methods in Physics Research A, 595, 572

D. Berge. 2006, Dissertation, Ruperto-Carola University of Heidelberg

Davies, J. M. & Cotton, E. S. 1957, Solar Energy, 1, 16

de Jager, O. C. & Djannati-Ataï, A. 2009, in Astrophysics and Space Science Library, Vol. 357, 451

de Jager, O. C. & Harding, A. K. 1992, ApJ, 396, 161

de Naurois, M. 2000, Ph.D. thesis, Université Pierre et Marie Curie - Paris VI

de Naurois, M. 2012, Habilitation

de Naurois, M. & Rolland, L. 2009, Astroparticle Physics, 32, 231

Doering, M., Bernloehr, K., Hermann, G., Hofmann, W., & Lampeitl, H. 2001, ArXiv e-prints

Dolag, K., Kachelriess, M., Ostapchenko, S., & Tomàs, R. 2011, ApJ, 727, L4+

Durrer, R. & Neronov, A. 2013, ArXiv e-prints

Eungwanichayapant, A. & Aharonian, F. 2009, International Journal of Modern Physics D, 18, 911

Feldman, G. J. & Cousins, R. D. 1998, Phys. Rev. D, 57, 3873

Fermi, E. 1949, Physical Review, 75, 1169

Fixsen, D. J. 2009, ApJ, 707, 916

Franceschini, A., Rodighiero, G., & Vaccari, M. 2008, A&A, 487, 837

Funk, S. & Hinton, J. 2013, Astroparticle Physics, 43, 348

Gaensler, B. M. & Slane, P. O. 2006, ARA&A, 44, 17

Gast, H. 2012, H.E.S.S internal note

Gillessen, S. 2004, Dissertation

Gilmore, R. C., Somerville, R. S., Primack, J. R., & Domínguez, A. 2012, MNRAS, 422, 3189

Gould, R. J. 1965, Phys. Rev. Lett., 15, 577

Grasso, D. & Rubinstein, H. R. 2001, Phys. Rep., 348, 163

Guy, J. & de Naurois, M. 2014, SMASH - Simulations with SASH, H.E.S.S. internal manual

H.E.S.S. Collaboration, :, Abramowski, A., et al. 2014a, ArXiv e-prints

H.E.S.S. Collaboration, Abramowski, A., Acero, F., et al. 2013, A&A, 550, A4

H.E.S.S. Collaboration, Abramowski, A., Acero, F., et al. 2011, A&A, 531, L18

H.E.S.S. Collaboration, Abramowski, A., Acero, F., et al. 2012, A&A, 541, A5

H.E.S.S. Collaboration, Abramowski, A., Aharonian, F., et al. 2014b, A&A, 562, A145

H.E.S.S. Collaboration, Abramowski, A., Aharonian, F., et al. 2014c, A&A, 562, L4

H.E.S.S. Collaboration, Abramowski, A., Aharonian, F., et al. 2014d, ArXiv e-prints

H.E.S.S. Collaboration, Abramowski, A., Aharonian, F., et al. 2015, in prep.

Hester, J. J. 2008, ARA&A, 46, 127

Hester, J. J., Stone, J. M., Scowen, P. A., et al. 1996, ApJ, 456, 225

Hillas, A. M. 1985, International Cosmic Ray Conference, 3, 445

Hillas, A. M., Akerlof, C. W., Biller, S. D., et al. 1998, ApJ, 503, 744

Hinton, J. A. & Hofmann, W. 2009, ARA&A, 47, 523

Hofmann, W. 2006, ArXiv e-prints

Jung, I. 2003, Ph.D. thesis, Ruprecht-Karls-Universität Heidelberg

Kennel, C. F. & Coroniti, F. V. 1984, ApJ, 283, 710

Kertzman, M. & Sembroski, G. 1989, KASKADE

Kohri, K., Ohira, Y., & Ioka, K. 2012, MNRAS, 424, 2249

Komatsu, E., Dunkley, J., Nolta, M. R., et al. 2009, ApJS, 180, 330

Komissarov, S. S. & Lyutikov, M. 2011, MNRAS, 414, 2017

Kronberg, P. P. 1994, Reports on Progress in Physics, 57, 325

Levenberg, K. 1944, Quart. Appl. Math, 2(2), 164

Li, J., Spitkovsky, A., & Tchekhovskoy, A. 2012, ApJ, 746, 60

Li, T. & Ma, Y. 1983, ApJ, 272, 317

Lobanov, A. P., Horns, D., & Muxlow, T. W. B. 2011, A&A, 533, A10

Loll, A. M., Hester, J. J., Blair, W. P., & Sankrit, R. 2007, in American Astronomical Society Meeting Abstracts, Vol. 39, 100.25

Lyubarsky, Y. E. 2003, MNRAS, 345, 153

Malkan, M. A. & Stecker, F. W. 1998, ApJ, 496, 13

Mariaud, C. 2014, LS 5039 Binary system

Marquardt, D. W. 1963, SIAM J. Appl. Math., 11(2), 431

Mayer, M., Buehler, R., Hays, E., et al. 2013, ApJ, 775, L37

Mayer, M., Buehler, R., Hays, E., et al. 2013, ApJLetters, 775, L37

Meyer, M., Horns, D., & Zechlin, H.-S. 2010, A&A, 523, A2

Miniati, F. & Bell, A. 2011, Astrophys.J., 729, 73

Miniati, F. & Elyiv, A. 2013, ApJ, 770, 54

Monnier, J. D., Zhao, M., Pedretti, E., et al. 2007, Science, 317, 342

Neronov, A., Semikoz, D. V., Tinyakov, P. G., & Tkachev, I. I. 2011, A&A, 526, A90+

Neronov, A., Taylor, A. M., Tchernin, C., & Vovk, I. 2013, A&A, 554, A31

Neronov, A. & Vovk, I. 2010, Science, 328, 73

Nolan, P. L., Abdo, A. A., Ackermann, M., et al. 2012, ApJS, 199, 31

Noterdaeme, P., Petitjean, P., Srianand, R., Ledoux, C., & López, S. 2011, A&A, 526, L7

Ohm, S., van Eldik, C., & Egberts, K. 2009, Astroparticle Physics, 31, 383

Ojha, R., Hays, E., Buehler, R., & Dutka, M. 2013, The Astronomer's Telegram, 4855, 1

Pacini, F. 1967, Nature, 216, 567

Porth, O., Komissarov, S. S., & Keppens, R. 2014, MNRAS, 438, 278

Primack, J. R., Somerville, R. S., Bullock, J. S., & Devriendt, J. E. G. 2001, in American Institute of Physics Conference Series, Vol. 558, 463–478

Rees, M. J. & Gunn, J. E. 1974, MNRAS, 167, 1

Rieger, F. M. 2011, International Journal of Modern Physics D, 20, 1547

Rolke, W. A., López, A. M., & Conrad, J. 2005, Nuclear Instruments and Methods in Physics Research A, 551, 493

Schlickeiser, R., Ibscher, D., & Supsar, M. 2012, ApJ, 758, 102

Sironi, L. & Giannios, D. 2013, ArXiv e-prints

Sironi, L. & Spitkovsky, A. 2011, ApJ, 726, 75

Striani, E., Tavani, M., Verrecchia, F., et al. 2013, The Astronomer's Telegram, 4856, 1

Sturrock, P. A. 1971, ApJ, 164, 529

Stycz, K. 2010, Diploma thesis, Friedrich-Alexander-Universität Erlangen-Nürnberg

Tavani, M., Bulgarelli, A., Vittorini, V., et al. 2011, Science, 331, 736

Tavani, M., Striani, E., Bulgarelli, A., et al. 2010, The Astronomer's Telegram, 2855, 1

Tavecchio, F., Ghisellini, G., Bonnoli, G., & Foschini, L. 2011, MNRAS, 414, 3566

Taylor, A. M., Vovk, I., & Neronov, A. 2011a, A&A, 529, A144+

Taylor, A. M., Vovk, I., & Neronov, A. 2011b, A&A, 529, A144+

The MAGIC Collaboration. 2008, Science, 322, 1221

The VERITAS Collaboration, Aliu, E., Archambault, S., et al. 2013, ArXiv e-prints, Ref.-ID 1309.5949

Trimble, V. 1973, PASP, 85, 579

Verrecchia, F., Striani, E., Tavani, M., et al. 2013, The Astronomer's Telegram, 4867, 1

Volpi, D., Del Zanna, L., Amato, E., & Bucciantini, N. 2008, A&A, 485, 337

Vovk, I., Taylor, A. M., Semikoz, D., & Neronov, A. 2012, ApJ, 747, L14

Weekes, T. C., Cawley, M. F., Fegan, D. J., et al. 1989, ApJ, 342, 379

Welford, W. T. & Winston, R. 1989, High collection nonimaging optics

Zanin, R. 2011, in International Cosmic Ray Conference, Vol. 7, International Cosmic Ray Conference, 71

Danksagung

Diese Arbeit hätte ich ohne die Hilfe und Unterstützung vieler Menschen nicht fertigstellen können. Zum einen sind das diejenigen, die mir die Promotion überhaupt erst ermöglicht haben, zum anderen die, die mir das Doktorandinnen-Dasein versüßt haben.
Zunächst bedanke ich mich herzlich bei meinem Doktorvater Thomas Lohse, der bereit war mich recht spontan zu übernehmen und sich in unseren Gesprächen immer sehr viel Zeit für mich genommen hat. Seine pragmatische Herangehensweise und sein Sachverstand haben mich durch die schwierigsten Herausforderungen geleitet.
Noch mehr Zeit (und sicherlich auch Nerven) hat Stefan Klepser mir geopfert, da er jederzeit erreichbar war und mir stets mit Rat und Tat zur Seite stand. Vielen Dank für die "Sub-Group-Meetings", die persönliche Beratung und das Korrekturlesen bis zum Abschluss der Arbeit, das Finden von Log2 und die Comedy-Einlagen, die Helge Schneider so nicht hinbekommt.
Einen wesentlichen Beitrag zum Gelingen meiner Arbeit hat auch Stefan Ohm geleistet. Ich danke ihm für die gute Zusammenarbeit beim Erstellen des Pair-Halo-Papers, aber vor allem für das aufmerksame und konstruktive Lesen meiner Arbeit. Durch seine Vorschläge habe ich viel gelernt, und durch den Austausch mit ihm viel gewonnen.
Bei Christian Stegmann bedanke ich mich dafür, dass er mir die Arbeit in Zeuthen überhaupt ermöglicht hat. Die stete Unterstützung weiß ich sehr zu schätzen.
Auch bei den anderen Mitgliedern der H.E.S.S.-Gruppe möchte ich mich für die schöne und spannende gemeinsame Zeit bedanken. Zu allererst bei Anneli, die mir in allen Höhen und Tiefen der Promotionszeit mit Rat und Tat zur Seite stand. Mit ihr konnte ich offen auch die "dümmsten" physikalischen Fragestellungen besprechen und die Zusammenarbeit hat einfach sehr viel Spaß gemacht hat. Egal ob in Nürnberg oder in Namibia, auf Anneli ist immer Verlass.
Markus danke ich für die cross-checks diverser Rechnungen, motivierende gemeinsame Arbeits-Wochenenden und die Geduld als Querflötenlehrer.
Dank Arnim habe ich bei der Schicht in Namibia viel mehr gelernt als gewöhnlich. Außerdem bin ich dankbar für die gute Zusammenarbeit beim Erstellen der Publikation zum Krebsnebel-Flare, und vor allem für die Lösung aller meiner Probleme, die auch nur im Entferntesten etwas mit Software und Computern zu tun hatten.
Als mein Tischnachbar hat Michi mir in unseren Gesprächen, insbesondere zu "Pulsarwindeln", oft weitergeholfen. Die Aufrechterhaltung eines hohen Spaß-Levels selbst unter harten Bedingungen hat sich aber mindestens genauso positiv auf meine Arbeit ausgewirkt.
Matthias hat mich besonders in der End-Phase meiner Arbeit unterstützt und motiviert. Dank ihm war es sogar angenehm, die halben Winterferien im Institut zu verbringen.
Außerdem bedanke ich mich bei Gianluca, Bev, Kathrin, Valou, Clemens und Eva, mit denen sowohl Arbeits- als auch Freizeit Spaß gemacht haben.
Meinen guten alten Freundinnen und Freunden, Nina, Maria, Luzi und Jo danke ich dafür, dass sie immer für mich da sind, auch wenn sie sich gerade am anderen Ende der Welt befinden.
Besonders dankbar bin ich meiner Familie, die mir in schwierigen Phasen Mut gemacht hat und sich mit mir über Erfolge gefreut hat.

Publikationsliste

Nur Veröffentlichungen die mit erheblicher Eigenbeteiligung entstanden sind werden aufgeführt. Sie wurden dem "peer-review"-Prozess unterzogen und in einem Fachjournal veröffentlicht.

[1] H.E.S.S. Collaboration, Abramowski, A., Aharonian, F., et al. 2014, "Search for Extended Gamma-Ray Emission around AGN with H.E.S.S. and Fermi-LAT", Astronomy and Astrophysics 562, A145

[2] H.E.S.S. Collaboration, Abramowski, A., Aharonian, F., et al. 2014, "H.E.S.S. Observations of the Crab during its March 2013 GeV Gamma-Ray Flare", Astronomy and Astrophysics 562, L4

Selbständigkeitserklärung

Hiermit erkläre ich, dass ich die vorliegende Arbeit selbständig verfasst habe. Jegliche Hilfsmittel sind angegeben und der Gebrauch fremder Quellen wurde im Text kenntlich gemacht.

Die vorliegende Arbeit wurde bisher keiner Prüfungsbehörde vorgelegt und ist nicht veröffentlicht.

Berlin, 13.01.2015